Dissertation

Submitted to the

Combined Faculties for the Natural Sciences and for Mathematics

of the Ruperto-Carola University of Heidelberg, Germany

for the degree of

Doctor of Natural Sciences

Presented by
M.Sc.: Sima Qamhiyeh
Born in: Nablus, Palestine

Heidelberg, May 16th 2007

A Monte Carlo study of the accuracy of CT-numbers for range calculations in Carbon ion therapy

Referees: Prof. Dr. Oliver Jäkel
Prof. Dr. Joseph Bille

To Baba & Mama
Without you, I wouldn't have made it!

The important thing in science is not so much to obtain new facts as to discover new ways of thinking about them. ~ William Lawrence Bragg

Zusammenfassung

Kohlenstoffionen deponieren den größten Teil ihrer Energie in einer schmalen Region nahe der maximalen Reichweite (Bragg Peak). Die Reichweite der Ionen in Gewebe ist abhängig von der Elektronendichte des Gewebes. Diese Elektronendichte kann gegenwärtig nur mit Hilfe eines Röntgen-Computertomographen (CT) mit ausreichend räumlicher Auflösung gemessen werden. Daher ist es notwendig, möglichst exakte CT-Daten zu erhalten.
Diese CT-Daten sind allerdings abhängig von den Parametern die während der Datenerfassung verwendet werden. In dieser Arbeit wird der Einfluss dieser Messparameter auf die CT-Daten mit Hilfe von Monte-Carlo Simulationen einzelner CT-Projektionen und der Rekonstruktion dieser Projektionen systematisch studiert. Abweichungen der CT-Daten aufgrund des Phantomdurchmessers sowie der Zusammensetzung des Substitutmaterials, dem verwendeten Phantommaterial und der gewählten Spannung der CT-Röntgenröhre werden untersucht. Desweiteren wird die Übertragung von Unsicherheiten in den CT-Daten in eine therapeutisch relevantere Reichweiten- und Dosisunsicherheit bei der Anwendung von Kohlenstoffstrahlen diskutiert.

Abstract

Carbon ions deposit most of their energy in a narrow region near the end of their range (Bragg peak). The range of ions in tissue depends on the electron density of the tissue, which can only be measured with reasonable spatial resolution using X-ray computed tomography (CT).Therefore, it is important to have accurate CT-data. However, the value of CT-numbers depends on the parameters used during the acquisition of CT-numbers. In this work, the effect of measuring conditions on CT-numbers is systematically studied by performing Monte Carlo simulations of a CT scanner and reconstructing the simulated projections. Deviations of CT-numbers due to the material of the substitutes, the material of the phantom which is used for CT measurements, the diameter of the phantom and the voltage settings of the X-ray tube are investigated. The translation of the deviations in CT-numbers into range and dose uncertainties of Carbon ions is also discussed.

TABLE OF CONTENTS

1. INTRODUCTION

Carbon ions deposit most of their energy in a sharp peak close to the end of their range. This peak in the depth dose distribution is called the Bragg peak. By comparison, the dose deposition of photons is highest in the entrance channel and decreases exponentially with depth. As a result, Carbon ion therapy spares normal tissues better than conventional radiotherapy with photons, especially in the case of deep seated tumours [1]. The depth dose profile of Carbon ions (compared with that of photons) is shown in Figure 1.

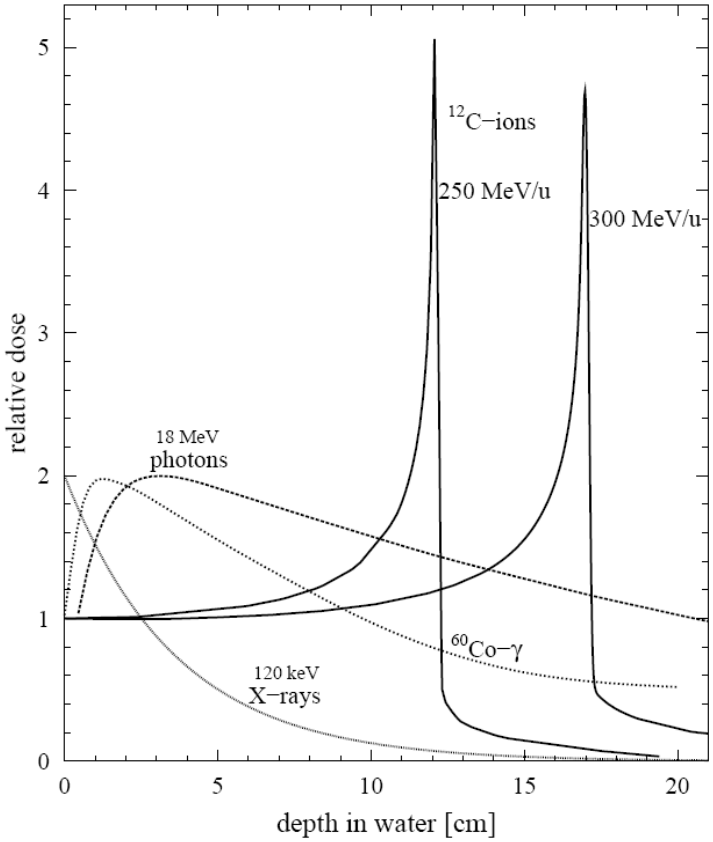

Figure 1. Depth dose profile of photons (X-rays, Cobalt-60 gamma rays, Bremsstrahlung) and Carbon ions for different energies. While photons deliver most of their dose close to the surface of the target, Carbon ions deposit most of their energy in the peak region (Bragg peak) [1].

In Carbon ion therapy, the Bragg peak is usually positioned in the tumour where the highest dose is needed. However, the position of the Bragg peak (range of ions) must be calculated with high accuracy to achieve maximum benefits of Carbon ion therapy. The correct calculation of particle range requires knowledge of the electron density or composition of the tissue.

Currently, the electron density can be obtained only from X-ray computed tomography (CT) images. The grey values of the image are CT-numbers, also referred to as Hounsfield Units (HU) in honour of Lord Hounsfield who invented the first clinical CT scanner in 1967[2]. CT-numbers have been used to distinguish the different media quantitatively. For example, the CT-number is -1000 HU for air and 0 HU for water.

Mustafa and Jackson indicated that a calibration relationship can be used to calculate the position of the Bragg peak directly from CT-data [3]. Measurements of CT-numbers and ion range in known substitutes have been used to calculate the calibration relations (see [4], [5], [6], [7] and [8]). However, the resulting calibration relations are sensitive to the material of the substitutes and the measuring conditions at the CT scanner. They are only valid for the specific scanner and specific imaging protocol.

CT data has been also used for dose calculation in conventional radiotherapy with MV photons. However, requirements for the accuracy of CT data are modest when it is used for conventional therapy. Deviations in CT-numbers cause a shift in depth dose distribution which changes slowly in the case of photons. The studies by Cozzi et al. [9], Kilby et al. [10], Thomas [11] and finally Ramm [12] suggest that the permissible uncertainty in CT-numbers increases as the energy of the MV photons increases. Thomas estimated that ±8% uncertainty in electron density can lead to dose uncertainties of only ±1% for 6MV photon beam [11]. This is equivalent to an uncertainty of CT-numbers of about ±20 HU for lung tissue (-740 HU) and about ±210 HU for cranial bone (+700 HU), assuming that the electron density relative to water (ρ_e) is calculated by Thomas as

$$\rho_e = \begin{cases} 1 + HU/1000 & HU < 100 \\ 1 + HU/1950 & HU > 100 \end{cases}.$$

On the other hand, in Carbon ion therapy, a similar uncertainty in the electron density will cause a shift in the position of the Bragg peak, i.e. dislocation of the dose maximum. For example, the ±8% uncertainty in electron density will cause a shift of about 6% in the range of ions in cranial bone.

The value of CT-numbers is affected by measurement parameters such as the size and material of the phantom used for the CT measurements, or the kilovolt setting of the X-ray tube [3] [13] [14]. The dependency of CT-numbers on the reconstruction Field Of View (FOV) and elemental composition of the scanned media was recognized in the early work of Mustafa and Jackson [3]. The dependency of CT-numbers on temperature was investigated by Homolka et al. for various water equivalent materials [15].

In this work, the effect of measuring conditions on CT-numbers is systematically studied by performing Monte Carlo simulations of a CT scanner and reconstructing the simulated projections. Deviations in CT-numbers due to the material of the substitutes, the material of the phantom which is used for CT measurements, the diameter of the phantom and the voltage settings of the X-ray tube are investigated. The translation of the deviations in CT-numbers into range and dose uncertainties of Carbon ions is also discussed.

2. BASICS OF TREATMENT PLANNING AND CT-IMAGING

2.1. Treatment planning for Carbon ion therapy

The aim of conformal radiotherapy is to deposit high doses in the tumour region while maintaining as low dose as possible in the surrounding normal tissues. The role of treatment planning is to optimize dose delivery.

The dose at a specified voxel depends on the position of the voxel in the depth dose profile of the ion beam(see Figure 1). The dose (D) is related to the particle fluence (Φ) as:

$$D = \Phi \cdot \left(\frac{S}{\rho} \right) \tag{2.1}$$

where, (S/ρ) is the mass stopping power of the medium [16].

At the Gesellschaft für Schwerionenforschung (GSI) in Darmstadt, Germany, treatment of cancer with Carbon ions started in 1997. High purity $^{12}C^{+6}$ ions are extracted from the synchrotron accelerator in pulses. The Carbon beam can be extracted in 256 monochromatic energy levels (50 MeV/u – 500 MeV/u). Depending on the beam energy, the range of the ion beam is defined for a known target.

The energy needed to hit a slice in a defined target can be calculated from the depth of the given slice. The beam can be moved from one slice to the other by changing its energy. The monochromatic beam is steered in a single slice by means of the raster scan delivery system which is composed of two perpendicular sets of magnets (vertical and horizontal) as seen in Figure 2. The position within the chosen slice is controlled by the magnetic field strength. When a homogeneous target volume is irradiated, it can be easily dissected into slices of depth, each equivalent to a specific energy.

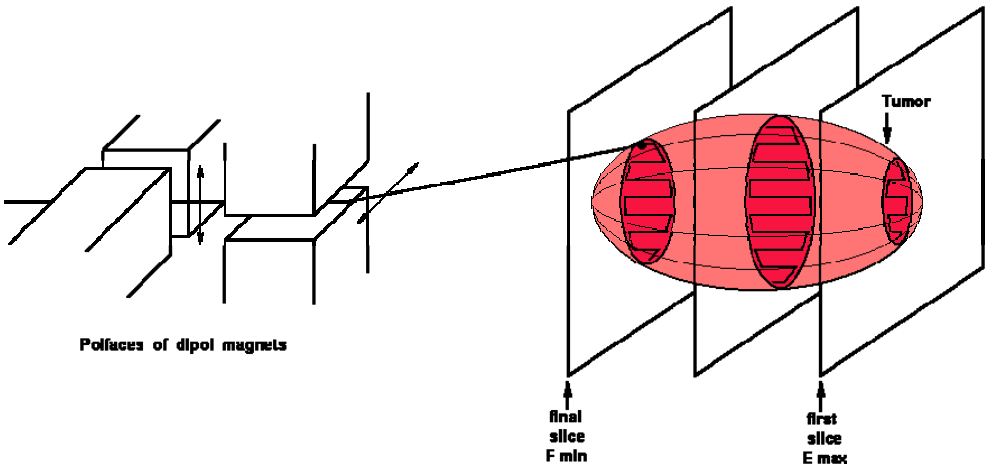

Figure 2. Raster scan delivery system for Carbon therapy at the GSI facility. An extended target is divided into slices whereby each can be covered using a specified monoenergetic beam. To over the target volume, the beam is steered within the single slice by mans of two perpendicular magnets [17].

The treatment planning code used for Carbon ion therapy in the GSI is "TRiP" [18]. To achieve a homogeneous dose distribution in the target, the intensities delivered to the shallow slices is set to lower values by means of the optimization algorithm in TRiP. The result is a Spread-Out Bragg Peak (SOBP) which is a superposition of discrete peaks of different energies and intensity as seen in Figure 3.

The treatment is usually delivered in fields. Each field is optimized to deliver a homogeneous SOBP. The dose of the SOBP is set by the clinical requirements. The modulation depth of the SOBP is planned to cover the target volume. Its distal edge (sharp dose falloff) is set at the distal end of the tumour to obtain appropriate target coverage while sparing the organs at risk. The energy of the Bragg peaks forming the SOBP are calculated from the known tumour geometry and depth. The intensity of the single peaks is optimized by the treatment planning code. For more information on "TRiP" see [18].

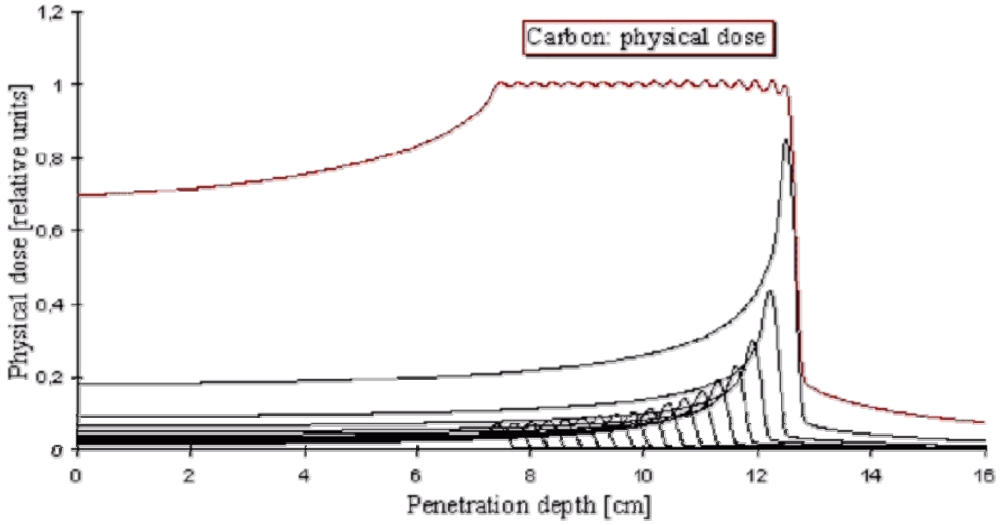

Figure 3. Spread-Out Bragg Peak (SOBP) is the super position of single Bragg peaks of different energies and intensities.

2.1.1. Ion range (stopping powers)

The range of the ions is their penetration depth in the medium. From the depth dose curve, the range is estimated as the position of the maximum of the Bragg peak. The range (R) can be calculated for ions with incident energy (E_0) as:

$$R = \int dx = \int_{E_0}^{0} (dE/dx)^{-1}\, dE = \int_{E_0}^{0} S^{-1}\, dE \qquad (2.2)$$

Where S is the stopping power of a medium and equals the rate of energy loss per path length.

$$S = -dE/dx\,. \qquad (2.3)$$

The above estimation of range is valid within the "Continuous Slowing Down Approximation" (CSDA) whereby the ions are assumed to lose their energy continuously along their path length until they are completely stopped by the medium. The CSDA can be used to calculate the range for Carbon ions because there is very little straggling in the path length of ions. In reality, the

energy loss happens via discrete interactions and the path length of the ions is slightly longer than their range[1].

The value of the stopping power varies with the energy of the incident ions. The relation between the stopping power and energy is governed by the type of interaction as seen in Figure 4. Ionization loss by collisions with electrons dominates the energy loss down to about 10 MeV/u. Below 10 MeV/u , the dominant interaction is electron capture; At very low energies, the energy loss of the ions is dominated by nuclear interactions.

Energy loss by ionization of electrons dominates the energy region of E >30 keV/u. However, the electron-stripped ions start to capture target electrons below 10 MeV. The energy loss of ions can be calculated by the Bethe-Bloch equation. The simple form of the Bethe Bloch equation (equation (2.4)) is valid for electron-stripped ions, i.e. energy higher than 10 MeV. The range of a 10 MeV/u Carbon ion is about 1 mm. Therefore, for a good approximation, the stopping power can be calculated from the Bethe-Bloch equation.

$$-\frac{dE}{dx} = 4\pi \cdot {r_e}^2 \, m_e c^2 \, N_{Av} \cdot \frac{z^2}{\beta^2} \cdot \rho \frac{Z}{A} \cdot \left[\ln\left(\frac{2 m_e c^2 \beta^2 \gamma^2}{I} \right) - \beta^2 \right]. \qquad (2.4)$$

In equation (2.4), c is the speed of light, N_A is Avogadro's constant, e is the elemental charge, m_e is the mass of the electron and r_e is the classical radius of the electron. z is the charge number of the projectile. β is the relative velocity of the projectile and $\gamma = 1/\sqrt{1-\beta^2}$. Z and A stand for the charge and atomic weight of the target atoms, ρ is the density of the target medium and $\rho Z/A$ is the electron density of the target material. Finally, I is the mean ionization potential of the target medium i.e. the mean energy needed to ionize a target atom [20]. For example, the ionization potential of water is estimated to be around 75 eV.

For precise calculation of R , electron density and mean ionization potential for each voxel should be assigned for all tissue types in the beam path. Another approach is to calculate R as a function of energy in a reference medium then use a look up table of range in material as a function of range in a reference medium. The reference medium for dosimetry is water. Data on stopping power and range of ions in water is available for all deliverable beam energies. Similar measurements in other media are generally not as accurate. Therefore CT-data are usually presented relative to water [18].

[1] The range (R) is proportional to the path length (PL) by: $R = d \times PL$ where d is the "detour factor and is almost one for Carbon ions.

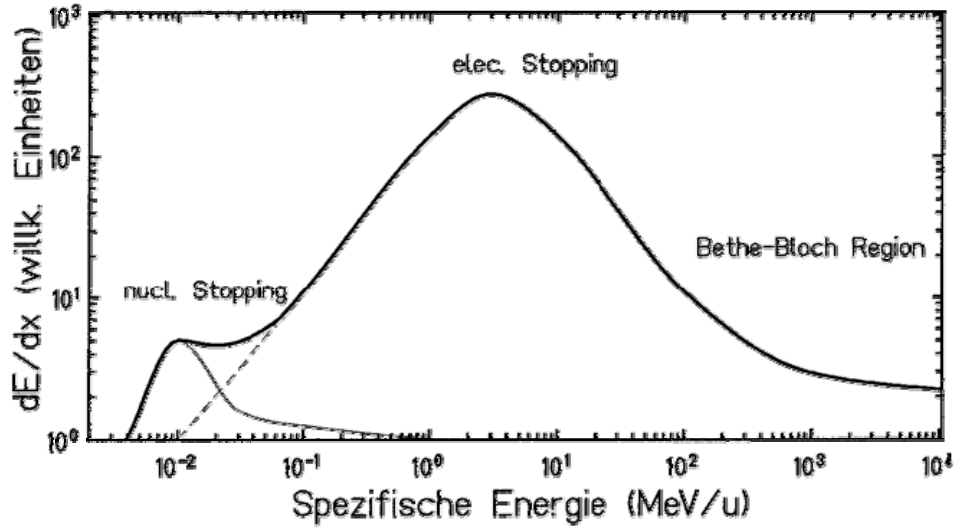

Figure 4. Stopping power (y-axis) as a function of incident energy (x-axis). Energy is written in terms of energy per nucleon (MeV/u). The energy loss is dominated by ionizing of the atoms (described by the Bethe-Bloch equation) for the range of E >10 MeV. Nuclear collisions dominate the lower energy part. In between, electron capture governs the interaction of the ions [17].

2.1.2. Range shift and Water Equivalent Path Length (WEPL)

As the stopping powers within the body change, the range changes and the position of the Bragg peak is shifted. An example for peak shifts due to inhomogeneities in the beam path is presented in Figure 5 for a 184 MeV/u Carbon beam. The range of the ions is energy dependent. In order to deliver the dose at the specified position in the presence of inhomogeneities in the beam path, the energy of the beam has to be changed while delivering a single slice.

The amount of shift in the peak position in water due to a slab of material is called the Water Equivalent Path Length (WEPL) of that slab. In other words, if a slab of medium with given thickness is replaced by extra water of thickness equal to the WEPL, the position of the shifted Bragg peak will be reproduced using the same beam energy.

Replacing inhomogeneous slabs by their equivalent water depths will preserve the information on particle range while facilitating the calculation of beam energy. Slices at a certain depth could again be delivered using a single energy as in the case of a homogeneous body. However, the geometrical definition of the target in terms of depth slices might be changed as seen schematically in Figure 6 .

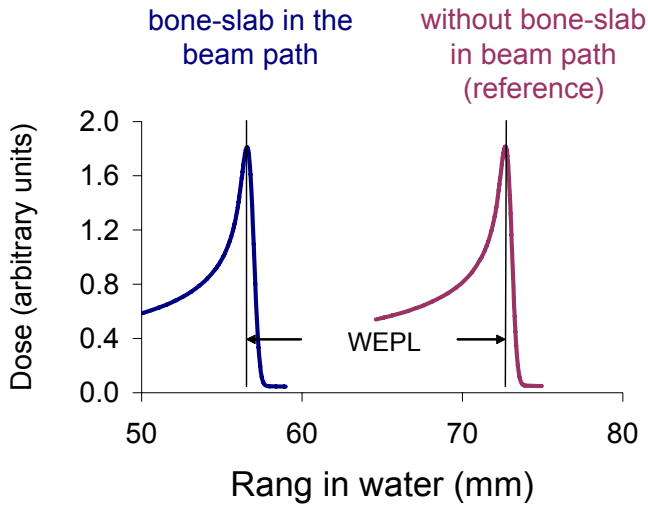

Figure 5. Water equivalent Path Length (WEPL) is the range shift of a Carbon beam in water due to a slab of material (in this case bone). The shift here is due to the presence of 1 cm slab of cortical bone substitute in the beam path.

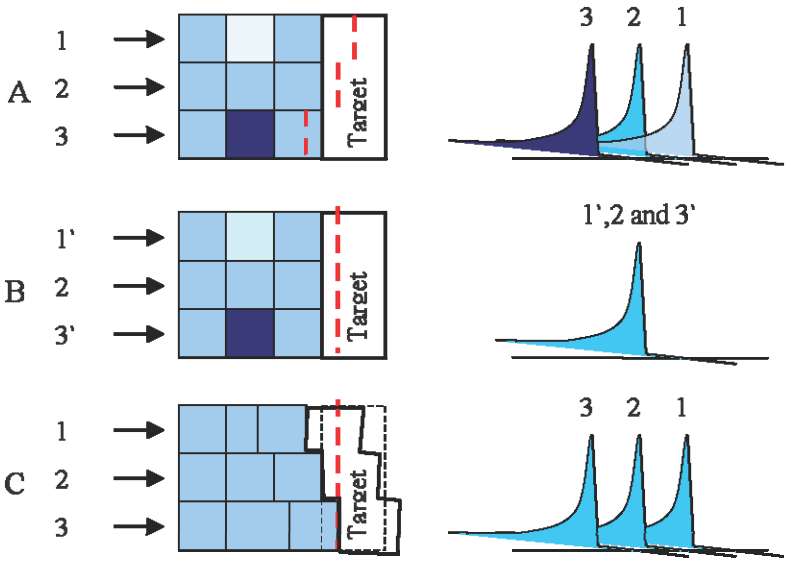

Figure 6. Schematic diagram on applying WEPL for heterogeneity corrections. A: in a heterogeneous object. Rays 1,2 and 3 have different range for the same incident energy. The range of the rays is shown as the dashed red lines. While rays 1 and 2 reach the target, 3 does not. B: rays 1,2 and 3 are delivered with different energy to have the same range and hit the target which is at the same depth for all three rays . C: heterogeneities are replaced with their equivalent depths; the beam can be delivered using a single energy for all three rays; the range distribution in A is maintained; however, the target definition in terms of depth should be modified.

The ratio of WEPL to the thickness of a slab (T) is called the relative range. In small slabs, where S is nearly constant, the relative range is proportional to the stopping power ratio of the medium relative to the stopping power of water. Hence, it is proportional to the electron density of the medium relative to the electron density of water to a first approximation as seen in equation (2.5).

$$\frac{WEPL}{T} \propto \frac{\rho_e^{medium}}{\rho_e^{water}} \cdot \frac{\left[\ln\left(2m_e c^2 \beta^2 \gamma^2 / I_{medium}\right) - \beta^2\right]}{\left[\ln\left(2m_e c^2 \beta^2 \gamma^2 / I_{water}\right) - \beta^2\right]} \tag{2.5}$$

In fact, the dependence of the relative range (equation (2.5)) on the energy of the incident particles is small for media with mean ionization energies comparable to water ($I_{medium} \approx I_{water}$). Measurement of relative range in muscle substitute has been performed by Jacob [21]. The results show that the relative range is independent of the energy of the incident Carbon ions for energies greater than 50 MeV/u.

Hence it is possible to calculate the stopping power of any medium using the relative range as:

$$S^{medium} = S^{water} \cdot \frac{WEPL}{T} \tag{2.6}$$

And the range is calculated using the CSDA by:

$$R^{medium} = \int \left(S^{medium}\right)^{-1} dE = \int \left(\frac{WEPL}{T}\right)^{-1} \cdot \left(S_i^{water}\right)^{-1} dE\,. \tag{2.7}$$

The CT-image of a heterogeneous body is dissected into volume elements (voxels). The range of ions in each voxel (R_i^m) can be calculated using:

$$R_i^m = \int_{E_{i+1}}^{E_i} \left(S_i^m\right)^{-1} dE \tag{2.8}$$

Here, E_i is the energy of the ions in the entrance channel of voxel *i.* And the total range of the beam is the sum of the range of the pixels along the beam path.

2.2. Basics of X-ray imaging

A CT image is a distribution of X-ray attenuation coefficients (relative to water) in the scanned object. The object is positioned between an X-ray source and detectors which are arranged in a ring-like gantry. Both the source and detectors are rotated around the object to record X-ray projections from different angles of view. The projections are later reconstructed into an image. This section describes X-rays production, interaction and detection in CT scanner, image reconstruction from projections and finally image representation in Hounsfield Units (HU).

Historically, CT scanners are classified in generations. The classification is based on the source and detector arrangement and their movement patterns to record the projections of the scanned object. The first generation CT scanners were designed with a pencil beam source and a single detector element, both the source an detector are scanned across the object to record parallel projections for each imaging angle. In second generation scanners, an array of detector-elements is used; the projections are of a partial fan beam. Third generation CT scanners have a single X-ray source and an arc shaped detector array. The beam from the X-ray source is fan shaped; the source-detector arrangement is rotated around the body to record the projections from different angles. Fourth Generation scanners have a single source and a complete ring of detectors; only the X-ray source is rotated to record projections from different angles. Higher generations of –scanners use more detector layers or flat panel detectors [2][22].

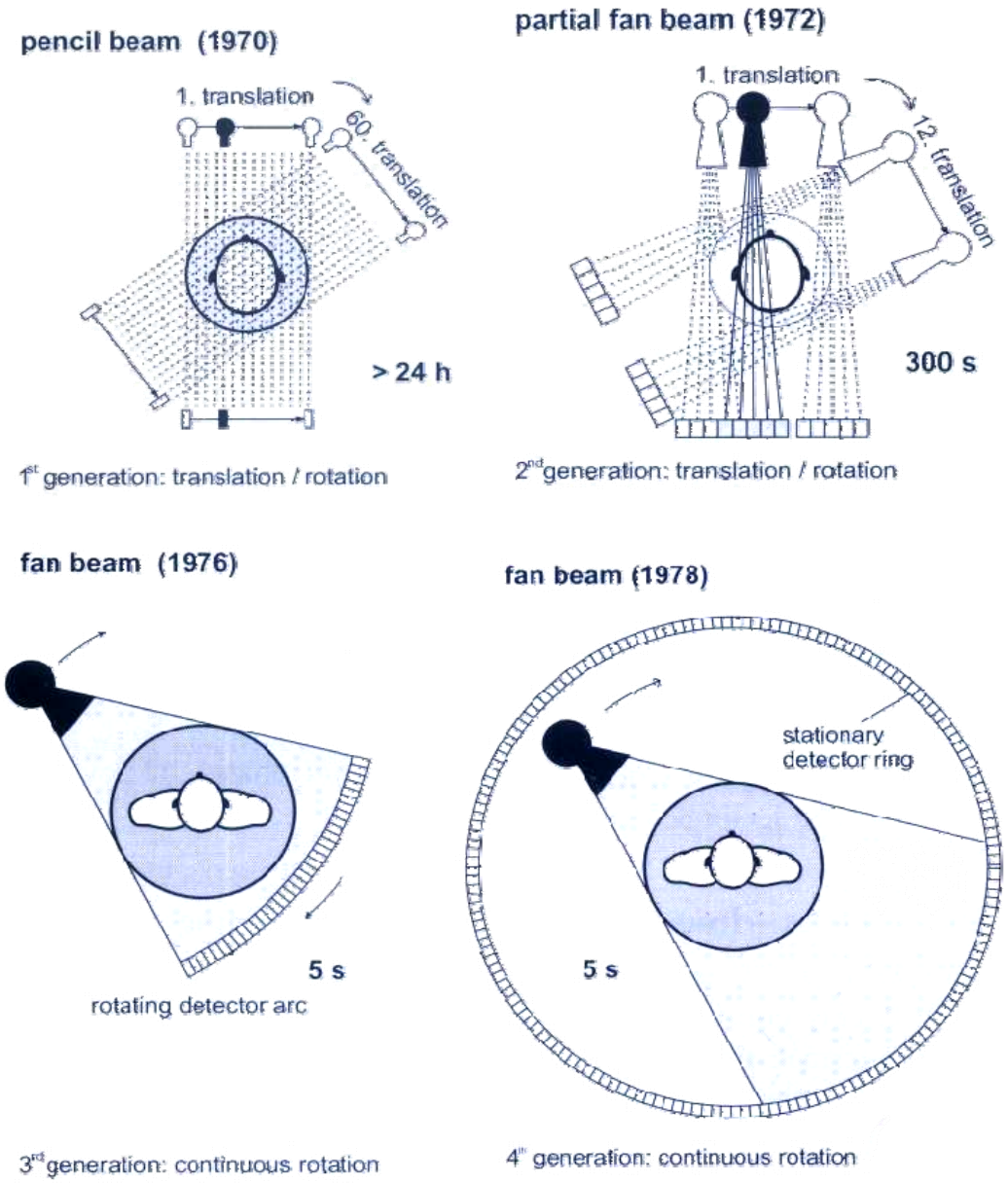

Figure 7. Generations of CT scanners. The first generation CT scanners used a point like source and a single detector element, both the source and detector are scanned across the object to record parallel projections then the source-detector arrangement was rotated to record projections for each imaging angle. Starting from the second generation (1972), an array of detector was used. The source and detectors wee still scanned across the body to record almost parallel projections. Third generation CT scanners have an arc shaped detector array that is focused to the focal spot; one needs only to rotate the source detector array to record fan-shaped projection. Fourth Generation scanners have a complete ring of detectors; only the X-ray source is rotated to record projections from different angle. The issue date of the different generations and the time needed to record a single image are also indicated [22].

2.2.1. Production of X-rays

X-rays are generated by transforming the kinetic energy of accelerated electrons into electromagnetic radiation. This can be through Bremsstrahlung or characteristic emission.

In the case of Bremsstrahlung (break radiation), the electrons are deflected by the coulomb field of the target nuclei. The accelerated electron emits electromagnetic radiation in the form of X-ray photons. The probability (σ) for a Bremsstrahlung event is low but increases with the atomic number of the target medium (Z) and the energy of the incident electrons (E).

$$\sigma \propto Z \cdot E^2 \tag{2.9}$$

The energy of the X-ray photon depends on the interaction distance. The energy spectrum of the X-ray photons covers the range between zero (no interaction) and maximum incident energy of the charged particle (electrons are stopped). The unfiltered Bremsstrahlung spectrum is inversely linear with energy up to the energy of incident charged particles.

The intensity of the Bremsstrahlung radiation (I) is proportional to the atomic number of the target material (Z).

$$I \propto Z^2 \tag{2.10}$$

The efficiency (η) of Bremsstrahlung production increases with Z and E as:

$$\eta \propto Z \cdot E \tag{2.11}$$

In the case of characteristic emission, the incident particle knocks out one of the bound electrons in the atomic shells. The newly created vacancy is filled by another electron from higher energy shells and the difference in energy is emitted as an X-ray photon. The emitted photon may either leave the atom without further interaction or can interact with one of the valence electrons which will in turn leave the atom as an Auger electron. The ratio of characteristic X-ray emission to Bremsstrahlung increases with increasing energy of the incident charge.

In general the efficiency of X-ray generation is rather poor; for example, if electrons with the kinetic energy of 100 keV are incident on Tungsten target (Z = 74), only 1% of the kinetic energy of the electrons is transferred to X-ray production while the remaining 99% is dissipated as heat. The efficiency is further decreases by filtration of photons in the target material.

2.2.2. X-ray interactions and attenuation coefficients

The attenuation of X-rays in matter is due to their interaction with atoms of the target. The interactions can be with the nucleus (as in pair production), with the electrons (as in Compton scattering) or with the atom as a unit (as in the photoelectric absorption and coherent scattering). The probability of the different interaction paths depends on the energy of the incident photons, the atomic number (Z) and the electron density (ρ_e) of the target material.

In pair production, the energy of the incident photon is transferred to the production of an electron positron pair in the vicinity of the target nucleus. Only pairs can be created since charge is conserved. The energy of the incident photon must therefore be larger than the total rest mass of the pair (1.02 MeV for the electron-positron pair). Pair production can not happen in the energy range used in CT imaging and will not be further discussed.

Compton scattering is an inelastic process in which the incoming photon scatters off a loosely bound electron and loses a part of its incidence energy (E) to the electron. The energy of the scattered photon (E') is the difference between the incident energy and the kinetic energy of

the liberated electron. Taking momentum conservation into account, the energy of the scattered electron can be calculated using equation (2.12) .

$$\frac{1}{E'} - \frac{1}{E} = \frac{1}{m_e c^2}(1 - \cos\theta) \tag{2.12}$$

where (θ) is the deflection angle of the photon.

Compton scattering dominates the interactions in the medium energy range (50 kV-10 MV). The probability increases with increasing electron density of the medium. The electron density (ρ_e) equals $\rho Z/A$ and Z/A is 0.4-0.5 for all materials except for hydrogen (Z/A=1).
In photoelectric interactions, the incident X-ray photon is totally absorbed by a bound electron in the atom. The electron is released with a kinetic energy which is the difference between the energy of the incident photon and the binding energy of the electron. The probability of photoelectric interactions is proportional to Z^3/E^3 . Therefore, the possibility of photoelectric interactions in bony tissues (containing Calcium, Z=20) is about 6 times more than in soft tissues. The effective Z of muscle is about 7.4; it is about 13.8 for bone [23]. The possibility increases when the photon energy is close to the binding energy of orbital electrons (edge absorption). The K-edge is below 1keV in biological compounds of H, C, N and O [24].

Rayleigh scattering or elastic scattering happens when the photon is absorbed and the atom is excited but not ionized. The excited atom reemits a photon with almost the same energy in a different direction. The atom recoils just enough to conserve momentum, but energy loss is minimal and almost all the energy goes to the photon. The possibility of Rayleigh interactions decreases with the energy of the incident photons.

The linear attenuation coefficient (μ) defines the fraction of photons removed from an incident beam by a thin layer of material. If a given number (N) of photons is incident on a thin layer (Δs) of material then the number of attenuated photons (ΔN) equals:

$$\Delta N = -N \cdot \mu \cdot \Delta s\,. \tag{2.13}$$

Assuming an infinitely thin layer and an initial beam intensity of I_0, the intensity after attenuation (I) could be written as:

$$I = I_0 \cdot \exp(-\mu \cdot s)\,. \tag{2.14}$$

For a single process, the linear attenuation coefficient can be calculated as the product of the interaction cross section ($\sigma(E,Z)$) with the density of interacting particles (electrons) as:

$$\mu(E,Z) = \sigma(E,Z) \cdot \rho_e\,. \tag{2.15}$$

The relation between the electron density and the attenuation coefficients is not linear since the interaction cross sections also depends on the electron density.

The total linear attenuation coefficient of photons (μ) is the sum of coefficients of the different interaction processes.

$$\mu(E,Z) = \mu_R(E,Z) + \mu_\sigma(E,Z) + \mu_\tau(E,Z)\,, \tag{2.16}$$

where μ_R, μ_σ and μ_τ are the attenuation coefficients due to Rayleigh scattering, Compton scattering and photoelectric effect respectively.

The *mixture rule* defines the attenuation coefficients for mixtures and compounds where the effect of the different elements (*i*) is assumed to be additive. The *mixture rule* is:

$$\mu/\rho = \sum_i \omega_i \cdot \mu_i/\rho_i \,, \tag{2.17}$$

where ω_i is the fraction by weight of the ith element [25] [26].

2.2.3. Detection of X-rays

Detecting X-rays is possible by tracing the effect of X-ray interactions on a detector medium. The effects vary from chemical (e.g. radiographic films) to photon remittance or luminescent (e.g. scintillation crystals like NaI and Gd_2O_2S) to ionization effects (e.g. semiconductor crystals and gas filled detectors). In CT imaging, the most commonly used types of detectors are scintillation crystals and Xenon filled gas detectors.

Several layers of detectors can be used simultaneously to shorten the exposure time of the patients by simultaneously imaging several slices. The detector array is additionally equipped with anti-scatter grids to eliminate the noise due to scatter in the patient or in the beam shapers and filters.

Gas detectors are operated as ionization detectors i.e. pressurized gas is held between two electrodes. Interaction with X-rays ionizes the gas atoms into positively charged atoms and negative electrons which are collected at the electrodes. The signal current increases with the applied voltage, except in the IC-plateau where changes in the applied ionization voltage can only cause small changes in the signal. Gas filled detectors are operated in the IC-plateau.

The detector arc is designed as a single block. Its volume is divided into many chambers (up to 1000) by means of the electrodes which are also used to collect the signal from the chambers (see Figure 9). There is no variation between the different chambers concerning gas properties. Therefore, multi-detector inhomogeneity is not an issue. However, the quantum efficiency of Xenon filled detectors is low (50-70%) compared to scintillation crystals even if the gas is kept at high pressures reaching 20-25 atmospheres.

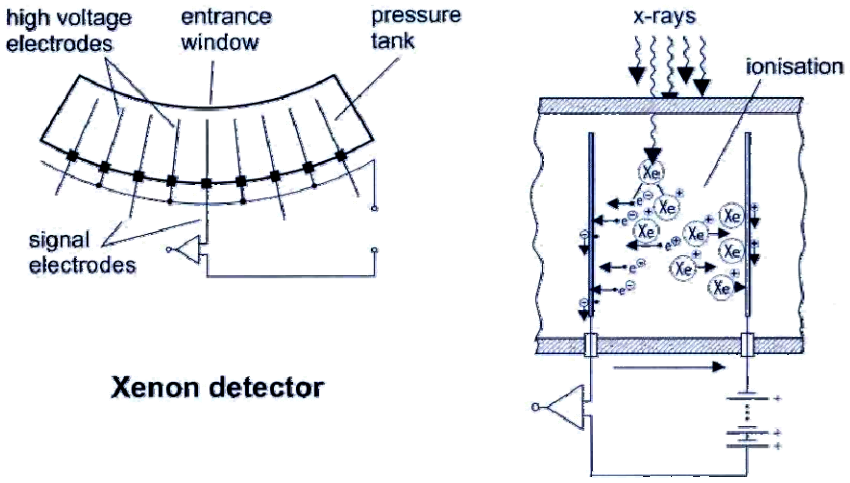

Figure 8. Xenon gas detector systems in the CT-scanner [22].

Scintillation crystals emit visible or UV light, when irradiated with X-rays photons. The photons excite electrons from the valence band (VB) to the conduction band (CB). The excited electrons fall back to the VB emitting photons with energy equal to the difference between the two bands. The emitted photons (light) can be collected and their intensity is translated into an electronic signal by either photodiodes or Photo Multiplier tubes (PMT). Most detector arrays are equipped with photodiodes. PMT are larger than photodiodes; this is a disadvantage when detector elements are packed in an arc-like geometry, as spatial resolution is lost.

Single detector elements are designed as a separate unit to avoid cross talk when centilation crystals are used as CT-detectors. Therefore it is important to have homogeneous signal from the different detector elements to avoid ring artefacts in the image. The need for a gap between active detection areas limits the packing density of the detectors. Scintillation crystals also need a very stable voltage supply for stable signal read-out since the separation of the energy bands depends on the applied voltage. CT vendors use crystals with very high detector quantum efficiency (98-99.5%). Typically used crystals are $CdWO_4$ and Ultra Fast Ceramic crystals (UFC) such as Gd_2O_2S. Unfortunately, the performance of the crystals can be affected by radiation damage. This can be limited by doping the crystal with rare earth elements and frequent calibrations.

Gas filled detectors are cheaper and easier to handle than ceramic detectors. However, the trend to use multi-detector arrays limits their usability compared to crystal detectors.

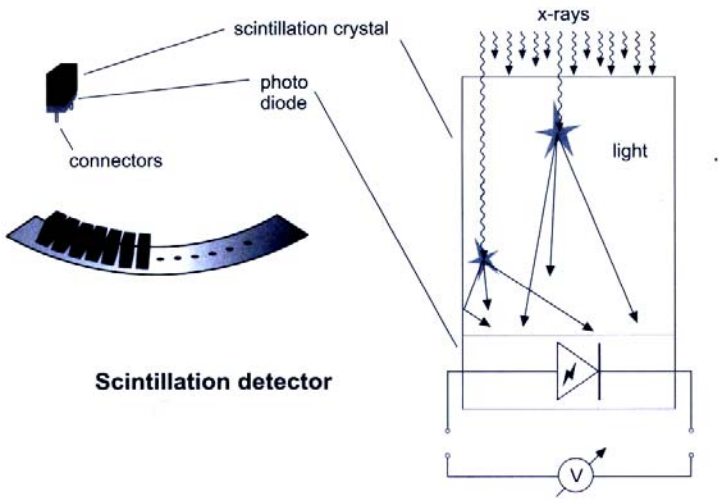

Figure 9. Scintillation detector systems in the CT-scanner [22].

2.2.4. Sampling of projections (sinogram)

Objects can be regarded as a stack of N small volumes (Voxels) where each voxel (i) has a unique value of the linear attenuation coefficient ($\mu_i(E,Z)$). Assuming the incident X-ray photons are monochromatic with an intensity (I_0), the attenuation at the end of the X-ray path (s) through N individual elements is :

$$I = I_0 \cdot \prod_i^N \exp(-\mu_i \cdot s_i) = I_0 \cdot \exp \sum_i^N (-\mu_i \cdot s_i) \qquad (2.18)$$

As N approaches infinity ($N \to \infty$), $I \to I_0 \cdot \exp\left(-\int \mu \cdot ds\right)$.

However, the incident X-ray is usually polychromatic with a defined spectrum ($\Omega(E)$) which depends on the X-ray tube design and energy of the incident electrons. The response signal of the detector-system (D) is also energy dependent. As a result, the intensity of the detected photons is a function of energy.

Assuming that the volume between source and detectors is filled with vacuum, the initial intensity of the X-ray photons becomes:

$$I_0 = \int \Omega(E) \cdot D(E)\, dE \,. \tag{2.19}$$

If an object is placed between the source and the detectors, the measured intensity at the detectors becomes:

$$I = \int \Omega(E) \cdot D(E) \cdot e^{-\int \mu(E,Z)ds}\, dE \,. \tag{2.20}$$

In X-ray imaging, the measured projection value (p) is defined as the line integral of the attenuation coefficients along the line of view:

$$\mathrm{p} = -\ln(I/I_0) = \int \mu\, ds \,. \tag{2.21}$$

As a result, p is a function of the energy and position.

The complete set of projections (μ) can is also be described by the two dimensional matrix (μ_{ij}). Assuming well known projection geometry -e.g. parallel projections as in Figure 10- and a detector array of L cells, the projection of μ can then be calculated as $\hat{P}_L\ \mu$, where

$$\hat{P} = \int_{-\infty}^{\infty} ds. \tag{2.22}$$

When the source-detector arrangement is rotated around the object to record the projections from M different angles (θ), the projections are subjected to the rotation operator $\hat{\Theta}_M$. The projection (p) can be written as an MxL matrix (p_{lk}) as:

$$p_{lk} = \hat{\Theta}_M\ \hat{P}\ \mu_{ij} \,. \tag{2.23}$$

The system operators ($\hat{\Theta}_M$ and $\hat{P}$) can also be described by the matrix (A) which is based on the scanner geometry and X-ray energy.

$$A = \hat{\Theta}_M\ \hat{P} \text{ and} \tag{2.24}$$

$$A \cdot \mu_{ij} = p_{kl} \,. \tag{2.25}$$

If the set of independent projections is large enough, it is possible to calculate μ_{ij} for each volume element i.e. to reconstruct the image.

The complete data set of projections can be presented as a sinogram which gives the signal of detector elements as a function of the rotation angle (θ). The horizontal lines in the sinogram represent the projections from a single angle of view by the different L channels. The naming

"sinogram" initiated from the sinusoidal function representing the image when a point like object is scanned as shown in Figure 9.

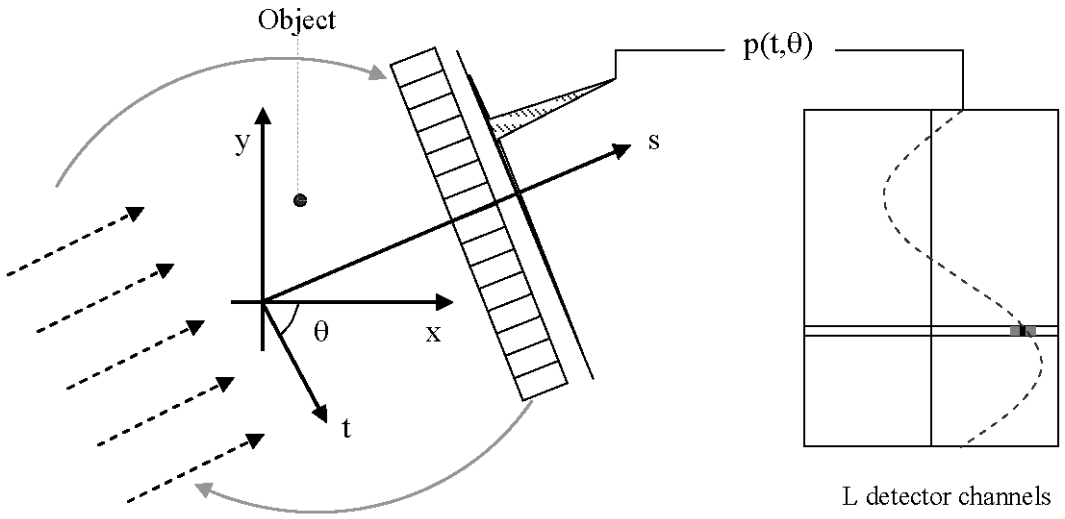

Figure 10. Measurement of projections by a parallel beam and a linear array of detector elements. The resulting projections are represented as a sinogram (right).

2.2.5. Image reconstruction from projections

The principle of calculating an object from an infinite set of projections was first developed by Radon in 1917. However, it was Cormak in 1956 who developed the mathematical theory of image reconstruction in radiology (Hsieh [2]).

There are several approaches for image reconstruction:

- Direct mathematical methods,
- Iterative reconstruction and
- Back projection.

The concept of image reconstruction can be easily explained for two dimensions.

Direct mathematical methods

Assume that the object is dissected into an NxN matrix (μ), one needs at least N^2 independent equations which have to be solved simultaneously for μ. The limiting factor for attempting to use this method in clinical applications is the high use of computing power. Matrix inversion can be applied if the matrix A is known. However, determining the matrix (A) is not as simple as it sounds because of additional noise and incomplete description of energy dependencies. The source of noise can be scattering or detector electronics.

Iterative reconstruction

Iterative reconstruction approaches are based on assuming a primary simple solution of the image. The measurements are then used to correct the simple solution and bring it closer to the measured object. The process can be repeated till the difference between image and

measurements is sufficiently small. One method is the Algebraic Reconstruction Technique (ART). Here, projections of the simple solution (similar to the measurement arrangement) are calculated and compared to the measured projections. The difference between measured and calculated projections is used to correct the simple solution by adding the difference to voxels along the line of view.

An example of an object which has a high density core (grey) and low density surroundings (white) is shown in Figure 11. Figure 12 shows the steps of iterative reconstruction by means of ART for the above example. The measured projections are also schematically shown in Figure 11.

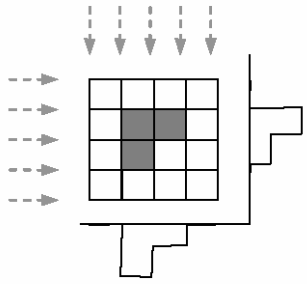

Figure 11. Schematic representation of an object which is scanned with a parallel beam. The projections of the object which has a high density core (grey) and low density surroundings (white) are also shown.

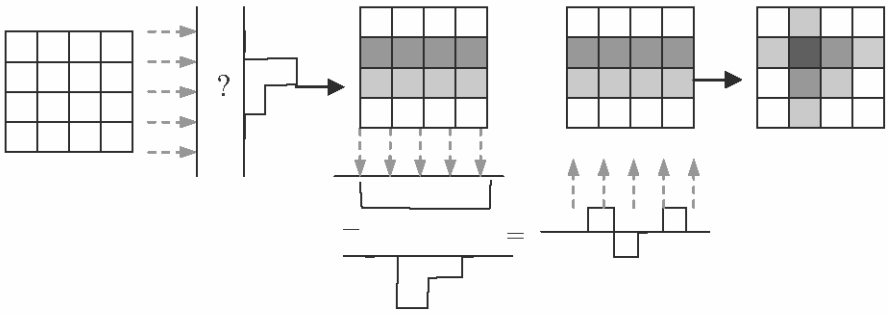

Figure 12. Schematic representation of iterative reconstruction using the ART method. A primary simple solution is set. Projections from the simple solution are collected and compared to the respective measured projections. Difference is added to correct the simple solution. The comparison and correction of projections can be performed several times until the results are satisfactory.

In general, iterative reconstruction techniques are time consuming and demand a lot of computer time. They also need large computer memory since the result of the last iteration is needed to calculate the next. The complete set of measured projections should be available to start the reconstruction. Iterative reconstruction methods are extensively used in Emission Tomography (PET, SPECT) where the projection signals are poor and carry a lot of noise. Elegant iterative reconstruction methods such as the Maximum a Posteriori approach (MAP) and Expectation Maximization methods such as OSEM are finding new applications in clinical CT imaging. The trend to use iterative reconstruction methods in CT is increasing with improved computer hardware and improved algorithm efficiency. It is driven by the successful handling of metal artefacts and truncated projections by the algorithm.

Reconstruction by back projection

Back projection is the redistribution of data from the measured projections along the image matrix. The image matrix is first set to zero in all image pixels and the contributions from the different projections are added up for each angle as seen in Figure 13 for the same example as above.

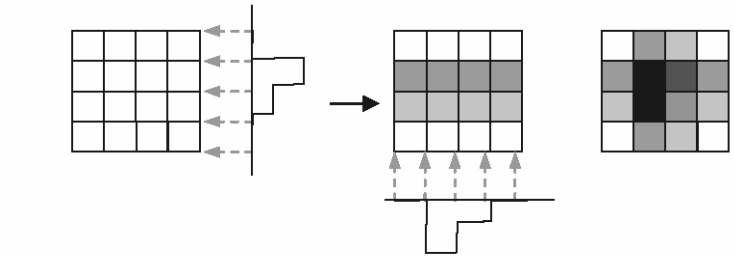

Figure 13. Schematic representation of back projection reconstruction. A primary matrix is set to zero. Projections are added up one after the other. Once all projections are added up the reconstruction process finishes.

The reconstructed images have an obvious blurring of the object due to smearing projection data across the image. This can be explained by means of the Central Slice Theorem (also known as Fourier Slice Theorem). The theory states that the Fourier transformation of a parallel projection is equivalent to a single line through the center in the map representing a 2D Fourier transform of the object.

The consequences of the Central Slice theorem is that it is possible to calculate the object function $\mu(x,y)$ by a 2D inverse Fourier transform of the 1D Fourier transform of the projections.

Let $\mu(x,y)$ be the distribution of attenuation coefficients of the object in Figure 14. Let the 2D Fourier Transform (FT_2) of $\mu(x,y)$ describe the object in Figure 14 as:

$$FT_2\left[\mu(x,y)\right] = F(u,v) = \int_{-\infty}^{\infty}\int_{-\infty}^{\infty} \mu(x,y)\, e^{-2i\pi(ux+vy)}\, dx\, dy \,. \tag{2.26}$$

Hence,

$$\mu(x,y) = FT_2^{-1}\left[F(u,v)\right] \tag{2.27}$$

Let t and s be the rotated reference frames with an angle of θ . Then:

$$\begin{aligned} t(x,y) &= x\cos\theta + y\sin\theta \,, \\ s(x,y) &= -x\sin\theta + ycon\theta \,, \end{aligned} \tag{2.28}$$

The projection data can be written in terms of equation (2.21) and (t, s) coordinates as

$$p(t,\theta) = \int_{-\infty}^{\infty} \mu'(t,s)\, ds \,. \tag{2.29}$$

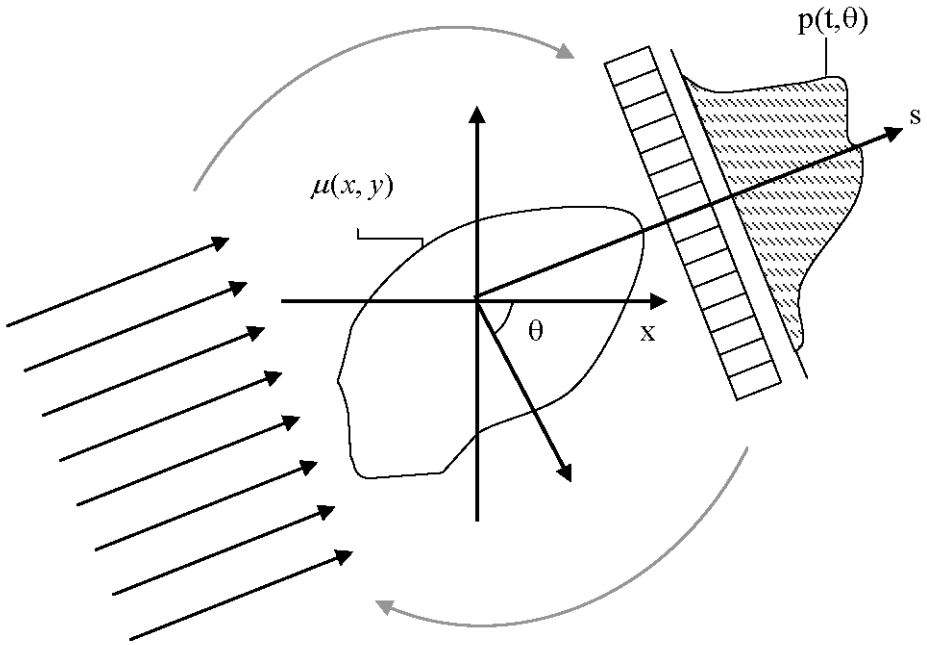

Figure 14. Schematic diagram describes measurement of projections of parallel beam by a linear array of detector elements [2].

For simplicity, assume $\theta = 0^0$. Then

$$p(t,0) = \int_{-\infty}^{\infty} \mu(x,y)\, dy\,. \tag{2.30}$$

The 1D Fourier transform of $p(t,0)$ is

$$FT_1[p(t,0)] = \int_{-\infty}^{\infty}\int_{-\infty}^{\infty} \mu(x,y)\, e^{-2i\pi(ux)} dy dx\,. \tag{2.31}$$

Thus it is clear that

$$FT_1[p(t,0)] = FT_1[p(t,\theta)]_{\theta=0} = FT_2[\mu(x,y)]_{y=0} \tag{2.32}$$

The consequences of the Central Slice Theorem is that: it is possible to calculate the object function $\mu(x,y)$ by a 2D inverse Fourier transform of the 1D Fourier transform of the projections.

$$\mu(x,y) = FT_2^{-1}[F(u,v)] = FT_2^{-1}[FT[p(x,y)]]\,. \tag{2.33}$$

However, the Central Slice Theorem is only valid for parallel projections because the main assumption is that the projections represent a single line through the center of the 2D FT of the object. In the case of fan projections, the Fourier transform of projections is still a line in the 2D Fourier transform of the object, but it no longer passes through the center. See Figure 15 for illustration.

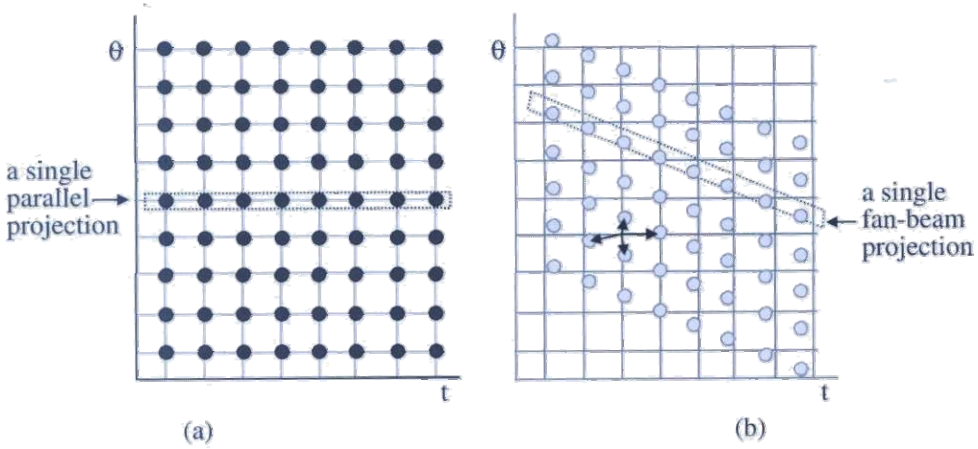

Figure 15. The sampling pattern in sinogram space for a parallel beam projection (a) and for a fan beam projection (b). Note that the sampling pattern can be rebinned to the parallel beam grid by calculating the interpolation from nearest neighbours [2].

The result is that the image can not be calculated by simply calculating the inverse Fourier transforms of the measured projections because the projections will no longer be allocated to the right image pixels.

This can be rectified by reorganizing the sinogram data set such that it is equivalent to parallel beam. The process is called "rebining the projection data". Once the rearranged sinogram is calculated, back projection is performed similar to a parallel beam sampling of the projections.

Another approach is to reconstruct the fan beam projections immediately by means of a geometrically corrected FBP. See Kak [27] and Hsieh [2] for more details.

Filtered back projection (FBP)

Because projections are sampled angularly, more information is available on the central part of the object than on the outer parts. Had this pattern of information been directly reconstructed, the image will appear blurry and unfocused due to the unbalanced distribution of the information to the image pixels. The amount of information on the object decreases with the distance from the center of the field of view. Therefore, the projections should be weighted in order to reconstruct a representative image. See Figure 16 for illustration.

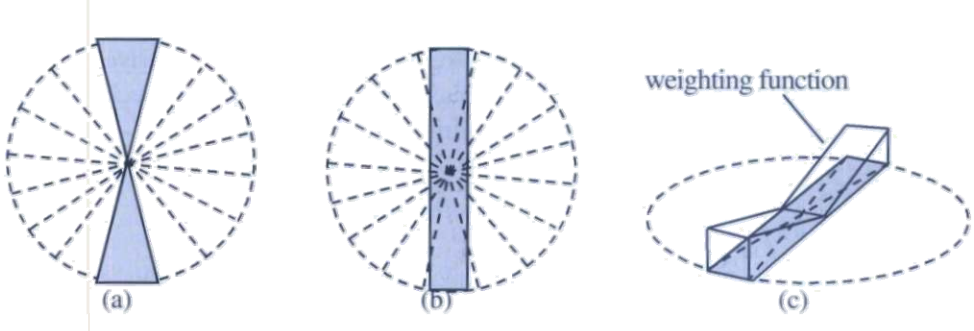

Figure 16. Illustration of the concept of filtered back projection. (a) Ideal distribution of information in the Fourier domain where projections are sampled angularly. (b) The actual information distribution for a parallel beam projection. (c) The weighting functions in the Fourier domain that is needed to approximate ideal information distribution.

For reconstruction purposes, the projections are convolved with the kernel (k) such that $FT[k] = K$ to reconstruct a blur-free image as:

$$\mu(x, y) = FT_2^{-1}[K \cdot FT[p]]. \tag{2.34}$$

This type of reconstruction where the projections are weighed by an extra convolution kernel (k) is called Filtered Back Projection (FBP). The application of FBP to the simple example in Figure 11 is shown in Figure 17.

The images vary with the used kernel. Kernels are usually described in the frequency (Fourier) space. Noise and edge definition are associated with high frequencies. Figure 18 shows the effect of choosing the Ram-Lak and Shepp-Loggan filters on a reconstructed image.

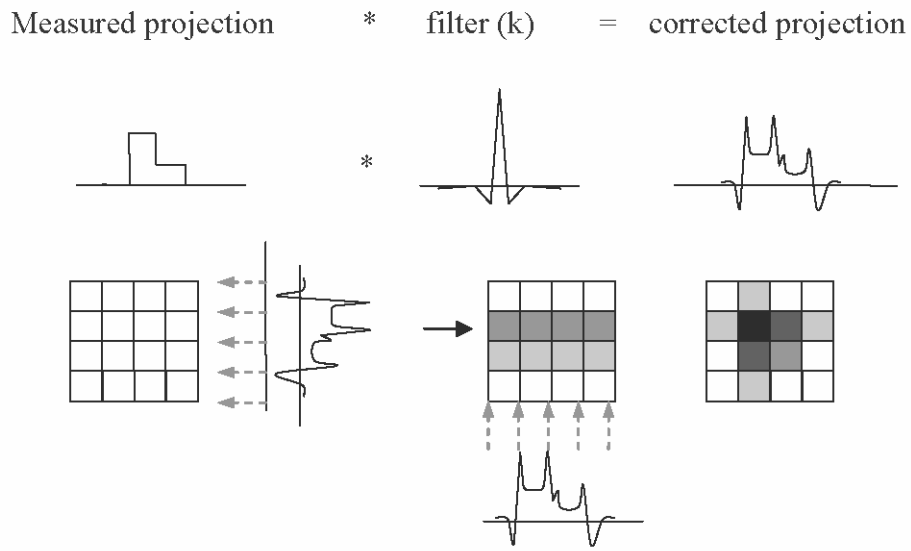

Figure 17. Schematic diagram representing the FBP algorithm. The measured projections are convolved with a filter then back projected. The process is repeated for all measured projections. The reconstruction finishes once all projections are processed once.

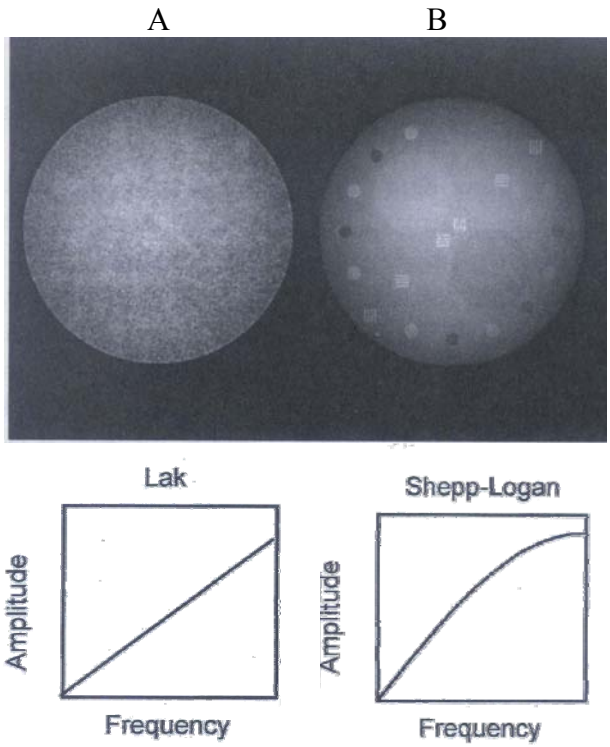

Figure 18. Effect of choosing different kernels on reconstructed image. A: Ram-Lak filter allows all the noise to be translated into the image. B: the Shepp-Logan filter dampens the high frequency contribution of the noise and the image is clear [24].

2.2.6. Image presentation in CT-numbers (Hounsfield Units)

When the image is reconstructed ($\mu(x,y)$ is calculated), the image can be represented in grey scale. The gray values or CT-numbers are the attenuation coefficients of the object relative to the attenuation coefficients of water.

$$\text{CT} - \text{number} = 1000 \times \left(\frac{\mu - \mu_w}{\mu_w} \right) HU \qquad (2.35)$$

Here, μ is the linear attenuation coefficient and μ_w is the linear attenuation coefficient for water.

By definition, the CT-number of water equals zero. The attenuation coefficient of air is nearly zero; therefore the CT-number of Air is -1000 for any measurement condition. There is no limit on the higher end of the CT-number scale, however most manufacturers set the scale between -1024 and +3071 HU for a 12-bit representation of the CT-number. CT-numbers larger than the maximum (+3071 HU) are set to the maximum value as in the case of metals. The CT-values can be used to identify the different tissues and bone types (Figure 19).

Despite the clear definition of CT-numbers, the exact value of CT-numbers varies depending on the settings of the CT scanner except for water and air. The variation is stronger in bone materials than in soft tissues. Fortunately, some of the factors above cause a systematic deviation that can be measured and corrected for, as in the cases of X-ray tube energy and beam hardening.

The value of CT-numbers is also affected by measurement set up like the kilovolt setting of the X-ray tube, the material and size of the scanned object, the reconstruction Field Of View (FOV) and finally on temperature[13][3][15]. It is also known that the daily electron density calibration of the CT machine affects the HU values [28]. Furthermore, the stochastic nature of X-ray interactions implies that the measured CT-numbers are average values. The noise in an image pixel is defined by the standard deviation of the measured CT numbers. The noise decreases with increasing number of photons assigned to the pixel. It is inversely dependent on the X-ray tube current, slice thickness and data acquisition duration.

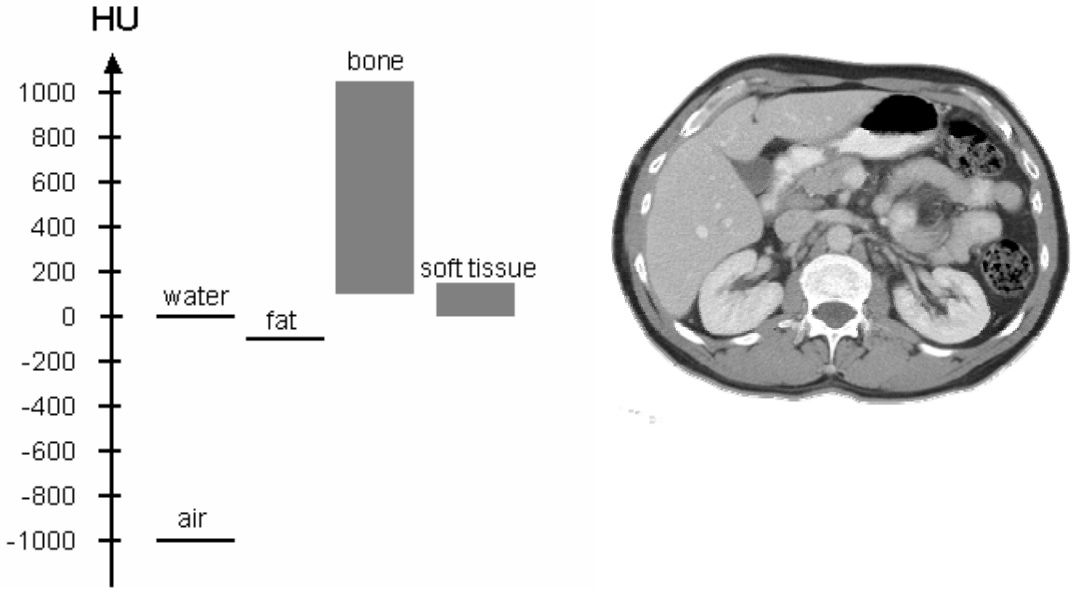

Figure 19. Scale of CT-number and the corresponding tissue types. To the right, a sample CT image of the abdomen [19].

Artefacts such as beam hardening, metal, partial volume, truncated projections, detector gain (ring artefacts), scatter and motion artefacts arise from incorrect sampling of projection data and affect the image quality along with the value of CT numbers. Fortunately, most artefacts can be corrected by using hardware add-ins or post processing of the signal.

3. MATERIALS AND METHODS

3.1. Investigated CT scanners

The performance of five CT scanners from different vendors was investigated. The scanners included a Philips Mx8000 IDT scanner, a Toshiba Aquilion16 scanner, a Siemens Sensation 4 scanner, a Siemens Sensation Open scanner and finally a Siemens Emotion Scanner. The scanners were operated using the standard imaging protocol for radiotherapy treatment. A summary of CT-settings used for the measurements are listed in Table 1.

The Emotion CT unit was simulated based on the design data provided by Siemens for the Emotion scanner series[2]. The data provided by Siemens included material specifications of the different filters and the detectors. Geometrical parameters concerning X-ray tube, filters, anti-scatter grid and the detector arc were provided. The distances from the focal spot to the detectors (SDD) and from the focal spot to the center of scanner (SSD) were also provided.

The scanner is equipped with a DURA 352-MV X-ray tube, two beam shaping filters (a bow-tie filter made from Al and a Teflon filter). The detector-arc is made out of 672 elements. The material of the detector elements is Gadolinium Oxysulfide (Gd_2O_2S) for which the energy response function has been published in the work of Heismann et al. [29] (Figure 32 below).

The Emotion CT scanner from Siemens is a third generation CT scanner which is also a prototype machine used for Image Guided Radio Therapy. It is located in a treatment room at the DKFZ, adjacent to a Siemens linear accelerator. The CT-gantry is set on rails whereby the gantry can move along the z-axis while the table is fixed. This special arrangement was designed for accurate patient positioning at the radiotherapy treatment table (see Figure 20). The scanner is located in a treatment room where 12-25 patients receive treatment daily. Therefore access to perform experiments on the CT-scanner is limited.

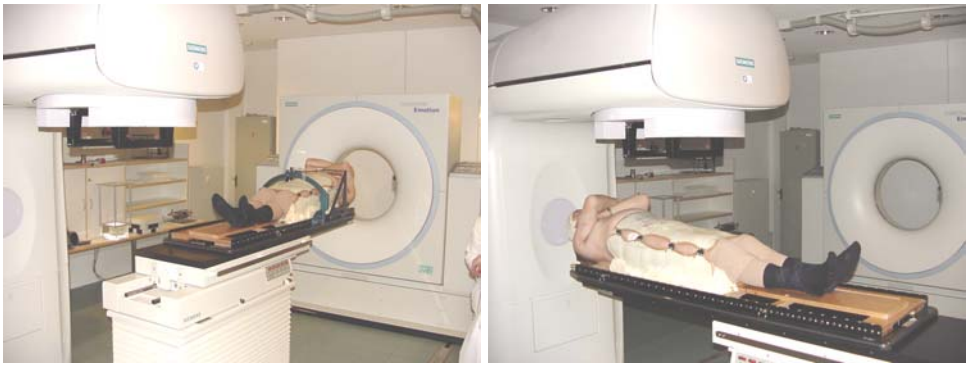

Figure 20. Overview of the arrangement of Linac and CT in the treatment room. On the left side, the patient is in scanning position, on the right side, he is in treatment position. To change from one to the other, a manual non-isocentric rotation of the couch is required (courtesy of Dr. Simeon Nill from DKFZ).

Measurements of CT-numbers of known substitutes were performed at all the investigated scanners. Measurements of CT-numbers of tissue samples were performed at the Siemens

[2] The confidential data were obtained from Siemens within the framework of a collaboration contract signed by "Siemens Medical Systems" and the Medical Physics department including a non-disclosure agreement.

Sensation 4 and Siemens Open CT scanners. The energy spectrum of the X-ray tube of the Siemens Emotion CT scanner was also measured.

3.2. Investigated substitutes and phantoms

Thirteen electron density substitutes, manufactured by Gammex-RMI (Middletown, WI, USA), were chosen as tissue equivalent substitute materials. The substitutes hardly contain heavy elements (Z >20) and imitate both the chemical composition and the electron density of real tissues [28][30]. The range of Carbon ions and CT-numbers were measured in the Gammex substitutes. Cylinders of substitutes of 1.4 cm radius and 6 cm height were used for CT measurements. Disks of 1.4 cm diameter and 1 cm thickness were used for range measurements. The composition of the different substitutes was also modelled in the simulation of the CT scanner.

Another group of substitutes (H-materials) has been experimentally investigated by Jäkel et al. [7]. H-materials are based on polyethylene and simulate tissue in terms of photon absorption, but their elemental composition contains high percentages of silicon and tin. The substitutes were found unsuitable for calibration purposes because their stopping power ratio was considerably higher than tissue. In the scope of this work, the elemental composition of the H-material was modelled for the calculation of CT-numbers based on the data provided by Jäkel et al. [7].

Sixteen fresh pig-tissue samples, a human cortical bone sample and a spongy cattle bone sample were used to investigate the suitability of Gammex substitutes and H-materials for CT calibration. Tissues were cleaned, sliced and stacked into cylindrical PMMA tubes (5 cm length and 2 cm radius). Bone samples were cut in the required dimensions but were not kept in PMMA tubes. The CT-numbers and range of Carbon ions was measured in tissue probes (cylinders of PMMA filled with tissue) and bone samples.

Two homogeneous PMMA cylindrical phantoms (Figure 21) were used for CT measurements. Their outer radius was 8 cm to simulate beam hardening in a patient's head. The inner radius of the phantoms were designed to fit various substitutes and tissue probes.

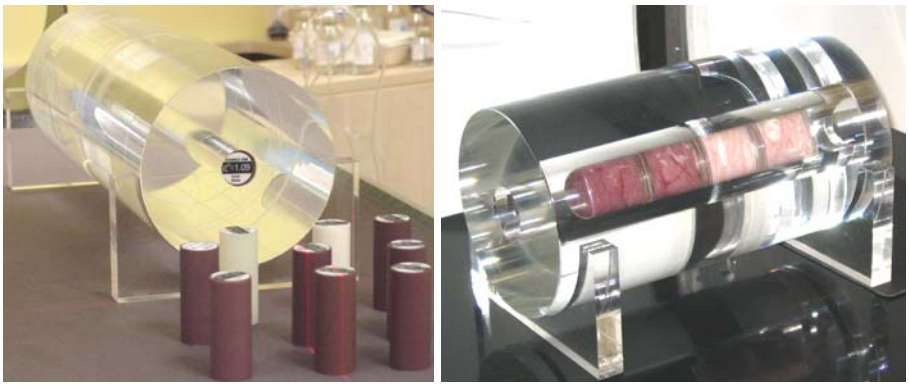

Figure 21. Cylindrical PMMA phantom with Gammex substitutes (left) and with 2 muscle and 2 brain tissue probes (right). The phantoms were used to measure the CT-numbers at the CT-scanners.

Furthermore, water equivalent materials such as PMMA, solid water and RW3 were simulated to investigate their equivalence to water. RW3 is a commonly used phantom material,

manufactured by PTW in Freiburg, Germany. Air and water were simulated as a reference to present the simulated results in terms of Hounsfield Units (see section 2.2.6).

3.3. Measurement of CT-numbers

Gammex electron density substitutes (see section 3.2) were inserted into the PMMA phantom (Figure 21) to measure CT-numbers. The phantom was positioned in the centre of the gantry with the cylinder axis aligned to the z-axis of the CT as seen in Figure 22.

Figure 22. Emotion CT scanner with the PMMA phantom, positioned for CT-value measurements.

Regions of interest (ROI) were defined in the center of the CT-images of the phantom with substitutes. An average diameter of the ROI is 1.8 cm. For a 256x256 pixels per image of the head (FOV is 287 mm diameter), the ROI contains 200 pixels. The number of pixels per ROI rises to 800 for 512x512 pixels in the image with the head protocol (287 mm FOV). The gray value of pixel is its CT-number. The average and standard deviation of CT-numbers of the image pixels within the ROI were calculated using the software tool kit of the CT-scanner.

The default scanner for treatment planning with Carbon ions is a Siemens Sensation 4 scanner. More than 90% of the patients treated with Carbon ion radiotherapy at GSI were treated for head and neck tumours. Hence, the default protocol for imaging is for head imaging. The parameters of the default imaging protocol are shown in bold letter in Table 1, which summarizes the standard imaging protocol for radiotherapy treatment planning of the different scanners.

The measurements investigated the effect of varying the slice thickness (Siemens Sensation 4), reconstruction kernel (Siemens Sensation 4, Siemens Open, Toshiba Aquilion16, and Philips Mx8000 scanners) and the effect of FOV (Siemens Sensation 4, Siemens Open, Toshiba Aquilion16 and Philips Mx8000). The effect of voltage setting of the X-ray tube was investigated at the Siemens Emotion scanner. Finally, the head protocols of the different scanners were compared.

The CT numbers of fresh pig-tissue samples, a human cortical bone sample and a spongy cattle bone sample were measured using a Siemens Sensation 4 scanner and Siemens Sensation Open

scanner. Tissues probes and bone samples were inserted into PMMA phantoms during CT-measurements (see Figure 21).

Table 1. Summary of CT scanners used for measurement of CT-numbers of Gammex substitutes. Full list of measurement parameters and results are available in Appendix A. The default scanner is the Siemens Sensation 4 CT; its default settings are in bold letters.

CT scanner	X-ray tube voltage (kV)	X-ray tube current (mAs)	Slice thickness (mm)	Filter "Scanner notation"	FOV (mm)
Siemens Sensation 4, Radiotherapy Dept., University clinics, Heidelberg	**120**	**300**	**3**	**H40s**	**287**
	120	300	3	H40s,H60s	500
	120	300	1,5	B40s	500
Siemens Open CT, Radiotherapy Dept., University clinics, Heidelberg	120	300	3	H40s	287
	120	300	3	H40s	500
	120	300	3	B40s,B60s	500
	120	300	3	B40s,B70s	500
Siemens Emotion, Radiotherapy Dept., DKFZ, Heidelberg	80	200	3	H40s	287
	110	200	3	H40s	287
	130	200	3	H40s	287
Toshiba Aquilion16, Radiology Dept., DKFZ, Heidelberg	120	300	3	FC10	500
			3	FC48	500
			3	FC10, FC48, FC69	240,320,400,500
Philips Mx8000, Radiology Dept., Mainz	120	300	3	C,D, EC	180, 240, 320, 400, 500

3.4. Range of Carbon ion in tissue and substitutes

The WEPL (defined in section 2.1.2) was measured in Gammex substitutes and in real tissues. The experimental setup for WEPL measurements consists of a water column of variable thickness between two parallel-faced ionization chambers. The signal of the exit chamber is measured relative to the signal of the entrance chamber. The relative signal is given as a function of the thickness of the water column. For further details concerning the measurement set up see Jäkel et al. [7].

WEPL measurements of the substitutes were carried out using a pencil beam of 184 MeV/u and 270 MeV/u Carbon ions with a beam width (FWHM) of about 10 mm. The length of the water column was changed in steps of 100 μm, which reflects the uncertainty in the thickness of the water column. Similar measurements using a 270 MeV/u Carbon beam were used to measure the water equivalent range of animal tissues and bone samples.

The WEPL measurement –for a given beam energy– starts by measuring the depth-dose profile of Carbon ions in water without any probe in the beam path. After recording this reference peak, a sample of the material is placed in front of the water column to measure another depth-dose profile, for the same beam energy. The difference between the position of the measured Bragg-peak and that of the measured reference peak (peak-shift, see Figure 5) is then divided

by the thickness of the sample to calculate the relative range of the sample. The thickness (T) of probes along the beam path is measured using a Vernier calliper. The average of several thickness measurements is recorded. The uncertainty of the thickness measurement was 0.1 to 0.2 mm.

The reported uncertainty in a single measurement of WEPL is the difference between the highest and lowest acceptable peak-shifts (σ). Inhomogeneity causes more range variation which in turn causes a broadening of the Bragg peak. As a result, the uncertainty of the WEPL increases with inhomogeneity.

The WEPL can also be simulated using Shield-HIT v.2. which is a Monte Carlo code for Carbon ion interactions. For more information see Appendix D.

3.5. Measurement of energy spectra using a Compton spectrometer

To calculate CT-numbers for known geometry and material composition, a complete CT system was simulated using the Monte Carlo Code BEAMnrc (see section 3.6.2). The system considered for simulation was the Siemens Emotion Scanner which is equipped with a DURA 352-MV X-ray tube.
The input data for the simulation code was the energy spectrum of the X-ray tube of the CT scanner. Energy spectra of the X-ray tube were simulated by Romanchikova [31]. Another set of energy spectra was provided by Siemens. The simulated spectra were based on the geometry and composition of the X-ray tube components. The spectra from Siemens were calculated by an analytical program. No information on the algorithm and no estimate on the uncertainty of the spectral data was provided.

Neither the simulated nor the Siemens spectra were benchmarked against experimental data. Therefore, it was necessary to measure the tube spectra with high energy resolution in order to compare measured spectra with the simulated and provided spectra. The energy resolution of a detector is defined as the full width at half the maximum (FWHM) of a measured signal divided by the energy of the center of the peak. In general, semiconductor detectors offer the best energy resolution compared to other types of detectors.

3.5.1. Semiconductor crystals as radiation detectors

The energy gap between the valence and the conduction band in the semiconductor crystals is about 1 eV. When reverse biasing is applied to a semiconductor junction, the charge carriers are drawn away from the junction and no current will be recorded. However, when the junction is irradiated, electrons are excited to the conduction band leaving holes in the valence band. The applied reverse bias sweeps the charge pair (electrons to the n-side and holes to the p-side) causing a current pulse. The amount of charge generated by an interaction is proportional to the energy deposited by the incident radiation.

The noise in semiconductor detectors is due to electronic noise, thermal excitations, inherited statistical fluctuations in the number of charges created per quanta of incident X-rays and incomplete charge collection.

Thermal excitations of the electrons in the valence band are avoided by cooling the semiconductor crystal down to very low temperature. The signal broadening due to statistical

fluctuations is proportional to the incident energy (which in turn is proportional to the number of created charge pairs). Incomplete charge collection is mainly due to charge recombination while the charges travel to the electrodes. The smaller the crystal is, the lower the rate of charge recombination because the charges travel less distance to the electrodes.

Small detectors have a smaller capacitance and therefore smaller electronic noise. On the other hand, large crystals have a larger effective volume and higher efficiency of detecting high energy radiation than small crystals.

For low X-ray energies, there is no need for a large effective volume. In the same time, the signal is small because the energy of incident photons is small. Therefore, it is important to keep a high ratio of signal to noise. Therefore, small planar semiconductor detectors give the best energy resolution performance for detecting X-rays and low energy gamma rays [32].

The minimum time required for a charge carrier to travel a distance of 1 cm in a Germanium crystal is about 100 ns [32]. The minimum temporal separation which is needed to record two events as two separate pulses is called dead-time. It is proportional to the time required by charge pairs to reach the electrodes. Photons incident during the dead-time can not be identified as separate events, if recorded. The higher the count-rate is, the higher the possibility of recording pulses during the dead-time and the larger the pile-up of the signal. When the signals are piled, it is impossible to distinguish the individual events. Large signal pile-up could paralyse the detector system when used at high count-rates.

To avoid pile-up complications, a maximum count-rate of 10^7 photons per second is recommended for semiconductor detectors. However, 10^{17}-10^{19} photons/sec are produced with X-ray tube settings of 10-300 mAs and assuming 0.5% efficiency of the X-ray tube. Collimation and measurement at large distances can reduce the count-rates by several orders of magnitude. However, the geometrical arrangement of a CT machine makes it is impossible to perform direct measurements since the distance between the focal spot and the center of FOV is 50-70 cm. As a result, semiconductor crystals can not be used in the primary beam of a CT-scanner in clinical conditions.

3.5.2. Compton spectrometer

In 1987, Matscheko and Ribberfors suggested the use of a Compton spectrometer for the measurement of X-ray spectra of clinical X-ray tubes [33] [34]. The design of the spectrometer is thoroughly discussed in [35][36]. The collimator shown in Figure 23 was manufactured by RTI Electronics (Mölndal, Sweden) [37]. In brief, the highly collimated incident beam is scattered of a PMMA rod. The scattered beam is further collimated before it reaches the detector crystal. The dominant interaction process in PMMA for photons of CT energy is Compton scattering where the incident photon scatters off a loosely bound electron. The photon loses part of its energy to the electron which leaves the atom. Conservation of energy and momentum imply that the energy of the scattered photon (E') is given by the incident photon energy (E) and the scattering angle (θ) (see equation (2.12)).

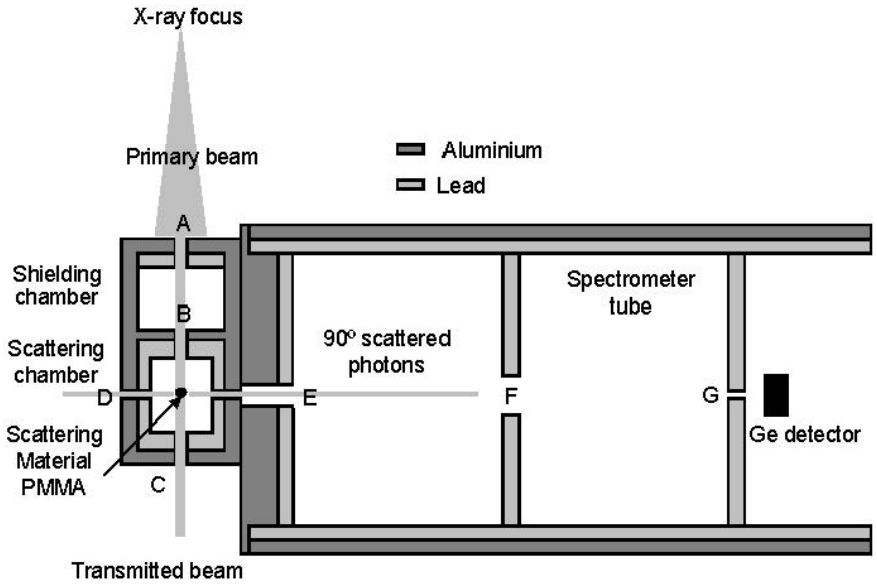

Figure 23. Schematic diagram of the X-ray Compton spectrometer (commercial name is Spectro-X). Incoming X-rays are collimated to a thin parallel beam by the collimators A and B. The beam then hits a thin PMMA rod. Only photons which are scattered by 90° angle from incident beam reach the Ge detector. The scattering rod of PMMA is kept in the heavily shielded scattering chamber. The chamber has 4 openings (B, C, D and E) to prevent backscatter of the photons to either the primary or 90° scattered beam.

The scattering rod is kept in the shielded scattering chamber and only the 90° scattered beam is detected by a Germanium detector. The scattering chamber has 4 collimated openings to prevent backscatter of the photons to either the primary or 90° scattered beam.
The Compton spectrometer reduces the intensity of the incident beam by about 5 orders of magnitude by means of collimation of the incident beam and by about 6 orders of magnitude by collimation of the scattered beam. The intensity of the scattered photons varies as a function of the scatter angle; it is minimal when the beam is scattered by 90°.

Matscheko and Ribberfors 1989b [38] also suggested a generalized algorithm for reconstructing the initial spectrum. In principle, it is possible to calculate the energy of the incident photons using equation (2.12) since the angle at which the photons are scattered is known (90°). The algorithm is accurate for initial energy spectra between 7 and 200 keV . The algorithm can also relocate the characteristic X-ray peaks in the spectra. However, the relocation (deconvolution) of the characteristic peaks is highly sensitive to noise in the spectrum therfore, it is limited to two pre-defined regions of interest: 57.8-60.0 and 66.3-69.8 keV to find the K-lines of tungsten.

3.5.3. Measurement setup

The scattering rods were 4.0 mm and 2.2 mm diameter and were made of PMMA. A thick scatterer allows the collection of higher signals since more scattering events of the primary photons are expected. On the other hand, a thin scatter allows better energy resolution since there are less multiple scattering events within the rod than in a thick scatterer.

The detector used for the spectral measurement is a low energy Germanium detector (LEGe) manufactured by Canberra. The crystal (n-type high purity Germanium) is 10 mm thick with an active area of 200 mm^2. The opening window is made of 0.5 mm thick Beryllium, 5 mm from the crystal, which allows the detection of low energy photons. The detector is portable with a

small attached dewar for liquid nitrogen (see Figure 24). The detector is read-out using the digital signal analyser DSA2000 [39].

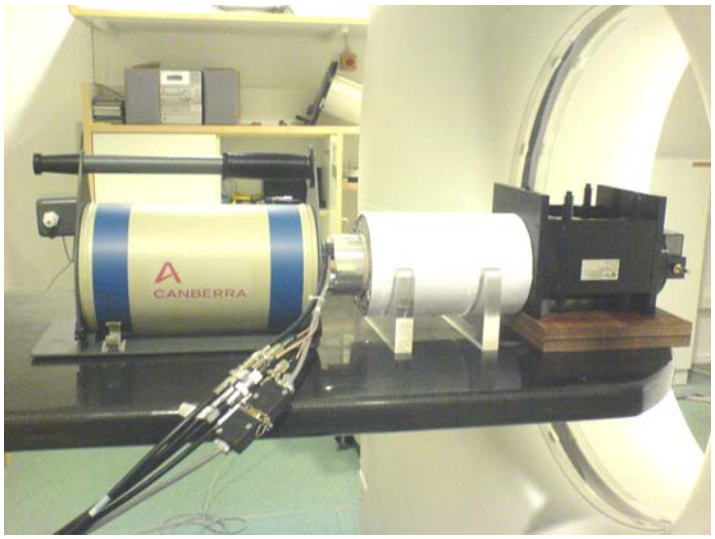

Figure 24. Set up for the measurement of the spectrum of the X-ray tube at the Emotion CT. From left to right are the dewar for the portable LEGe detector, detector cryostat under lead shielding(white) and the Spectro-X collimator (black).

Measurements performed during the preparation phase indicated that the thin scatterer collected only 28% of the signal collected by the thick scatterer with comparable energy resolution. Consequently, the thick scatterer was used to accelerate the detection of sufficient counts while minimizing the time for measurement at the CT-machine. The time needed for measurement was critical because the CT is located in a treatment room which also contains a radiotherapy accelerator.

In the simplified picture of Compton interactions, the electrons are free and stationary. In reality, the electrons are bound to the atoms and have orbital velocities. The distribution of orbital velocities lowers the energy resolution of the measured Compton spectrum. The energy resolution is also affected by the multiple scattering events which broaden the measured spectra and the energy resolution of the Ge detector [35][33][36].

The energy broadening caused by multiple and coherent scattering is estimated by 0.3 keV. The distribution of the velocity of shell electrons in the scatterer is estimated by 0.75 keV [33][36].

The optimum resolution of the detector is 195 eV at 5.9 keV (3.3%) and 520 eV at 122 keV (0.4%)(detector data sheets). The measured resolution of the 59.7 keV line of ^{241}Am was 0.8%. The energy calibration of the detector was performed using ^{241}Am and ^{133}Ba radioactive sources. The resulting energy per channel was 0.173 keV.

The spectral distribution was measured for 3 nominal tube settings (80, 110 and 130 kV) in the center of the FOV. The energy spectra were also measured for a 110 kV tube setting at 3 off axis positions (2.8, 7.0 and 14.0 cm from center of FOV) as shown in Figure 25. For each of the settings used for spectral measurements in Table 2, a separate background measurement was performed. Six separate measurements of the background were performed in total.

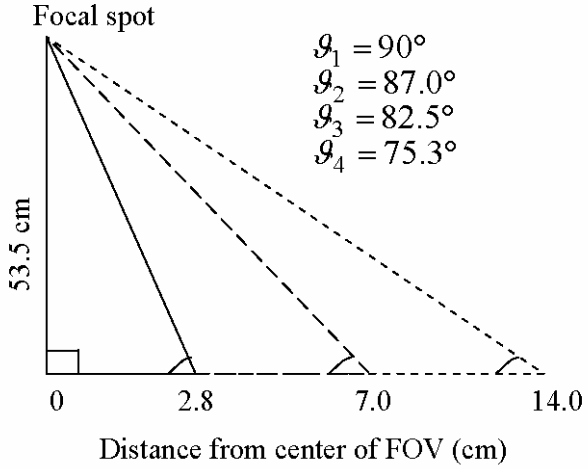

Figure 25. Schematic diagram showing the position of the Compton spectrometer with respect to the focal spot of the X-ray tube. The values of the angles are the required tilting of the entrance chamber to achieve 90° angle between focal spot and the LEGe detector.

The background was measured by removing the scatterer from the scattering chamber (Figure 23) and measuring the resulting spectrum with beam on. The photons collected by the detector in this manner did not originate from the scatterer and were considered as background[3]. The natural background is already taken into consideration by using the above method.

The scanner was operated in a stationary mode i.e. the X-ray tube was held at one position in the gantry and was not allowed to either rotate or move in the z-direction. X-rays were extracted in pulses. 100 mAs of electrons hit the target per pulse. The pulse duration is 1.5 sec. 25-50 pulses were used to collect sufficient counts. The tube heat was a limiting factor on the number of pulses. Tube heat was maintained below 60°C to avoid any damage to the tungsten target. All the measurements were performed using a large focal spot (0.2 x 0.7 mm). Using the small focal spot (0.2 x 0.5 mm) increased the dead-time of the measurement to 20-30%.

3.5.4. Comparison of energy spectra

The measured spectra were compared to the simulated and Siemens spectra using three different properties: the position of the characteristic peaks, the K-ratio and the mean energy of the spectra.

The target material is a mixture of Tungsten ($Z = 74$) and Rhenium ($Z = 75$). However, the percentage per weight of rhenium is very small and the characteristic lines are mostly the K-lines of tungsten.

The K-ratio was defined as the number of characteristic photons relative to the total number of photons in spectrum. The characteristic lines were defined between 56 and 61 keV for the K_α and between 65 and 71 keV for the K_β lines.

[3] This method slightly overestimates the background radiation as photons scattered in the air volume substituting the missing scatterer are also regarded as background [37].

Table 2. Settings of CT-scanner and Compton spectrometer for measurement of X-ray spectra.

Parameter/Measurement	1	2	3	4	5	6
Nominal voltage setting	80	110	130	110	110	110
Actual voltage settings (kV) [4]	79.2-79.4	101.8-102.0	121.6-121.8	101.8 - 102.0	101.8-102.0	101.8-102.0
Tube current (mA)	100	100	100	100	100	100
Rotation mode	Static	Static	Static	Static	Static	Static
Pulse duration (sec)	1.5	1.5	1.5	1.5	1.5	1.5
Number of pulses	50	50	25	10	25*	25
Angle between central beam axis and entrance chamber	0°	0°	0°	3.0°	7.5°	14.7°
X-ray tube position	180°	180°	270°	180°	180°	180°
Distance from center of FOV (cm)	0	0	0	2.8	7.0	14.0

The mean energy was calculated as:

$$\overline{E} = \sum_i w_i \times E_i \Big/ \sum_i w_i \,, \tag{3.1}$$

where w_i are the counts at the energy bin (i) with the energy E_i. w_i are normalized such that

$$\sum_i w_i = 1 \,. \tag{3.2}$$

To calculate the uncertainty in the mean energy, assume that:

$$\Delta w_i = \sqrt{w_i} \,, \tag{3.3}$$

Then,

$$\Delta\overline{E} = \sqrt{\sum_i \left(w_i \times (E_i)^2\right)} \tag{3.4}$$

3.6. Monte Carlo simulation of CT-numbers of the Siemens Emotion CT

Literature described simulations of CT scanners have been driven by:

- Optimisation of scanner design,
- Minimization of radiation dose to the patients,
- Improvement of image quality by studying artefacts, mostly scatter.

The approaches varied with the purpose of the simulation. Simulation methods focused on calculating the energy spectrum and beam profile of the X-ray tube of the scanner.
There are several approaches to calculate the energy spectrum of a CT including empirical models and Monte Carlo simulations. The accuracy of the various approaches have been studied by Bhat et al. [40], Caon et al. [41] and later by Ay et al. [42] and [43].

[4] The air calibration of this particular CT scanner is maintained by changing the voltage settings of the X-ray tube without notifying the user. Exact voltage settings are only accessible when the scanner is operated in service mode.
* The background was measured using 10 pulses only for this particular set up because of excess tube heating. The background for all other measurements was measured for the same number of pulses as the main measurement.

Another important aspect of the simulations is calculating the effect of beam shaping filters. Several methods have been used to simulate CT filters. The approach of creating a look-up table containing information on the angle of incidence and the amount of material in the beam path was used in the work of Atherton and Huda [44] and more recently in the work of Jarry et al. [45]. In their work, the information was transferred into weighing factors [45] or into a look up table of linear attenuation coefficients as a function of angle [44]. Full Monte Carlo simulation of the filter geometry was carried out by Salvado et al. [46] and Tzedakis et al. [47].

The advantage of the Monte Carlo (MC) approach is that the MC code handles the variation of energy and position for each particle based on validated physical models. It takes into account the presence of different materials in the beam path and their geometrical boundaries. An equivalent analytical approach can not handle the interactions on the level of single photons without referring to simplified models to give a general description. The disadvantage of MC approaches are that they require long calculation times and that the user has to rely on the physical models provided in the code, unless the user develops its own (Rogers [48]).

3.6.1. Simulation work flow

The aim of this work is to calculate CT-numbers from well defined projections. Therefore, CT projections were simulated using the MC code BEAMnrc/EGSnrc (see 3.6.2) and images were reconstructed from the simulated projections.

The MC simulation was divided into 2 parts. The first part deals with X-ray production and filtration (CT1 in Figure 26). The second part deals with the transport of photons through phantoms and substitutes (CT2 in Figure 26). Each part was terminated by a so-called scoring plane. Phase space files (PHSP) were calculated at each scoring plane. By dividing the simulation into different sections, one only needs to perform the simulation of X-ray generation and filtration part (CT1) once and use it, repeatedly, as input to the second part (CT2).

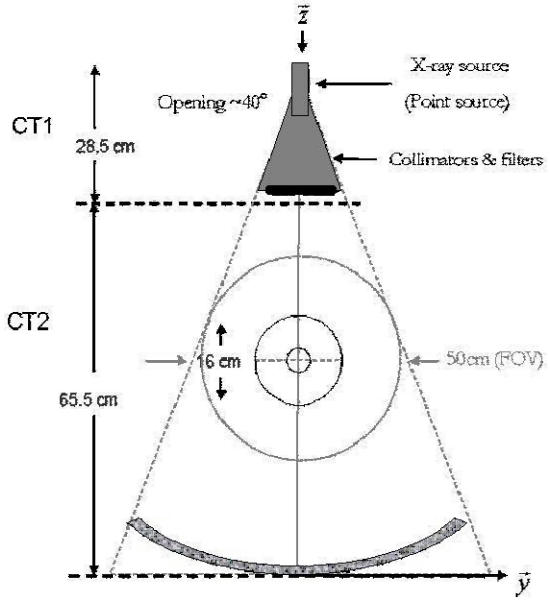

Figure 26. Scheme of simulated CT unit and phantom. The simulation was divided into 2 parts. The CT1 part deals with X-ray production and filtration. The CT2 part deals with the transport of photons through phantoms and substitutes.

The output of the MC simulation is a phase space file where the energy of the photons, position and incidence angles are stored. However, one needs projection data to perform the

reconstruction and acquire CT-numbers. Projections are defined as $-\ln(I/I_0)$ for each detector element (see 2.2.4). Calculating projections from PHSP involves the sub processes of sorting the photons into detector elements, accounting for detector response, and finally representing the signal in raw data format for projections ($-\ln(I/I_0)$). Scatter and beam hardening corrections are applied. Images are reconstructed from many projections using a PC-based FBP algorithm with a ramp-Lak filter (see Figure 18-A). Average CT numbers were calculated by defining regions of interest (ROI) in the reconstructed images. The CT-numbers calculation chain is shown in the Figure 27.

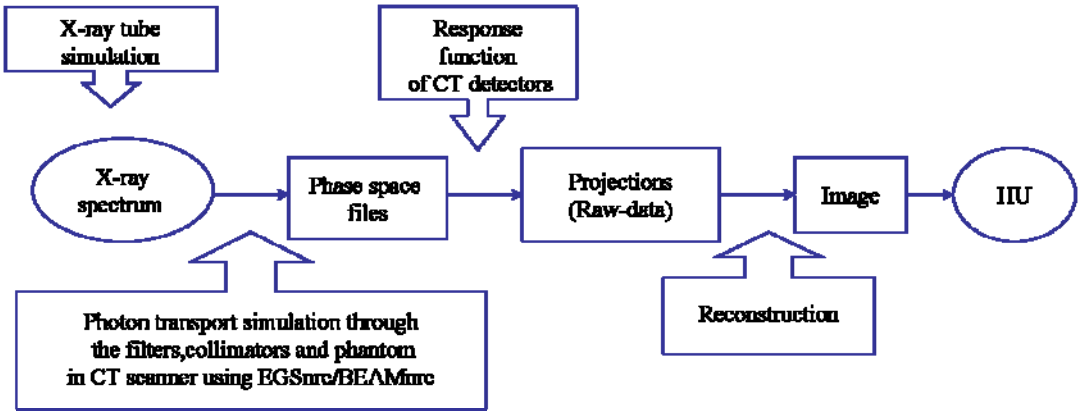

Figure 27. Scheme of the calculation of CT-numbers: from X-ray spectrum to CT-numbers (HU) that are extracted from the CT-image.

3.6.2. MC code (BEAMnrc/EGSnrc)

To correctly describe particle interactions with matter, one needs to determine the mean free path of the particle between interactions and to determine the type of interaction which will take place at the end of the mean free path. Reasonable determination of both parameters requires the use of reliable random number generators. The random numbers are used to estimate probabilities of interactions based on detailed theoretical models and experimental data of the interactions. Another important issue in MC simulations is the crossing of geometrical boundaries. If the particle changes media, its mean free path and the interaction cross sections also changes. The ability of MC codes to accurately reproduce physical interactions and their flexibility in modelling geometrical designs distinguishes the different codes.

MC codes for medical physics applications

Most MC codes were originally designed for particle or astrophysics applications. The trend to use MC simulations in answering medical physics questions has intensified with the presence of powerful codes and continuous rise in computing power. The most commonly used MC codes for electron and photon transport in medical physics are EGS, MCNP, GEANT and finally commercial codes similar to VMC++ .

It is difficult to compare the different codes since they handle physics differently. The comparison requires considerable familiarity with the different codes to correctly model the tasks while using the codes at their best. Most comparisons between the different codes are based on dose calculations and measurements (Carrir et al. [49] , Chibani and Li [50] and Verhaegen et al. [51]).

Comparisons of different versions of the same code are also important to evaluate its strengths and weaknesses (see the work of Verhaegen [52]and Kawrakow [53] for the EGS code). For example, dose perturbations due to high-Z heterogeneity were successfully modelled using EGSnrc for photon energies up to 1 MeV [52]. Other codes and earlier versions of the EGS code have failed to correctly reproduce measured dose results near the interface of heterogeneities.

Off axis Bremsstrahlung has also been studied by different versions of the EGS code. It was found that the EGS4 version underestimated the characteristic lines (Bhat et al. [54], Ay et al. [43], Rogers et al. [55]). The EGSnrc version has been equipped with the modified Electron Impact Ionization library (EII) which calculates the intensity of characteristic lines more accurately than previous versions (Kwarakaw [56]).

The EGSnrc code has the most advanced interaction library for physics modelling of electron, positron and photon interactions in the low energy range applications (1-150 keV) [51] [52] [53] [57] [58].

EGSnrc

The Electron Gamma Shower system (EGS) was developed as a tool for high energy physics in the Stanford Linear Accelerator Center (SLAC). It used to cover the energy range 100 MeV to 100 GeV. The code was upgraded for medical physics applications by the collaborative works of the National Research Council of Canada (NRC) and SLAC. The EGS4 version of the code was able to model interactions in the energy range 10 keV to 50 MeV [58][48]. Further improvements solved the problem of interactions near geometrical boundaries (Kawrakow [53]). The developments by the Japanese KEK group of the low energy physics aspects of the code (Namito et al. [59]) were also included in the EGSnrc version.

The EGSnrc manual (PIRS-701 [58]) describes in detail how the following physical processes are implemented:

- Annihilation of positrons at rest or in flight
- Inelastic Moller scattering of electrons from atomic electrons
- Inelastic Bhabha scattering of positrons from atomic electrons
- Bremsstrahlung production by electron or positron interactions with either nuclei or atomic electrons
- Elastic single and multiple scattering from either nuclei or atomic electrons
- Pair production by photons
- Compton scattering from bound atomic electrons
- Photoelectric interactions with atomic electrons. The angular distribution of the Photoelectrons is sampled from the Sauter distribution.
- Reyleigh (coherent) scattering of photons from atoms
- The relaxation of the atoms after a vacancy is produced
- Relativistic spin effects can also be included in nuclear elastic scattering. The algorithms for relaxation events after Photoelectric and Compton interactions include detailed models for K, L and M shell fluorescence in any material. Relaxation by emission of Auger and Coster-Kronig electrons is also modelled. Electron binding effects can be taken into account in bound Compton scatter.

BEAMnrc

The general purpose tool "BEAM" was released in 1995 to facilitate the modelling of all types of radiotherapy accelerators as well as ^{60}Co and X-ray units (Rogers et al. [55] [60]). The physical processes, boundary calculations and random number generators have been based on the EGSnrc code. The code also has a variety of variance reduction methods which can accelerate the calculations by as much as a factor of 25. It also has the ability to run processes in parallel on any number of Linux machines (Rogers [48]).

The output of the simulation can be a Phase Space file (PHSP) where charge, energy and position of each scored particle are given. Its default format is binary. The BEAMnrc/EGSnrc package provides many general purpose tools to read, manipulate and analyze PHSP including: "Beamdp", "SRCXYZ", "readphsp" and many more [60].

The "Beamdp" is a sub routine in the BEAMnrc software package. It allows the user to analyze the PHSP files and calculate the energy and fluence distributions of the particles. "Readphsp" is another subroutine in the BEAMnrc package which allows the user to extract information from the binary PHSP files. It also allows the user to write the binary data of the PHSP into any other format defined by the user. "SRCXYZ" is a subroutine which can calculate the beam profile from the distribution of the particles in a given PHSP file.

3.6.3. Optimization of parameters used in the MC code

Optimization for low-energy interactions

The EGSnrc code follows the interactions of each history (electron or photon) until its energy reach a predefined threshold (cut-off). If the energy is less than the cut-off energy, the particle is no longer traced by the code and its energy is allocated to the absorbing medium. Setting high cut-off energies leads to loss of information on the low energy part. However, the cut-off energy also determines the computation time needed to finish simulation. The value of the electron cut-off energy (ECUT) and photon cut-off energy (PCUT) have been set as low as possible for reasonably long run-times of the simulation[5].

For ECUT, a value of 0.516 MeV was used in most of the simulations. However, electrons with a kinetic energy of 10 keV or less will not reach the detectors (50 cm away). As a result, an ECUT value of 0.521 MeV was used for simulating the filters in the CT1-part of the simulation. An ECUT value of 0.700 MeV was used to save calculation time in the region of collimators.

A PCUT value of 0.001 MeV was maintained throughout the simulation, since changing PCUT values did not affect the duration of the simulation.

Concerning interactions in the low energy range, the MC code allows the user to choose from a list of built-in interaction processes. Most interaction processes are switched on automatically. Low energy interactions processes which are not of importance for most applications (e.g. Rayleigh scattering) or refinement of present interactions (e.g. bound Compton scattering or allowing atomic relaxation after a vacancy is created in the electron shells) is left to the user.

[5] ECUT is defined as the sum of the rest mass energy of the elecrrn (0.511 MeV) and its kinetic energy. For example, an ECUT of 0.516 MeV is equivalent to a kinetic energy of 5 keV.

Omitting Rayleigh scattering decreases the counts in the spectral distribution by 3 %. Bound Compton scattering and electron relaxation effect affected the spectrum of simulated photons by 2 and 1% respectively (see Figure 28). As a result, bound Compton scattering, Rayleigh scattering and atomic relaxation processes are switched on during the MC simulations.

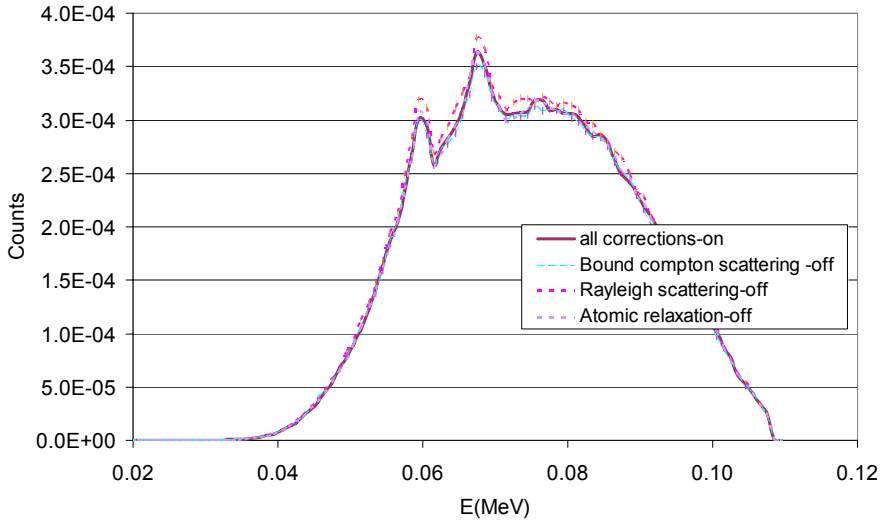

Figure 28. Effect of switching off X-ray interactions on the energy spectrum.

Other parameters of the EGSnrc code were set according to recommendations for low energy simulations. For more information on parameters definition see [58].

The parameters include:

- Global SMAX= 5,
- ESTEPE= 0.25,
- XIMAX= 0.5,
- Boundary crossing algorithm (BCA) = PRESTA−I,
- Skin depth for BCA= 0,
- Electron-step algorithm= PRESTA−II,
- Spin effects= On,
- Brems angular sampling= Simple,
- Brems cross sections= NIST,
- Bound Compton scattering = On,
- Pair angular sampling= Simple,
- Photoelectron angular sampling= On.

Generation of cross-section data for simulated materials (PEGS4)

The cross section data for each of the simulated material must be defined for the energy range of interest. The cross section database for BEAMnrc/EGSnrc is created using the code PEGS4. It also defines the low-energy thresholds for the production of secondary Bremsstrahlung photons and knock–on electrons (AP and AE, respectively). PEGS4 data also defines the interaction cross sections for the given energy range and for the selected interactions.

BEAMnrc/EGSnrc is equipped with two default PEGS4 data files. The default AE is either 0.521 or 0.700 MeV depending on the PEGS4 data files. The default AP is 0.010 MeV in both default data files. The cross section for low energy interactions such as Rayleigh scattering is not calculated for the default PEGS4 files. The files did not include most of the materials simulated (see 3.2). The simulated materials included Gammex and H-substitutes, Teflon and

Aluminium to investigate CT filters, phantom materials (PMMA, solid water and RW3) and finally air and water to represented results as Hounsfield Units (see 2.2.6). It was necessary to create a new PEGS4 file to include the interaction cross sections of the above material and to set appropriate threshold energies.

PEGS4 files for AE = 0.516 MeV and AP= 0.001 MeV, specifying the cross section of all interactions including Rayleigh scattering, were created for the material compositions presented in Appendix C.

3.6.4. Simulation set up

As presented earlier, the simulation was set up in two main parts: CT1 and CT2. The input to the CT1 part were pre-calculated tube spectra. The calculation of the spectra and set up of the different parts (Figure 26) are discussed in the following section.

X-ray source

The X-ray spectra of the DURA 352-MV Tube of the Siemens Emotion CT were simulated using the BEAMnrc code[6]. The optimisation of the parameters of X-ray tube simulation was carried out in the scope of the Diploma work of Romanchikova [31].

The simulations were performed for the X-ray tube voltages of 80, 100, 105, 110, 115, 120 and 130 kV. 10^8 incident electrons were used[7]. The total filtration was 0.2 mm Tungsten (while escaping the target), 0.6 mm Titanium and 3.0 mm Aluminium. X-ray spectra were simulated using the same parameters described in section 3.6.3 and a Pentium4 Linux PC with 3GHz CPU power and 1GB RAM. The run-time of the simulation was approximately one week of CPU time for each of the tube voltages. The efficiency of the X-ray tube simulation was rather poor (< 0.5%). The efficiency was calculated as the ratio of the number of photons in the PHSP file to the number of incident electrons. The phase space files of the simulation of the X-ray tube (X-ray-PHSP) were also available.

In addition to the MC simulation results, X-ray spectra were obtained from Siemens for the voltages of 80, 105, 110, 115 and 130 kV at the center of the field of view i.e. for minimal filtration from beam shaping filters. Spectra at the edge of FOV (maximal filtration) were provided for the 105, 110 and 115 kV. However there is no documentation on either the accuracy or the method used to generate the provided spectra. The spectra are presented in Figure 29 and Figure 30.

[6] The parameters of the tube angle, voltage settings and pre-filtration were provided by Siemens.

[7] Assuming 100mAs electrons and that a complete rotation is made out of 1000 angle increments (view), 10^{14} electrons are used per view when the CT is operated in clinical conditions.

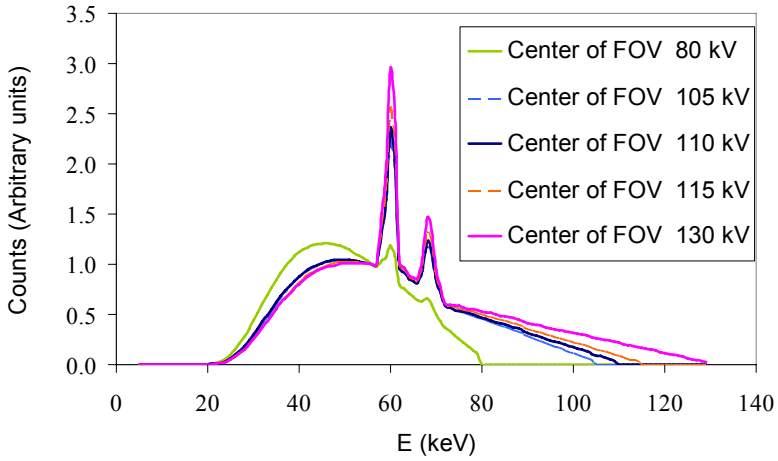

Figure 29. Energy spectra provided by Siemens for the DURA 352-MV X-ray tube at the center of the FOV. Counts were arbitrarily normalized relative to counts at 56 keV (base of the region of K_α characteristic lines of tungsten).

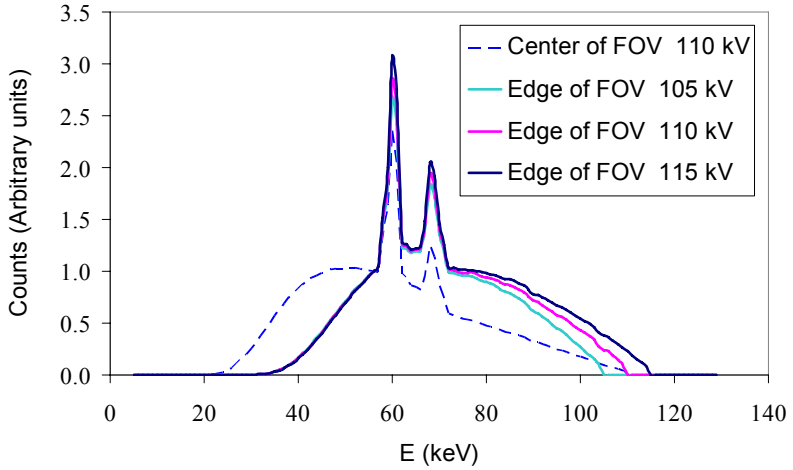

Figure 30. Energy spectra provided by Siemens for the DURA 352-MV X-ray tube at edge of the FOV. The tube settings are 105, 110 and 115 kV. Counts were arbitrarily normalized according to the counts at 56 keV (base of the region of K_α characteristic lines of W). The spectrum of 110 kV photons in the center of the FOV is also shown for comparison.

The energy spectra calculated from the MC simulation of the X-ray tube and the spectra provided by Siemens are compared to energy spectra measured using the Compton spectrometer described in section 3.5.

CT1: Source, filters and collimators

For simulation of the filters and collimators, the X-ray tube was approximated by an isotropic photon source. The approximation was used even despite having a PHSP file of the X-ray tube representing the position and energy of the photons exiting the X-ray tube. This is done to limit the dependence of the final results on the position of the photons in the PHSP file representing the X-ray source. Another reason is to save calculation time. The efficiency of the X-ray tube simulation was very poor (< 0.5%) and the total number of photons in the PHSP of the X-ray tube simulation was very small. It was considerably smaller than the number required for further simulation (10^{10}). Had the PHSP file been used, it should have been recycled for > 100 times. Reading the entries of the PHSP file and tracing each particle (photons and electrons)

requires more time than assuming that the photons are created at a single point in space with a given energy.

The X-ray tube was simulated as a collimated point source with rectangular beam section. It was set 3.4 cm from the compound module simulating the filter. The size of collimator aperture was chosen to provide a field size of 50 cm diameter in the centre of the CT. The MC simulated spectra with different maximum energy were used as input spectra of the point source. A comparison between the point source approximation and the MC simulation of the X-ray tube is presented in section 0.

Our specific CT machine has a bow-tie filter from Aluminium, followed by Teflon filter. The filters were simulated using the compound model "pyramids". Each filter was simulated in layers to correctly model the design. 19 layers were used to model the Al filter while 13 layers were used to model the Teflon filter. Unfortunately, the compound module "pyramid" is defined with a 0.1mm air-gap separating the different layers to allow correct allocation of electrons at the boundaries of the layers. However, the presence of air-gaps distorts the spatial distribution of the filters which influences the beam profile. To reduce the effect of the air gaps, the layers of the CM were set such that the thickness of air-gap is 10% the thickness of the layers. The density of both Al and Teflon was assumed 110% the real density to compensate for the air-gaps and model the density distribution of the filters. The simulated geometry of the filters is shown in Figure 31.

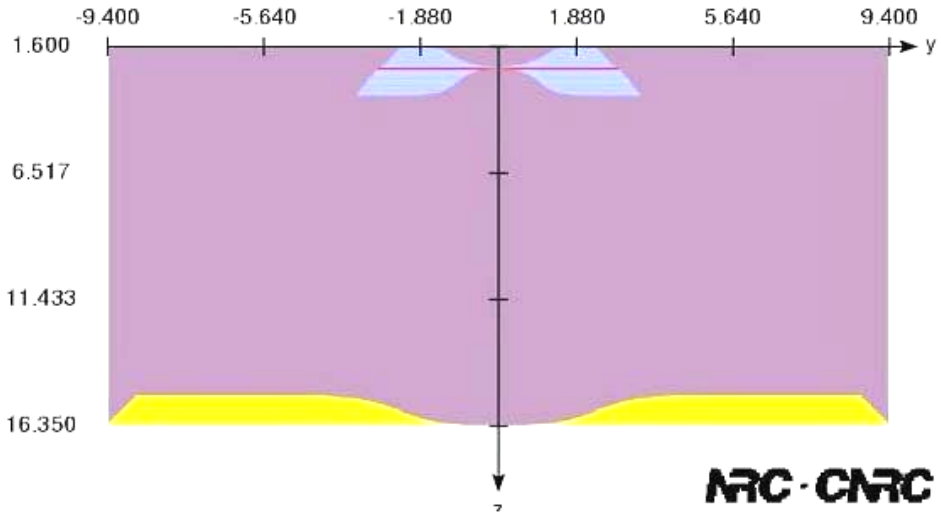

Figure 31. The simulated geometry of the Al filter (blue) and Teflon filter (Yellow). The beam axis is the vertical axis. Horizontal axis is the axis along the slice. Both dimensions are in centimetre units.

The last component in the CT1 part of the simulation was a lead collimator. The compound module used to simulate the collimator was a "Block", 14.7 cm from the focal spot. The opening of the collimator was 1cm by 50 cm. The aim of this collimator is to stop all the photons outside the "CT-slice" of interest to shorten the simulation time.

Investigation of various collimator designs showed that use of collimators doesn't affect the spectrum of incident photons if leakage and aperture scatter are taken into consideration in designing the collimator. Choosing an aperture that is slightly larger than needed was sufficient to eliminate scatter due to the collimator. Using high cut-off energies for the collimator body prevented leakage.

Only 1% of the incoming photons were scored at the PHSP. The reason is that the code requires that the field of the incident isotropic source be larger or equal to the entrance face of the first compound module. As a result, a large fraction of the incident beam was not usable and was cut out by the collimators. The phase space file of the CT1 part of simulation (CT1-PHSP) was used as input to CT2 part.

CT2: phantoms and substitutes

The cylindrical phantoms and tissue equivalent substitutes were simulated using the compound module "side tube". Since the simulation code terminates the history of particles outside the defined dimensions of the compound module, it was necessary to simulate a side tube of minimum 3 layers representing the substitute, phantom and air surrounding the phantom in the field of view (50 cm diameter). Otherwise the projections of the phantom would have been truncated.

The input of this part of the simulation was CT1-PHSP. The output was calculated at a scoring plane (94 cm from focal spot) representing the position of the detector arrays. The surrounding medium was defined as air. The detector array and the scatter grid were not simulated. The simulation of 672 detector channels and 673 septa of the grid require unreasonable simulation times. Ideal collimation was assumed and scattered photons were subtracted analytically (see section 3.6.7 below).

Each simulation of the CT2 part was regarded as a "view" i.e. a measurement at a single specified angle which corresponds to a line in the sinogram. To generate more views using the same CT1-PHSP, the seeds of the random number generators were varied for CT2 part of the simulation.

$5x10^8$ incident photons were usually used for the CT2 part of the simulation. If the number of photons in the CT1-PHSP was insufficient, the program automatically recycles the file until the specified number of particles is achieved. As a result, the variance in the CT2-PHSP is underestimated because input photons are correlated. In order to recycle the CT1-PHSP as little as possible, large CT1-PHSP files have been created.

The efficiency of the part CT2 of the simulation was defined as the number of photons in the PHSP file relative to the number of the incident photons. It was about 5%.

The phase space output of the simulation (CT2-PHSP) is originally in binary format. It was converted to ASCII for further analysis using a modified "readphsp" subroutine in the BEAMnrc/EGSnrc package. The conversion was necessary since the MC simulation was run under Linux, however, calculation of projections and reconstruction are available under MS Windows using ASCII files.

3.6.5. Implementation of detector response

It is possible to calculate the energy response of the detectors because the energy of the photons is given for each photon in the PHSP file. According to the energy of the photon, an efficiency factor (weight) is given to each photon. The weight was estimated from the energy response function of the detectors as shown in Figure 32 [29]. The total signal at each detector element was calculated as the sum of weights which were scored in the specified element.

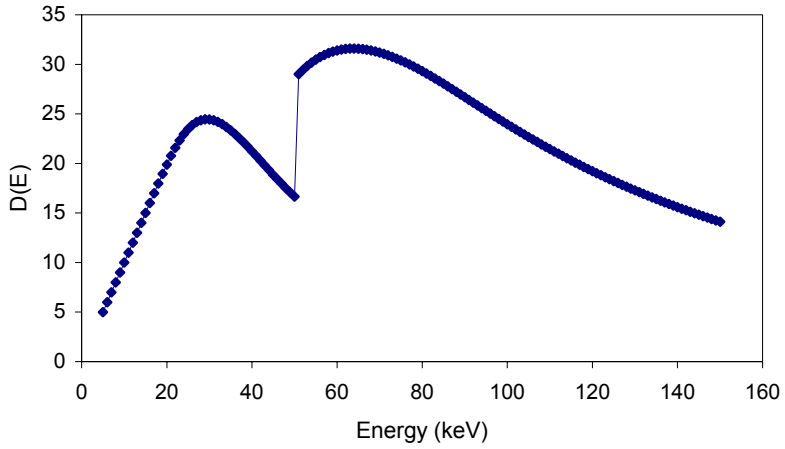

Figure 32. The response function of the detector material of the Siemens Emotion CT scanner.

3.6.6. Sorting photons into detector elements

Particles are initially sorted in the required slice thickness using the information on the position of the photons in the X-direction. Sorting the particles into detector elements along the slice-axis (y-axis of the simulation) required the knowledge of the number of detectors in the array (N) and the length of the active part of the detector.

First, the effective angle of incidence along the Y-axis (β) is calculated for the scored photon (see Figure 33). β is calculated as the arctangent of the y-position relative to the distance to the focal spot (SDD) and can be used to define the detector element in which the photon is scored.

$$\beta = \text{ arc tan (y-position/SDD).} \tag{3.5}$$

Then, the photon is sorted into the detector elements by calculating an effective detector-index (n) based on β . The index (n) refers to the position of the detector element in the arc. It is calculated as:

$$n = Floor(\beta/\alpha), \tag{3.6}$$

where α is the opening angle of each detector element and $\alpha = 2 \times 27°/N$ (see Figure 34) .

The impact angle (θ) is the angle with which the photons hit the scoring plane. It is independent of β which determines where photon hits the scoring plane.

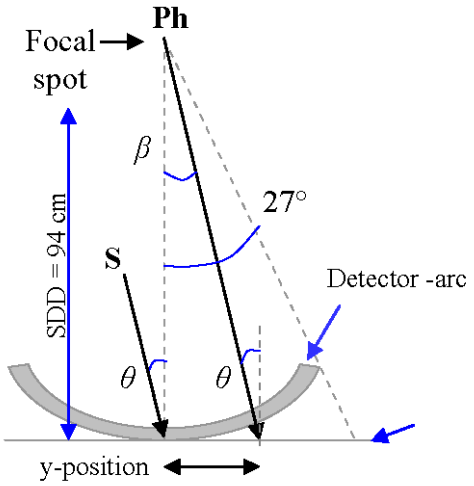

Figure 33. Schematic diagram representing the calculation of the effective angle of incidence (β) as a function of the y-position in the scoring plane for the photon Ph. The impact angle (θ) is also indicated. It is independent of β . For example, θ is the same for the photon (Ph) and the scattered photon (S) whereas β for S is zero.

3.6.7. Scatter corrections

In a real CT scanner, particles which hit the active area of the detectors without hitting the scattering grid are considered "true events" (see Figure 34).The same was assumed in the simulation.

Photons can be distinguished by assuming ideal collimation. It is possible to exclude all scattered photons knowing the dimensions of the scatter-grid, the length of the active and dark areas of the detector (δ_{active} and δ_{dark}) and the incidence angle of each photon in the scoring plane (θ). The schematic diagram in Figure 34 illustrates the concept of scatter corrections.

Knowing that there are no detectors in the center of the detector arc (i.e. at y=0), the opening angle of each detector (α) was divided into 3 zones : ½ dark, active and another ½ dark. The angle defining the active part of the detector (δ_{active})equals:

$$\delta_{acttive} = \alpha - \delta_{dark} \qquad (3.7)$$

The value of δ_{dark} was calculated as the arctangent of the length of the dark area relative to the distance to the focal spot (SDD) as:

$$\delta_{dark} = \text{arc tan}(l_{dark}/\text{SDD}). \qquad (3.8)$$

The detector element in which the photons are scored (n) is already known from equation (3.6). By knowing δ_{dark} , δ_{active} and n , it is possible to determine the start and end y-positions of each active/dark part of each of the detectors in the scoring plane (flat) without losing information on the arc-geometry of the detector array.

A photon is registered as an event in the active part of the detector if:

$$\left[n \cdot \alpha - \frac{\delta_{dark}}{2} \right] \leq \beta \leq \left[(n+1) \cdot \alpha + \frac{\delta_{dark}}{2} \right]. \tag{3.9}$$

Knowing the length of the septa of the detector elements (SL), the opening angle of the septa (φ) is calculated as:

$$\varphi = \arctan\left(\frac{l_{dark} + l_{active}}{\mathrm{SL}} \right). \tag{3.10}$$

The photon is not hitting the septa if

$$\begin{aligned} &\tan(n \cdot \alpha) \leq \tan(\beta) \leq \tan((n+1) \cdot \alpha) \text{ and} \\ &\theta < |\varphi/2|, \end{aligned} \tag{3.11}$$

Here, θ is the impact angle of the photon (angle with which the photon hits the scoring plane).

Photons arriving at the active area of the detectors (see equation (3.9)) without hitting the septa of the collimators (see equation (3.10)) were recorded as "true events". Trajectories 1 and 2 in Figure 34 show the limits of the accepted true events. Events that hit either the dark area of the detector (S1 in Figure 34) or the collimator septa (S2 in Figure 34) were considered scatter events.

θ can also be used to distinguish if the photons suffered multiple scattering (scatter-1 pattern) from photons which did not suffer any scattering along their beam path from the source to the active part of the detector (scatter-2 pattern). The photons are registered as scatter free events, if both equations (3.11) and (3.12) are fulfilled.

$$\theta < |\delta_{active}/2|. \tag{3.12}$$

3.6.8. Beam hardening corrections (BHC)

Beam hardening is the shift of the X-ray spectrum to higher effective energies as the beam transverses matter. It is an artefact which can not be avoided in CT imaging. It happens because low energy photons are more likely to be absorbed than high energy ones. As a result, the effective energy of the spectrum increases (hardens) with increasing path. The circular arrangement of sources and detectors in CT scanners leads to an increase of energy towards the center of FOV. As the effective energy increases, the absorption probability decreases and attenuation coefficients are underestimated. This leads to an underestimation of CT-numbers in the center of the image. The decrease of CT-numbers in the center of the FOV is called the cupping effect.

Beam hardening artefacts can be corrected if the energy spectrum of the incident photons is known. To illustrate this, let the attenuation coefficient $\mu(s,E)$ be composed of two functions ($f(s)$ and $\psi(E)$) such that:

$$\mu(s,E) = f(s) \cdot \psi(E) \tag{3.13}$$

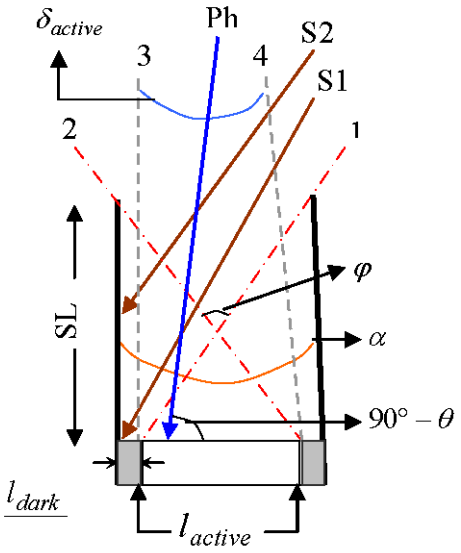

Figure 34. Schematic diagram of a single detector element in the detector arc. The diagram also shows the length of the active and dark areas of the detector (l_{active} and l_{dark}), the length of the septa (SL), the impact angle(θ), the opening angle of the septa (φ) and the opening angle for the detector element (α). Photons (Ph) hitting the active area of the detectors element are considered true events (opening angle is limited by trajectories 1 and 2). Events that have an impact angle (θ) which is less than δ_{active} are considered scatter free photons. The dashed grey lines (3 and 4) represent the limits of the trajectories defining such photons. Events that hit either the dark area of the detector (S1) or the collimator septa (S2) were considered lost and were not registered in the specific detector.

From equation (2.20) and (2.21), the projections ($p(s,E)$) can then be written as:

$$p(s,E) = -\ln\left[\int \Omega(E)\cdot D(E)\cdot e^{-\int \mu(s,E)\cdot ds}\, dE\right] - \ln[I_0] \qquad (3.14)$$

For a normalized spectrum and detector response functions:

$$-\ln[I_0] = -\ln\left[\int \Omega(E)\cdot D(E)\, dE\right] = 0. \qquad (3.15)$$

Using equation (3.13), (3.14) can be written as:

$$p(s,E) = -\ln\left[\int \Omega(E)\cdot D(E)\cdot e^{-\psi(E)\int f(s)\cdot ds}\, dE\right] \qquad (3.16)$$

Assuming that $q(s)$ represent the energy independent projections, then

$$q(s) = \int f(s)\cdot ds\,, \qquad (3.17)$$

The

$$p(s,E) = -\ln\left[\int \Omega(E)\cdot D(E)\cdot e^{-\psi(E)\cdot q(s)}\, dE\right]. \qquad (3.18)$$

Equation (3.18)(3.17) can be inverted to calculate q from the polychromatic projections (p). See Kachelriess and Kalender [61] and Kachelriess et al. [62] for more details.
BHC is a post-processing correction. It is applied at the level of the raw data before reconstruction is performed since equation (3.18) implies that $p(s,E)$ should already be in the form of projections to correctly calculate q as $q(p)$.

The implementation code for BHC was provided by the image reconstruction group of the medical physics department of the Institute of Medical Physics in the Friedrich-Alexander-University Erlangen-Nürnberg, Germany. The code was used with permission of developers for our specific calculations.

The input parameters of the code were the p, $\psi(E)$, $\Omega(E)$ and $D(E)$. In this work, $\psi(E)$ was set to equal the attenuation coefficient of water as a function of energy relative to the coefficient at 40 kV which is the effective energy of the corrections.

$$\psi(E) = \mu^{water}(E) \Big/ \mu_{40kV}^{water} \tag{3.19}$$

Only water based BHC were applied in the scope of this work. The BHC algorithm corrects the effect of beam hardening on the bases that all media interact with the spectrum similar to water. This is a simplification to the problem but a good approximation to most tissue types. If it is possible to distinguish between water-like media and tissue-like media at the level of projections, it is possible to apply a weighted BHC which can correct for bone as well as soft tissues. Weighted BHC has been successfully applied by Kachelriess and Kalender [61].

3.6.9. Presenting projections in log format

The number of photons in the CT2-PHSP file is around 10^7. The analysis of the PHSP file is performed photon by photon. The photons are neither arranged according to energy nor position because photons are scored in the PHSP as soon as their history is terminated (energy below PCUT). Therefore, the calculation of the signal of the detectors is very slow and time consuming.

Once a photon is sorted into its associated detector element (see 3.6.6), the photon is given a new weight factor based on its energy (see 3.6.5). The weight factors are summed separately for each detector element in the array and the result is then stored as list of detector indices (n) and the corresponding signal ($I(n)$).

To calculate projection data ($-\ln(I/I_0)$), one needs to calculate the initial intensity of the incident photons (I_0). A dedicated simulation is set with only air in the FOV to calculate I_0. $I_0(n)$ is calculated in the same manner as any other file. Once $I_0(n)$ is obtained, $-\ln(I(n)/I_0(n))$ is calculated for each detector index (n). The initial intensity ($I_0(n)$) was calculated, each time a different CT1-PHSP file was used.

3.6.10. Reconstruction

Now the photons are sorted into projections, a simple fan-beam Filtered Back Projection reconstruction algorithm (FBP) is applied to obtain images. The reconstruction algorithm includes:

- Rebinning into parallel projections
- Convolving with a Ram-Lak kernel
- Back projecting

The reconstruction algorithm was developed by the Image Reconstruction group of the medical physics department of the Institute of Medical Physics in the Friedrich-Alexander-University Erlangen-Nürnberg, Germany[8].

The reconstruction code requires the knowledge of: diameter of FOV, number of views, position of CT at starting angle, fan angle of the X-ray tube and detectors, size of image and number of pixels per image. The main input is the generated projection from section 3.6.9.

The reconstructed image matrix is given in arbitrary values. Though the values represent the distribution of the attenuation coefficients, they are not normalized.

To calculate average attenuation coefficient, a circular region of interest (ROI) is defined in the center of the reconstructed image. The diameter of the ROI was set to 1.8 cm. The attenuation coefficients of the different pixels which are within the ROI are averaged.

3.6.11. Normalization of reconstructed values (Hounsfield units)

Hounsfield units are the attenuation coefficients relative to μ_w (see equation (2.35)). Therefore, it is necessary to know μ_w. To obtain μ_w, a dedicated simulation is performed using a water cylinder in the center of the FOV. The diameter of the water cylinder was always set to 25 cm. The reconstructed value of μ_w (μ_w^{recon}) was calculated by defining a region of interest in the center of the reconstructed image and calculating the average attenuation coefficients from the different pixels which are within the ROI. μ_w^{recon} was used to define the normalization parameters for the other simulations of the same settings of the X-ray tube and filters.

The assumptions for normalization are:

$$HU_{water}\left(\mu_w^{recon}\right)=0\,, \tag{3.20}$$

$$HU_{air}\left(\mu_{air}^{recon}\right)=-1000\,, \tag{3.21}$$

and that the relation between CT-numbers and attenuation coefficients is linear as seen in equation (2.35).

For the other materials whose attenuation coefficient is given by the reconstruction algorithm (μ_m^{recon}), CT numbers were calculated using:

$$\text{CT}-\text{number}=1000\times\left(\frac{\mu_m^{recon}}{\mu_w^{recon}}-1\right)HU\,. \tag{3.22}$$

The condition for water in equation (3.20) is immediately satisfied. The condition for air is satisfied because the projections have been written as $(-\ln(I(n)/I_0(n)))$ which is zero for air, As a result, $\mu_{air}^{recon}=0$ and the normalized CT-number of air is -1000.

[8] The code was used with permission of developers for our specific calculations.

3.7. Simulated effects

The MC simulation of the CT- scanner (see 3.6) was used to study the effects of the material of the substitutes (Gammex and H-materials see 3.2), the filters, the voltage settings of the X-ray tube, the size of the PMMA phantom and finally the material of the phantom. This was achieved by varying the studied parameter while keeping all the other parameters the same as in the standard simulation.

The standard simulation for CT1 is a simulation of the two filters (Al and Teflon) for an input spectrum of 110 kV which was generated by earlier simulations of the X-ray tube. The incident number of photons is 10^{10}.The standard simulation for CT2 is a simulation of phantom of 16 cm diameter which is made out of PMMA. The phantom inserts are Gammex substitutes of 2.8 cm diameter. The simulations were performed for a selection of Gammex substitutes including: Brain, CB, CB2 30%, CB2 50%, CB, IB, Fat, Muscle, LN300 and LN450.The input file is CT1-PHSP from the standard simulation above.

The incident number of photons is $5x10^8$. One view is usually used to perform the reconstruction. A summary of the simulated effects and the parameters used to generate them are listed in Table 3.

When more than one view is needed, the seeds for the random number generator were changed in CT2-part of the simulation but sill using the same CT1-PHSP file as input.

3.7.1. Filters

The Emotion CT has 2 filters: an Aluminium bow-tie filter and a Teflon filter. In this study, 4 independent simulations of the CT1 part were performed to investigate the effects of the filters. The simulations describe the cases when:

- There are no filters in the beam path,
- There is only one filter of Aluminium in the beam path,
- There is only one filter of Teflon in the beam path,
- Both Aluminium and Teflon are in the beam path.

Besides removing one or both filters, no modifications to the shape of the filters were done. The input to the simulation is the photon spectrum corresponding to 110 kV which was generated by MC simulation of the X-ray tube. The number of incident photons was 10^9 which was is not sufficient to reconstruct CT-images with reasonable quality.

The simulated CT1-PHSP files were analyzed using “Beamdp”. The spectral distribution in-center and off-axis of the FOV were calculated. Also the average energy and the energy fluence in the FOV were calculated.

3.7.2. Phantom inserts (Gammex substitutes and H-substitutes)

The standard CT1-PHSP (10^{10} incident photons for a 120 kV energy spectra) was used. In CT2 part of the simulation, the phantom was assumed to be made of PMMA with a 16 cm diameter. The number of incident photons was $5x10^8$. Five views were used to reconstruct the images.

Table 3. Summary of CT-simulations performed in this work and the parameters used to carry out the different studies. The parameters indicated for CT1 part are: the number of incident photons and the peak voltage of the phantom spectrum in CT1. The arrangement of the filters is also noted. For the CT2, the indicated parameters are: the number of incident photons, the number of independent views, the type of phantom material, the diameter of the phantom, the type of insert. Corrections as scatter and BHC are also indicated. The quantities analyzed in the study (spectral distribution, mean energy or CT-numbers) are mentioned.

CT1	Filters	Phantom inserts	kV	Diameter of phantom	Phantom materials
Incident # photons	10^9	10^{10}	10^{10}	10^{10}	10^{10}
Peak voltage (kV)	110	120	80, 100, 105, 110, 115, 120 and 130	110	110
filters	Al, Te, Al & Te, none	Al & Te	Al & Te	Al & Te	Al & Te
CT2					
Incident # photons	--	$5x10^8$	$5x10^8$	$5x10^8$, $3x10^9$ for 28 and 32 cm diameter	$5x10^8$
independent views	--	5	5 for 80, 110, 120 and 130 kV. 1 for 100. 105. 115 kV	1	5
Phantom material	--	PMMA	PMMA	PMMA	PMMA, water, air, RW3, muscle, CB
Phantom diameter (cm)	--	16	16	12, 16, 20, 24, 28 and 32	16
Insert	Gammex subs	Gammex subs & H-materials	Gammex subs	Gammex subs	Gammex subs & water
Scatter cor.	Yes	yes	yes	yes	yes
BHC	No	no	no	yes	Yes
Analyzed quantities	Spectra Energy fluence Average energy	Spectra Average energy CT-numbers	Spectra Average energy CT-numbers	CT-numbers	CT-numbers

The inserts of the phantom were Gammex substitutes and H-materials. H-materials (see section 3.2) were experimentally investigated by Jäkel et al. [6]. Their composition was simulated from the above reference. The substitutes investigated were: H-800, H-500, H+200, H+400, H+900 and H+1200.

The simulated CT2-PHSP files were analyzed using "Beamdp". The spectral distribution and energy fluence for the 110 kV incident photons were analyzed when Gammex substitutes are used as phantom inserts. The CT-numbers for the Gammex substitutes and H-materials were calculated for the voltage settings of 120 kV.

3.7.3. Voltage settings of X-ray tube

Spectral distributions which were calculated by simulating the X-ray tube were used as input to CT1. The spectral distributions were calculated using 7 peak energies (80 kV, 100 kV, 105 kV, 110 kV, 115 kV, 120 kV and 130 kV).

The incident number of photons in CT1 was 10^{10} for the voltage settings above. The CT1-part of the simulation was performed using both Aluminium and Teflon filters. The number of incident photons in the CT-part was $5x10^8$. The simulated phantom was 16 cm diameter out of PMMA. The simulated inserts were Gammex substitutes. Scatter corrections were applied but not BHC. 5 independent views were simulated for the kV settings of 80, 110, 120 and 130, to ensure low statistical noise of the simulated projections and the reconstructed CT-numbers. Only 1 view was simulated for the voltage settings of 100, 105, 115 kV, since these simulations were only used to estimate the effect of 5 and 10 kV changes in the voltage.

The simulated CT2-PHSP files were analyzed using "Beamdp". The spectral distribution and energy fluence were calculated for three initial spectra (80, 110 and 130 kV) when PMMA phantom and cortical bone insert are in the center of the FOV. The CT-numbers for the Gammex substitutes were calculated for all voltage settings.

3.7.4. Diameter of PMMA phantom

The PMMA phantom was simulated with varying diameters to study the effect of phantom size on CT-numbers of the substitutes inside the phantom. The standard phantom diameter is 16 cm.

10^{10} incident particles and a 110 kV energy spectrum was used in the CT1 simulation. In CT2 part of the simulation, the diameter of the phantom was varied from 12 to 32 cm in steps of 4 cm steps. The number of incident photons was $5x10^8$. Beam hardening corrections were applied to the simulated polychromatic projections. A single view was used to reconstruct the images after applying beam hardening corrections.

Unfortunately, the simulations of the 28 and 32 cm diameter with only $5x10^8$ incident photons resulted very noisy projections. The reconstructed images of which had lots of ring artefacts and the calculated CT-numbers had very large uncertainties. Therefore, the above simulations (28 and 32 cm diameter) were carried out using $3x10^9$ incident photons. The noise in the projections and the uncertainty of the calculated CT-numbers were considerably reduced. However, the higher number of incident photons came at the cost of recycling the CT1-PHSP 26 times instead of the usual 4 times when $5x10^8$ photons are used.

3.7.5. Material of phantom

The material of the standard phantom is PMMA. In this study, the phantom was simulated with different material to study the effect of phantom material on CT-numbers of the substitutes inside the phantom. The materials investigated were air, water, muscle substitute from Gammex, cortical bone substitute from Gammex, RW3 water equivalent material from PTW and finally PMMA.

The standard CT1-PHSP (10^{10} photons with a 110 kV energy spectrum) was again used. In CT2 part of the simulation, the material of the 16 cm diameter phantom was varied. The simulation was carried out for Gammex substitutes and water as phantom inserts. The number of incident photons was $5x10^8$. Five independent views were simulated. BHC were applied to each view which were reconstructed into a CT-image.

3.8. CT calibration relations for ion therapy

The treatment planning program (TRiP) calculates the penetration depth of the ions using a Hounsfield Look-Up Table (HLUT) which is based on CT –calibration. In this work, an empirical calibration was used to study the effects of CT-uncertainty on Carbon ion dose calculations. To build an empirical calibration relation, a piecewise linear fit (representing the relative range as a function of CT-numbers) is performed. The relative range data were measured values as seen in 3.4. The CT-numbers were simulated values as in 3.7. The piecewise fit was performed using the fit-package of Sigma Plot 8.0.

Several CT-calibration relations are calculated. The calibrations are based on CT-simulations of different voltage settings, different phantom size and different phantom materials and substitute materials, to study the effect of the different CT-parameters on the relations. In total, 8 calibration relations are calculated.

The simulations for the standard phantom settings were set as the base of the comparison. The standard setting is given by a 110 kV photon beam which is incident on a 16 cm phantom of PMMA with Gammex inserts.

To study the effect of voltage shifts, a ±10 kV increment was assumed. The CT-numbers of each substitute (i) at the voltages 100 (HU_i^{100}) and 120 kV (HU_i^{120}) were calculated from the simulated 110 kV using the relation between CT-numbers and voltage difference (ΔU) such that:

$$HU_i^{100+\Delta U} = HU_i^{110} + \left(\frac{\Delta HU}{\Delta U}\right)_i \times (\Delta U), \tag{3.23}$$

The value of $(\Delta HU/\Delta U)_i$ was calculated for each substitute (i) from the interpolation of simulated data for 80, 100, 105, 110, 115, 120 and 130 kV.

Similarly, the CT-numbers of Gammex substitutes in a PMMA phantom of 30 cm diameter (HU_i^{30cm}) were calculated from the values in a 16 cm phantom (HU_i^{16cm}) and 110 kV as:

$$HU_i^{30cm} = HU_i^{16cm} + \left(\frac{\Delta HU}{\Delta diameter}\right)_i \times (14cm). \tag{3.24}$$

Here, the value of $(\Delta HU/\Delta diameter)_i$ was calculated for each substitute (i) from the interpolation of simulated data for 12-32 cm diameter phantoms of PMMA with steps of 4 cm.

From the simulation of different phantom materials, the results of the simulations of substitutes in air were used to build a calibration relation. The CT-numbers of the H-materials were also used to build a calibration relation.

Finally, two worst case scenarios for the soft-tissue region (-100 – 120 HU) were assumed. The range of HU defining the soft tissue region was estimated from CT-histograms ([14] and Figure 82). Tissues with CT-numbers between -100 HU and 120 HU represent more than 70 % of the volume of the patient. Worst case scenarios were set by assigning extreme relative ranges to the CT-numbers in the soft tissue region. In the first case, all the tissues in the defined region were assigned the relative range of fat. In the second case, all the soft tissues were assigned the

relative range of low density bone. The remaining regions (less than -100 HU and more than 120 HU) were treated the same as the standard calibration for 16 cm phantom of PMMA with Gammex substitutes and 110 kV photon beam.

The parameters defining the calibrations are listed in Table 4.

Table 4. List of parameters defining calibrations which were calculated based on simulated CT-numbers

	Phantom diameter(cm)	Phantom material	kV	Inserts	Soft tissue region
1	16	PMMA	110	Gammex substitutes	Piece-wise fit
2	16	PMMA	100	Gammex substitutes	Piece-wise fit
3	16	PMMA	120	Gammex substitutes	Piece-wise fit
4	30	PMMA	110	Gammex substitutes	Piece-wise fit
5	16	PMMA	120	H-materials	Piece-wise fit
6	16	Air	110	Gammex substitutes	Piece-wise fit
7	16	PMMA	110	Gammex substitutes	Lower limit
8	16	PMMA	110	Gammex substitutes	Upper limit

3.9. Translation of CT-calibrations to range uncertainties

To study the effect of the calibrations on the relative range, CT data from one patient treated with Carbon ion at the GSI was used. The reference number to the selected patient is CCN283. The selected patient suffered from chondrosarcoma at the base of the skull. Total volume of the tumour was 105 ml. The critical organs were the brainstem the chiasm and the left optical nerve. The CT images were taken for the head and neck part of the body. Figure 35 is a slice though the tumour. It shows the clinical target volume (CTV, in red) and the critical organs around it.

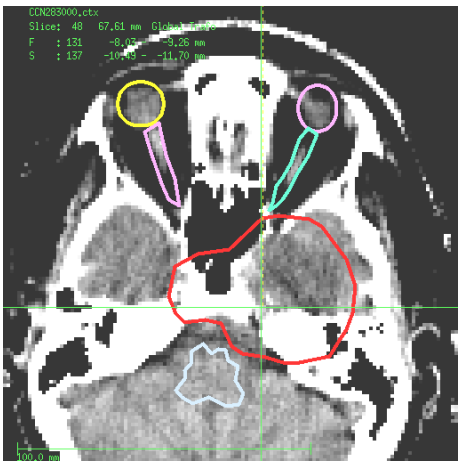

Figure 35. Transverse slice of the CT-data of patient CCN283. The tumour (CTV) is marked in red; the organs at risk are the brain stem which is marked in blue, the left optical nerve which is marked in green, the chiasm (not shown in this slice), the eyeballs and the other optical nerve.

The CT-numbers along a line through a central image (slice 48) were calculated. The line through the CT-image was defined by the pixel coordinates of y=131. X was 1-256. The profile is shown in Figure 36. The tumour is between pixels 110 and 160.

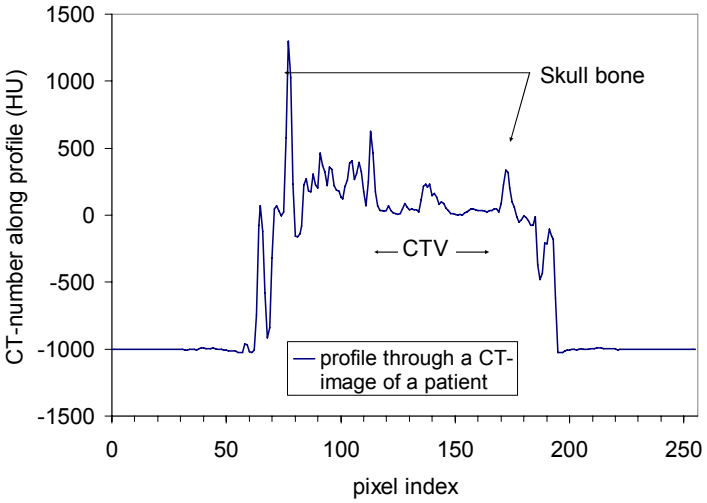

Figure 36. Profile through a CT-image of a patient. The profile is through the y=131, x 1-256 (slice number 48). The arrows indicate the position of skull bone. In between is a mixture of soft tissue and spongy bone (lower skull base).

The tumour is located towards the left side of the body; it could be treated using a single field coming from the left. A better dose distribution can be achieved using a two-field treatment. Each field is optimized to deliver a homogeneous SOBP. The relative range for each pixel is calculated based on the CT-number of the pixel and the given calibration relation. The accumulated range along the beam path is calculated by adding up the contributions from each pixel in the beam path.

The WEPL of each pixel is calculated as the relative range of the pixel times the length of the pixel. The patient is scanned using a 287 mm diameter FOV and the image is represented by a 256x256 pixel matrix. Therefore, the length of the pixels is equal to $\frac{287mm}{256} \cong 1.12mm$.

It is possible to calculate the shift in the distal end of a SOBP in terms of WEPL by assuming a single field irradiation where the field is coming from the left. The distal edge of the spread out Bragg peak is set at pixel 110 for the optimized field (i.e. energy and intensity of the single Bragg-peaks forming the SOBP has been calculated based on the standard calibration). The shift in the position of the distal end ($\Delta WEPL$) is then calculated by:

$$\Delta WEPL = WEPL_{cal(i)} - WEPL_{\text{standard}}, \qquad (3.25)$$

where $WEPL_{cal(i)}$ is the WEPL which is calculated using the calibration (i) and $WEPL_{\text{standard}}$ is the WEPL calculated using the standard calibration curve.

3.10. Translation of different CT calibrations to dose uncertainties

Treatment planning for Carbon ions is performed using the treatment planning software "TRiP". The ions are delivered in fields. It is necessary to first optimize the field then the dose can be calculated using the information of the optimized field. However, the code also needs to know where the tumour is in depth; therefore, it also needs to have a HLUT already.

In order to estimate the effect of the range uncertainties on the resulting overall dose distribution, each of the relations in Table 4 was fed into TRiP as a HLUT. In this work, the optimization of the fields was performed using one calibration relation (cal 1, Table 4). The dose was calculated based on the beam settings of the optimized field. The dose calculation was first done using the calibration relations cal 1 in Table 4. The calibration relation was then varied and dose calculation was redone using the other calibration relations in Table 4 for the same optimized field.

The analysis was performed for the patient with reference number CCN283. A transverse slice of the CT-data of the patient, showing the location of the tumour and neighbouring critical organs, is shown in Figure 35. Two beam arrangements were optimized: a single-field plan and a two-field plan[9]. The single-field plan uses one field which is characterized by a couch angle of -65°. The two-field plan uses the field with a couch angle of -65° and another with a couch angle of 90°; each of the fields in the two-field plan was assigned 50% of the prescribed dose. The field arrangements with respect to the patient (face up) are shown in Figure 37. Each of the fields was optimized separately. The dose distribution of the two-field plan is the sum of the contributions of both fields.

An ideal plan would be if 100% of the target volume receives 100% dose with no dose in the critical organs. A more realistic criterion for target coverage is when the target volume is covered by the 90% isodose lines and that the average dose in the target volume (D_{mean}) is close to 100%. As for the organs at risk, the average dose delivered to the total volume of the organ (D_{mean}) should be kept as low as possible. It is also important to avoid high dose localisation in parts of the organs at risk because this might also lead to radiation damage. For this purpose, it is important to limit the percent of the organ volume which is inside the 90% isodose line (V_{90}).

The D_{mean} and V_{90} were calculated for the target volume (CTV) and the organs at risk (brainstem, chiasm and the left optical nerve) using the two plans (single and two-field plan) and the eight calibrations in Table 4 for the tumour geometry shown in Figure 35. In total 16 dose plans are compared.

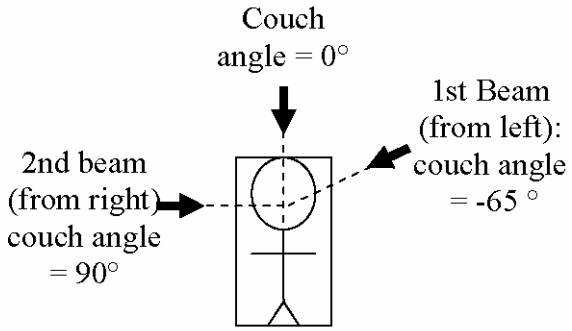

Figure 37. Schematic diagram showing the direction of the incoming beams used for dose calculation. The first beam comes in from the left side with an angle of -65°. The second beam comes from the right for a couch angle of 90°.

[9] Treatment at the GSI is performed using a fixed horizontal beam. The direction of the beam is defined by the angle of the patient's couch.

4. RESULTS

4.1. Experimental investigation of the effects of scanner settings on CT-numbers

The dependence of CT-numbers of Gammex substitutes on the settings of the scanner including: effects of reconstruction kernels, voltage settings, different vendors, slice thickness and FOV are presented here. .

The results presented in Figure 38, Figure 39, Figure 40 and Figure 41 are the difference between the measured CT-numbers at the specified settings and the CT-numbers measured using the head protocol of the Siemens Sensation 4 CT, which is the default protocol for treatment planning for Carbon therapy (protocol number 4 in Appendix A). The deviation between the different measured values (SD) is shown for each data set.

4.1.1. Reconstruction kernels

The effect of reconstruction kernels on CT-values varied for different CT vendors. For the Siemens Scanners, using the H40s reconstruction kernel produces higher CT-numbers for bone substitutes and lower CT-numbers for lung and fat substitutes than using other reconstruction kernels (B40s, B60s, B70s and H60s). The deviation in the CT-number of cortical bone is about 50 HU (Figure 38). For the Toshiba Aquilion16 scanner, FC69 reconstruction kernel produces lower CT-numbers than the FC10 and FC48 kernels. As for the Philips scanner, CT-numbers resulting from using the EC kernel are higher than those using the D kernel which is in turn higher that the C kernel (Figure 39) .

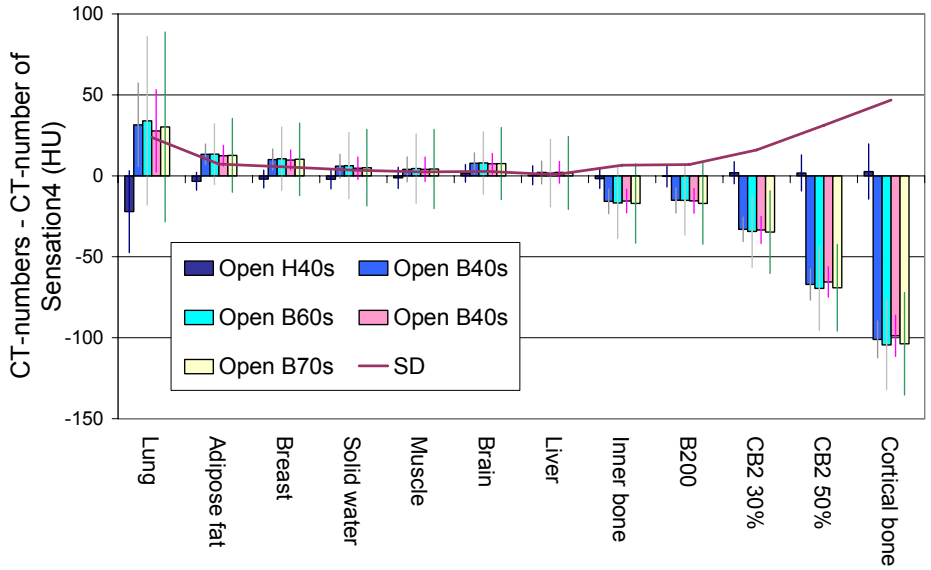

Figure 38: Change of CT-number with reconstruction kernel of the Siemens Open CT scanner. In the legends, H40s, B40s, B60s and B70s are reconstruction kernel specifications of the manufacturer.

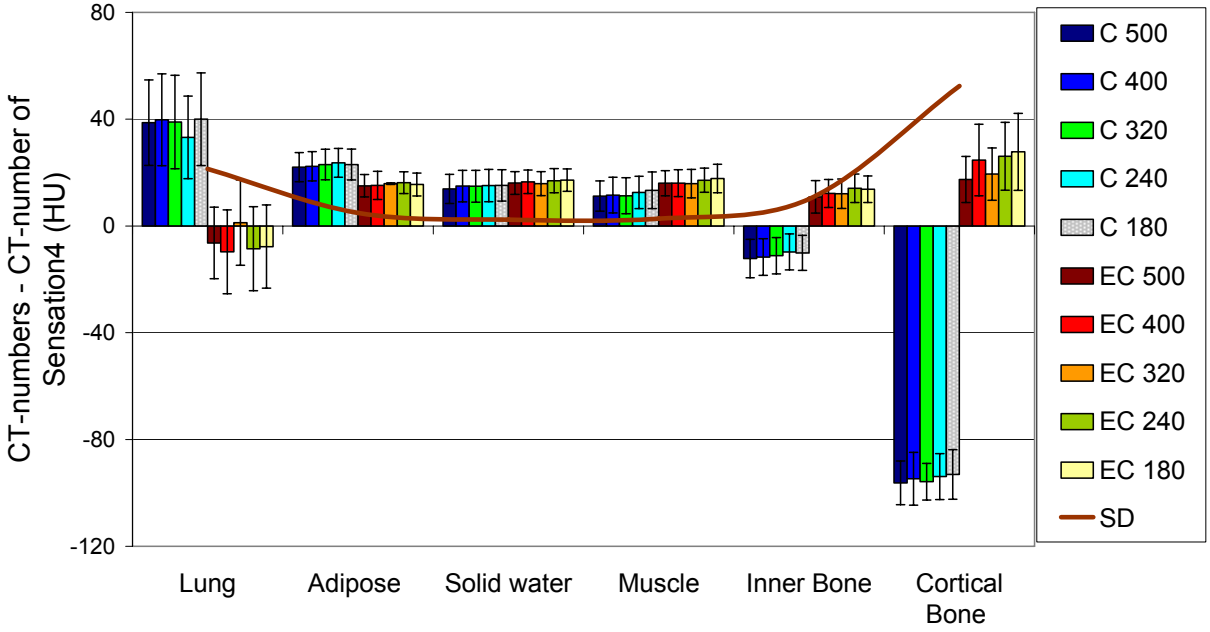

Figure 39. Change of CT-numbers with FOV diameter and reconstruction kernel of the Philips CT. In the legend, C and EC refer to the reconstruction kernel and numbers 180-500 refer to the diameter of the FOV in mm.

4.1.2. KV settings

The effect of voltage setting of X-ray tube was investigated for the Siemens Emotion scanner. The CT-values increase with decreasing voltage settings of the X-ray tube. CT-values of bone like materials are strongly affected by the change of energy. The changes of kV by 50 kV lead to 270 HU deviations in CT-number of the cortical bone. The CT-values of soft tissues are not affected.

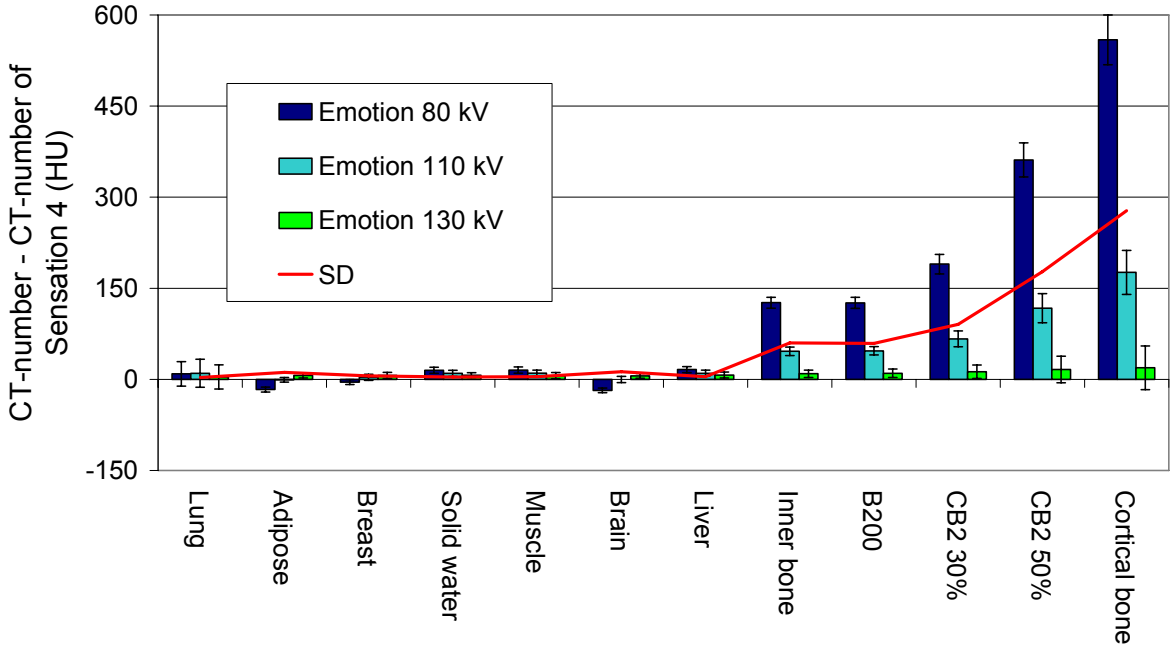

Figure 40. Change of CT-numbers with kilovolt settings of the X-ray tube of the Emotion CT scanner.

4.1.3. Different vendors

In Figure 41, the CT-numbers resulting from scanning Gammex substitutes with the head scanning protocol as specified by each vendor is presented. The protocol is taken as specified by manufacturer. The standard deviation between the different measurements increases with increasing electron density of the measured substitute. It reaches 75 HU for cortical bone substitute. The deviations are well within the measured uncertainties for lung, fat and soft tissue substitutes.

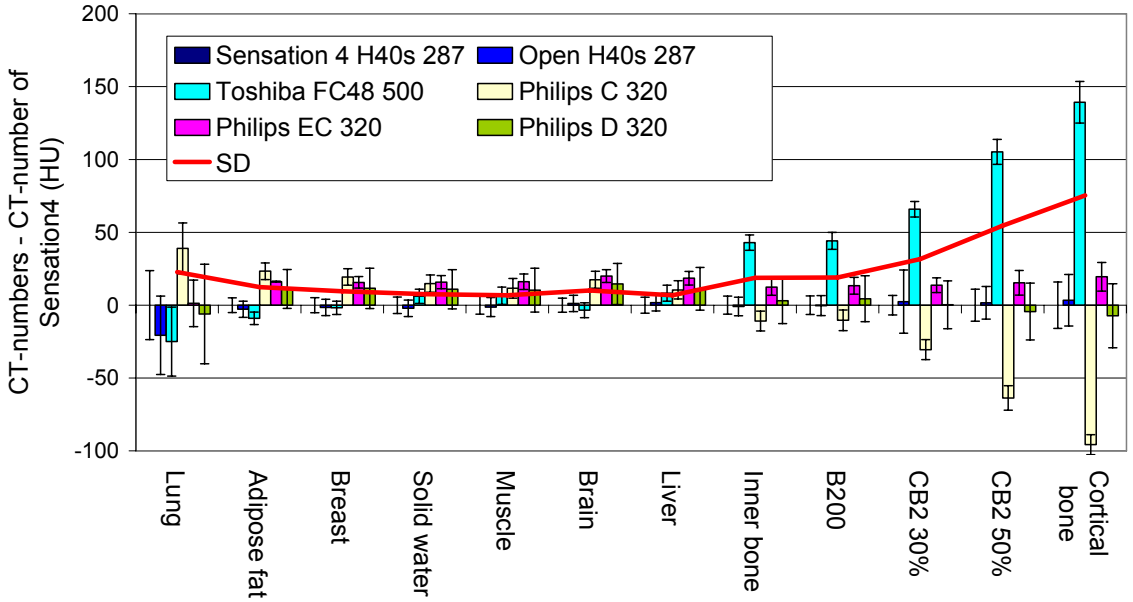

Figure 41. CT-number of Gammex substitutes using the head protocol of different CT vendors. The standard deviation between the different measurements for each substitute type is indicated in the graph as "SD". The uncertainty of each measurement point is represented in the error bars. The legends indicate the scanner name (Sensation4, Open, Philips and Toshiba) the reconstruction kernel used (H40s, C, D, EC and FC48) and the diameter of the FOV in mm (287 for Siemens scanners, 500 for Toshiba and 320 for Phillips) .

4.1.4. Slice thickness

As expected, there is no visible deviation in CT- numbers due to changes in slice thickness using the homogeneous substitutes. Two independent measurements of the CT-numbers in Gammex substitutes were performed; the slice thickness was 1 and 5 cm. The substitutes were scanned once using protocol 7 in Table 15 and another using protocol 8. CT-numbers were calculated separately from the two measurements. The CT-numbers of the both measurements agree to within 1 HU maximum (see 7 and 8 in Table 16 in Appendix A).

4.1.5. FOV

There is no reason to assume change in measured CT-numbers due to changing the size of the FOV, unless the dimensions of the FOV are smaller than the scanned object. The problem, then, is truncated projections.

All the measurements which were compared to study the effect of the scanning FOV have been performed with a FOV diameter that was bigger than the diameter of the phantom (16 cm). The measurements performed at the two scanners where the option of changing the dimensions of the scanning FOV is possible i.e. The Philips MX8000 and the Toshiba Aquilion16 scanner.

Measurements at the Philips scanner where performed using 5 diameters of the FOV (180-500 mm). Figure 39 clearly shows that the variation of the CT-numbers is within the uncertainty of the measurements. In fact, more deviation is seen from changing the reconstruction kernel than due to changing the dimensions of the FOV.

Measurements at the Toshiba scanner were performed using 4 different FOV diameters (240, 320, 400 and 500 mm). Deviations in measured CT-number at the Toshiba Aquilion16 scanner were considerably larger: 63 HU for cortical bone and 22 HU for lung. The reason is that the filtration of the X-ray beam is correlated with the diameter of the FOV at the Toshiba Aquilion16 scanner. As a result, changing the FOV corresponds to a different energy of the incident photons which will cause deviations in the measured CT-numbers.

4.2. Gammex substitutes vs. H-materials

CT- numbers and relative range were measured in Gammex substitutes. The data on CT-numbers and relative range of the H-materials were taken from Jäkel et al. [6].

For CT measurements, PMMA phantom (Figure 21) was scanned using the Siemens Sensation 4 and Siemens Open scanners (protocols 4 and 9 in 0). The measurement results are presented in Table 5 for the Gammex substitutes. The difference between the measurements at the Sensation 4 and the Open scanners was negligible. CT-numbers are presented as a function of the electron density of the Gammex and H-materials in Figure 42.

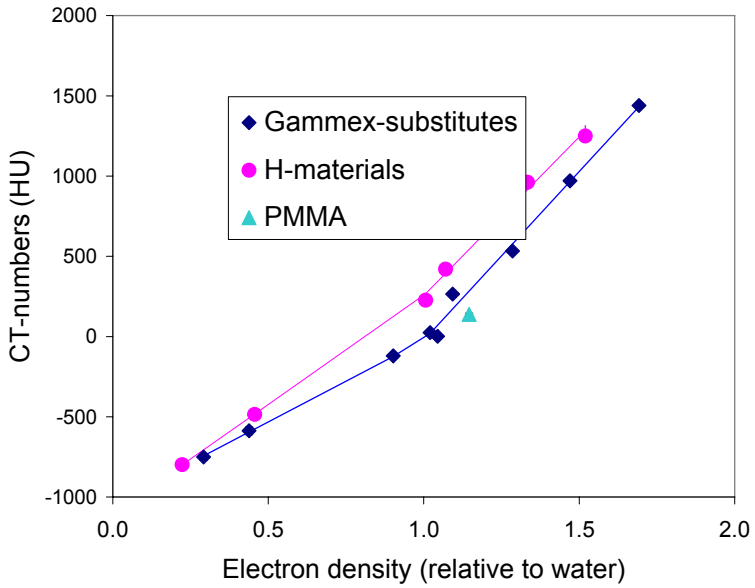

Figure 42. CT numbers as a function of the electron density relative to water for Gammex substitutes, H-materials and PMMA. The uncertainties in CT-measurements are also plotted but they are indistinguishable.

184 MeV/u and 270 MeV/u Carbon beams were used to measure the relative range (WEPL/T) of the Gammex substitutes. The position of the maximum of the Bragg peak in water was used to determine the WEPL. Inhomogeneous substitutes (e.g. LN450[10]) caused more range

[10] The LN450 sample is a substitute for lung. The substitute has a spongy texture with trapped air bubbles which gives it the required low density but also makes it inhomogeneous.

variation which in turn caused a broadening of the measured Bragg peaks (see Figure 43). Results of relative range measurements for the different beam energies are presented in Table 5. The difference between the range measurements with different energies was within the uncertainties of the measurements.

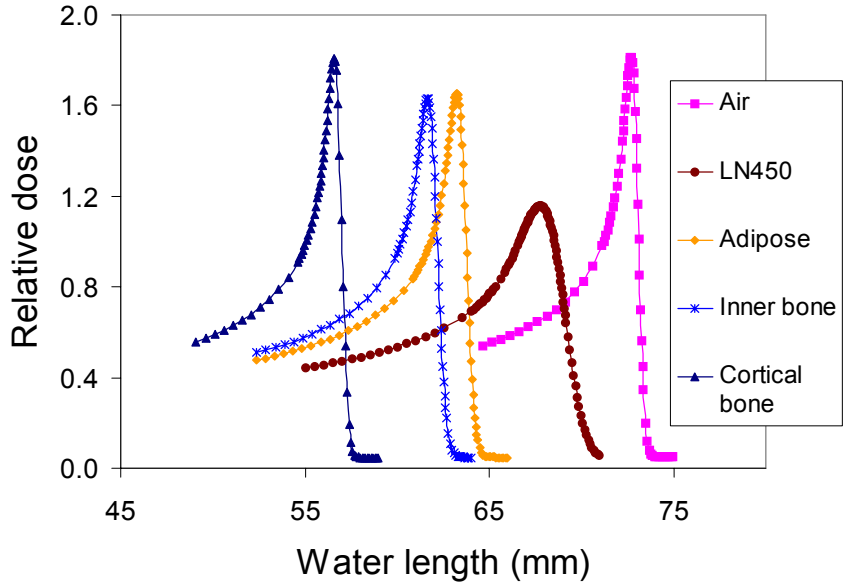

Figure 43. Depth dose curves measured of a 184 MeV Carbon ions due to passing through one centimetre of tissue substitutes. Measurements were carried out using the same intensity level for all different materials. The broadening of the peaks is due to straggling induced by the inhomogeneities of the inserts. The "Air" measurement was taken when no substitutes were placed in the beam path.

Measurements of the relative range of Gammex substitutes are presented as a function of the electron density in Figure 44. Measurements in the H-materials are shown for comparison. Both data sets have the same linear dependency on the electron density for both Gammex substitutes and H-materials; PMMA has the same dependency as the substitutes.

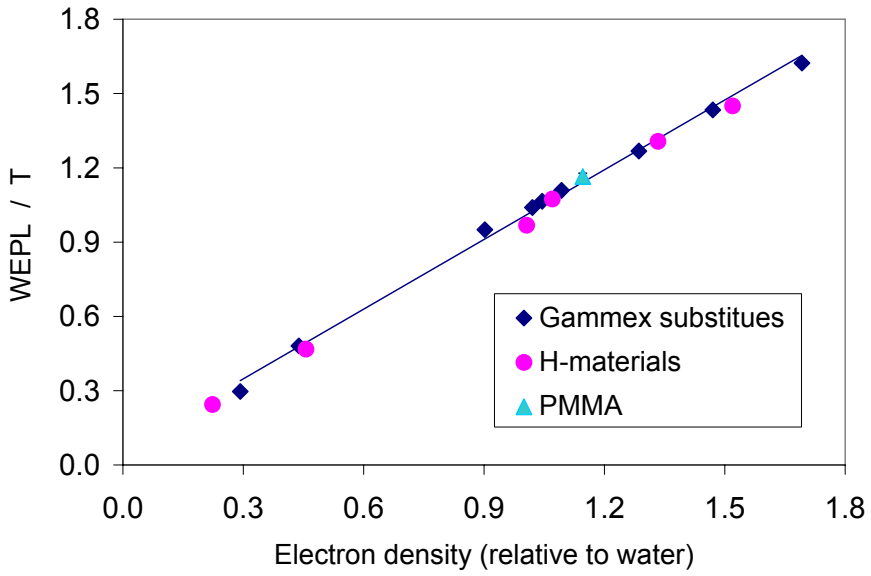

Figure 44. Relative range (WEPL/T) as a function of the electron density relative to water for Gammex substitutes, H-materials and PMMA. The WEPL measurements were performed using 270MeV/u Carbon beam. The uncertainties are plotted but they are smaller than being distinguishable.

Table 5. Results of CT-number and relative range measurements in Gammex substitutes and PMMA.

N	Substitute	Sensation 4 HU	Open HU	C-184 MeV/u Relative range	C-270 MeV/u Relative range
1	Lung 450	-587±24	-608±27	0.495±0.004	0.481±0.010
2	Adipose fat	-120±5	-123±6	0.950±0.005	0.950±0.008
3	Breast	-63±5	-64±6	0.991±0.005	--
4	Solid water	-8±6	-10±6	1.017±0.005	--
5	Brain	1±5	2±6	1.066±0.007	1.065±0.010
6	Muscle	25±6	23±7	1.042±0.005	1.040±0.007
7	Liver	66±6	68±6	1.079±0.005	--
8	Inner bone	265±6	264±6	1.111±0.005	1.109±0.007
9	Bone mineral	273±6	273±7	1.115±0.005	--
10	CB2 30%	533±7	536±7	1.263±0.006	1.268±0.011
11	CB2 50%	971±11	972±11	1.432±0.006	1.434±0.010
12	Cortical bone	1440±16	1443±18	1.619±0.006	1.623±0.010
13	PMMA	124±8	128±7	--	1.170±0.011

4.3. Substitutes vs. real tissues

The CT measurements were performed under the same conditions for the CT-measurements of the Gammex substitutes. A 270 MeV/u Carbon beam was used to measure the WEPL of tissue and bone samples. Results are shown in Table 6.

Table 6. CT-number and the relative range (WEPL/T) measurement results in tissue samples.

N	Tissue	Sensation 4 HU	Open HU	C-270 MeV/u Relative range
1	Lung 1	-636±137	-639±134	0.398±0.019
2	Lung 2	-369±124	-374±118	0.669±0.010
3	Lung 3	-356±123	-372±84	0.687±0.010
4	Fat 1	-104±9	-96±9	0.962±0.004
5	Fat 2	-98±13	-101±13	0.986±0.006
6	Fat 3	-98±18	-102±11	0.967±0.003
7	Brain1	33±8	33±7	1.031±0.005
8	Brain2	33±9	32±7	1.030±0.005
9	Brain3	32±12	29±11	1.031±0.005
10	Brain4	31±11	30±9	1.031±0.003
11	Kidney	46±8	45±6	1.042±0.005
12	Muscle, diaphragm	58±8	49±9	1.049±0.005
13	Muscle, leg 1	57±9	55±7	1.048±0.004
14	Muscle, leg 2	52±16	51±17	1.045±0.005
15	Muscle, leg 3	53±19	50±15	1.049±0.005
16	Liver	66±9	65±7	1.063±0.006
17	Fresh spongy bone	571±151	567±144	1.300±0.041
18	Human cortical bone	1177±169	1143±120	1.645±0.018

The variation of CT-numbers with the length of probes was examined for each tissue probe. Considerable inhomogeneities are observed in the Lung and bone samples. The variation from one slice to the consequent slices varies by up to 50 HU for the lung and 20 HU for the “human

cortical bone" sample. For the remaining tissue samples the variation of CT-number along the different slices is within ±5 HU.

The measured relative range is shown as a function of measured CT-numbers in Figure 45. The graph also shows the calibration (piecewise fit) based on the measurements of WEPL and CT-numbers in Gammex substitute. In a test to quantify the agreement between the tissue samples and Gammex substitutes, the relative range of the samples was calculated using a piecewise-fit which is based on measurements in Gammex substitutes; the relative range which was calculated by the piecewise-fit was compared to measured relative range of real tissues. The deviation between the measured and fit-calculated range in real tissue samples was less than 4% for all samples except for the Human cortical bone sample. The deviation for PMMA was 6%.

4.4. Measured energy spectra of X-ray tube in comparison to other data sources

In this section the measured spectra of the DURA 352-MV X-ray tube are presented. The energy spectra obtained from the different sources (the simulated spectra and the spectra provided by Siemens) are also presented and compared to measurement results for the different nominal voltage, in the center of the FOV and off-axis.

The measurements of the spectra were carried out for the nominal settings of 80, 110 and 130 kV. However, the real voltage settings of the X-ray tube were 79.3, 101.9 and 121.7 kV respectively. The measured spectra (in and off center) are presented Figure 46. Figure 47 presents the energy spectra of the DURA 352-MV X-ray tube which were simulated using BEAMnrc/EGSnrc. The Siemens spectra have already been presented in Figure 30.

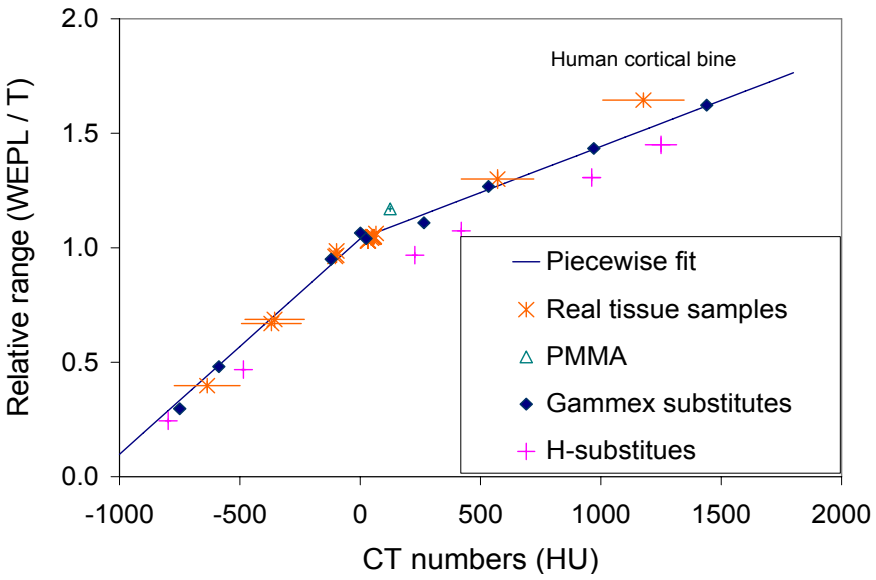

Figure 45. Measured relative range as a function of measured CT-numbers. Measurements in Gammex electron density substitutes, H-substitutes (Jäkel et al. [6]) and real tissue measurements.

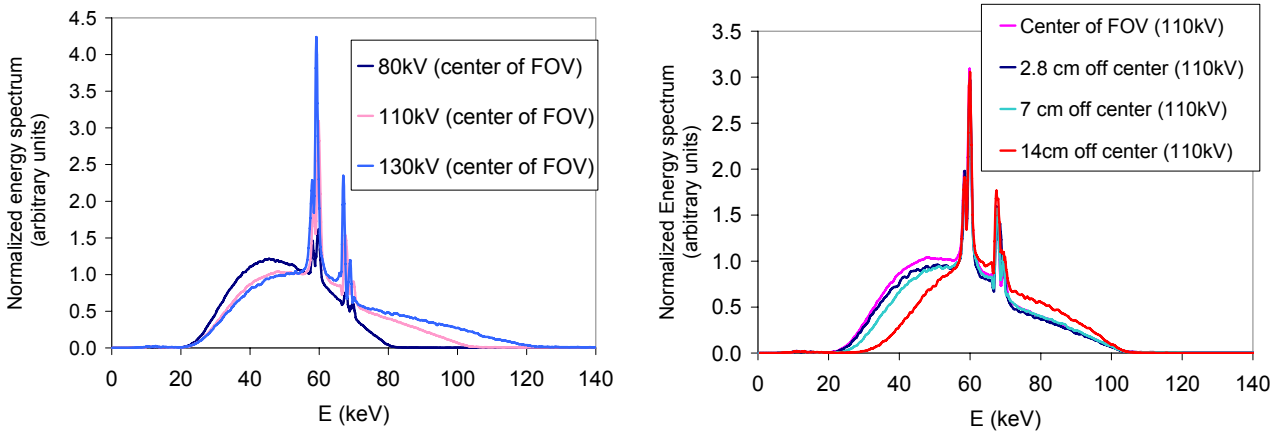

Figure 46. Measurements of energy spectra of Dura 352-MV X-ray tube; left are measurements in the center of FOV; right are the off-axis measurements for 110 kV setting.

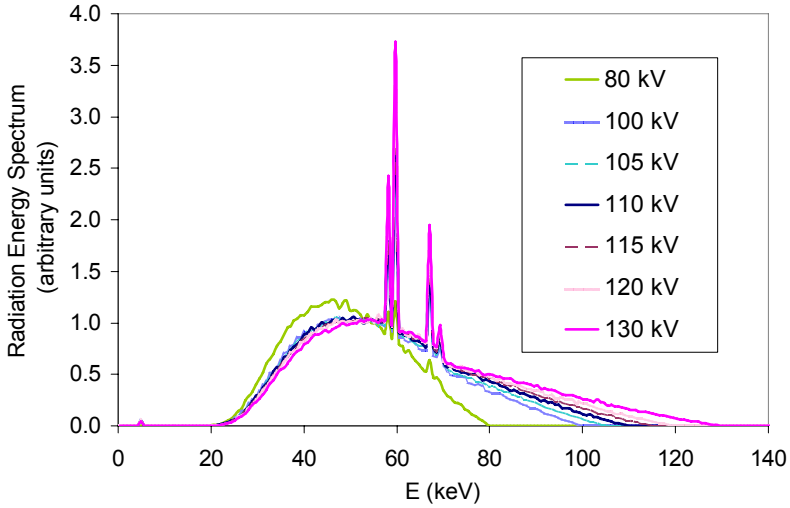

Figure 47. Simulated energy spectra using BEAMnrc/EGSnrc MC Code.

The spectra were compared using three different properties: the position of the characteristic peaks, the K-ratio and the mean energy of the spectra.

4.4.1. The position of the characteristic peaks

Comparing the characteristic lines in measured spectra to the lines in Siemens spectra, the $K_{\alpha 1}$ characteristic peaks in the Siemens spectra appear at higher energy (60 keV) than either the measured of simulated peaks (59.2, 59.6 keV respectively). The position of the K-lines is listed in Table 7. The binning of the spectra from the different sources is 1 kV for the Siemens spectra, 0.75 kV for the simulated spectra and 0.173 kV for the measured spectra.

4.4.2. The K-ratio

The K-ratio was defined as the number of characteristic photons relative to the total number of photons in spectrum. The characteristic lines were defined between 56 and 61 keV for the K_{α}

and between 65 and 71 keV for the K_β lines. The estimated accuracy of the K-ratio is 2%[11]. The K-ratios for the spectra at the center of FOV are listed in Table 8. The Siemens spectra locate about 5-10% more photons in the characteristic peaks than either the simulation of the measurements.

Table 7. Position of the K-lines of tungsten (Z = 74) from literature, simulations, measurements and Siemens spectra.

	Literature Position (kV)	Measurement Position (kV)	Siemens Position (kV)	Simulation Position (kV)
$K_{\alpha 1}$	59.48	59.52	60	59.63
$K_{\alpha 2}$	58.12	57.97	--	58.13
$K_{\beta 1}$	67.87	67.13	68	67.13
$K_{\beta 2}$	69.65	69.54	--	69.38

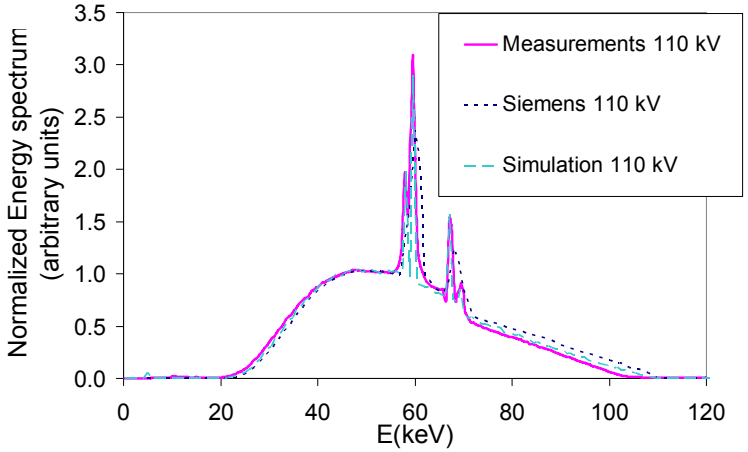

Figure 48. Comparison between measured, simulated and Siemens spectra of the nominal X-ray tube voltage 110 kV.

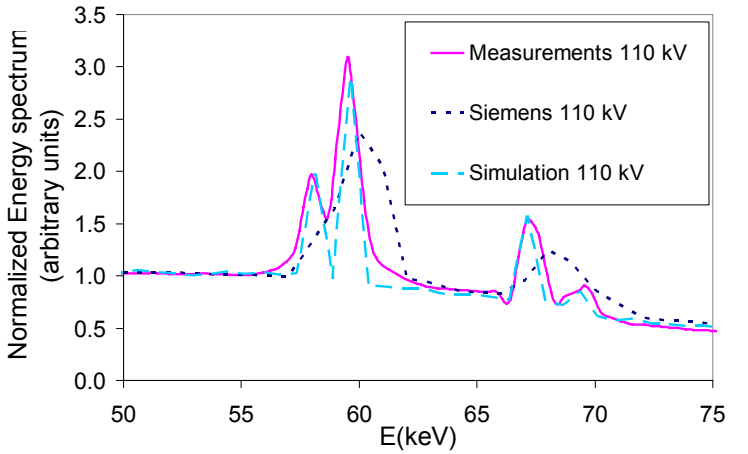

Figure 49. Comparison of peak positions of measured, simulated and Siemens spectra of the nominal X-ray tube voltage 110 kV.

[11] The K-ratio varied by 2% maximum depending on whether the characteristic peaks were de-convolved or not.

Table 8. Percent K-ratio of the various spectra depending on the peak voltage and the method of calculation. The spectra were measured and calculated at the center of the FOV.

kV	MC simulation	Measurement	Siemens
80	12	16	22
100	16	--	--
105	16	--	28
110	17	21	28
115	17	--	29
120	17	--	--
130	17	23	28

4.4.3. The mean energy of the spectra

The mean energy was calculated using equation (3.1). The uncertainty in the mean energy was calculated using equation (3.4).

The mean energy at the center of the FOV is listed in Table 9 for the simulated, measured and Siemens spectra as a function of the nominal voltage. However, the actual voltage settings for the measured spectra are 79.4, 101.8 and 121.8 corresponding to the nominal voltages 80, 110 and 130 kV, respectively. In general, the difference between the three sources of data is within the uncertainty of the calculated mean energy. The Siemens spectra appear to have a slightly higher mean energy than the other sources (see Table 8). In Figure 50, the mean energy is shown as a function of the actual peak voltage of the incident photons.

Table 9. Mean energy of the various spectra (at the center of the FOV) depending on the peak voltage and the method of calculation.

Nominal voltage (kV)	MC simulation $\overline{E}$ (kV)	Measurement $\overline{E}$ (kV)	Siemens $\overline{E}$ (kV)
80	49.2 ± 1.0	49.8 ± 0.2	50.3 ± 1.2
100	55.6 ± 1.0	--	--
105	57.0 ± 0.7	--	58.7 ± 1.2
110	58.4 ± 1.0	57.2 ± 0.2	60.2 ± 1.2
115	59.7 ± 0.7	--	61.4 ± 1.2
120	61.0 ± 1.0	--	--
130	63.5 ± 1.0	62.4 ± 0.2	64.8 ± 1.1

The mean energy is presented as a function of the distance from center of FOV in Figure 51.The solid lines show the mean energy calculated from the full simulation of the CT1-simulation for the voltage settings 100, 110 and 120 kV. The measurements indicate that the attenuation across the FOV is stronger than predicted by the simulation. The Siemens spectra at the edge of the FOV have higher mean energy than the simulation results and appear to be in good agreement with the trend of measured results.

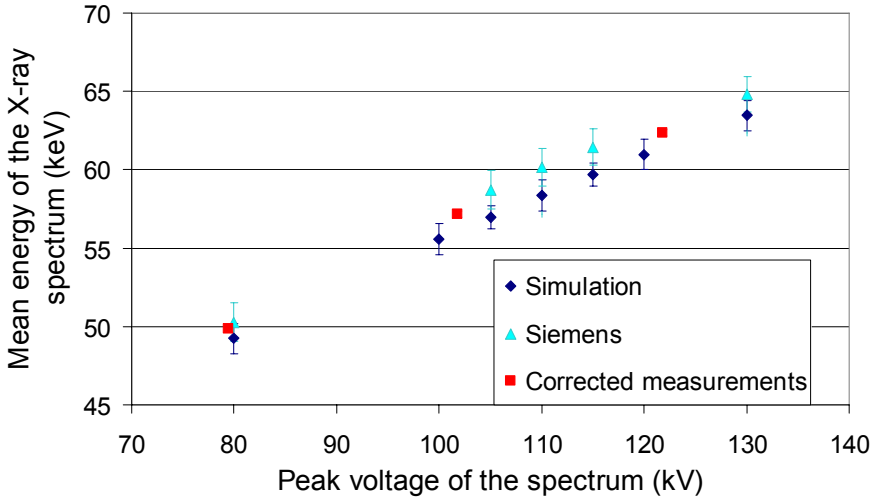

Figure 50. Mean energy of measured, simulated and Siemens spectra at the center of the FOV.

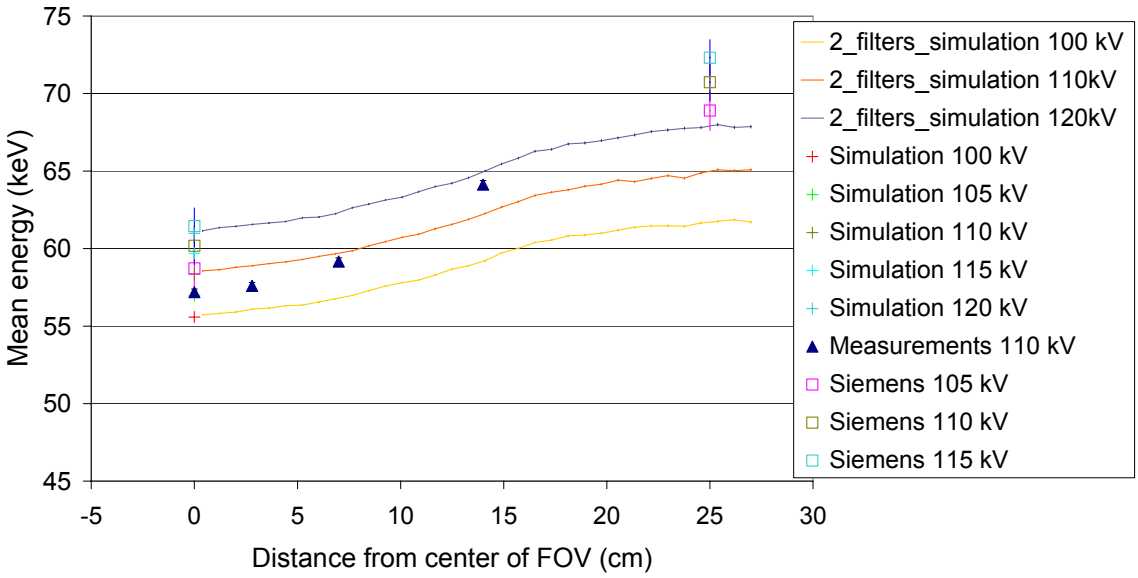

Figure 51. Mean energy as a function of the distance from the center of the FOV as calculated for spectra from various sources. The solid lines indicate the mean energy calculated from the full simulation of the filters.

4.5. Analysis of simulation set up

4.5.1. Efficiency and duration of the simulation

The efficiency of the simulation is calculated as the number of photons of interest (which are recorded in the PHSP files) relative to the total number of incident photons. In general, the efficiency of the simulation is poor. It is about 1% for the CT1-part of the simulation and about 5% for the CT2-part.

The absorption in the filters and collimators (CT1) increases with decreasing peak energy of the incident photons in CT1. Therefore, the efficiency of the CT1-simulation increases with the energy of the incident photons.

Simulations run faster when high ECUT values are used. The duration of the simulation also increases with the number of incident photons.

For illustration, a simple example is shown. A slab of substitute material is irradiated with a photon beam of a given spectrum. The simulations were performed for varying slab thicknesses (1 and 10 cm) and for LN450 (e-density relative to water is 0.4) and for cortical bone substitutes (e-density relative to water is 1.7). The number of incident photons was kept the same for all simulations. The CPU-time needed to perform the set tasks is shown as a function of ECUT in Figure 52. Indeed, simulation time is reduced by increasing the values of ECUT. The reduction of computation time increases if more interactions are expected (denser materials or thicker slabs).

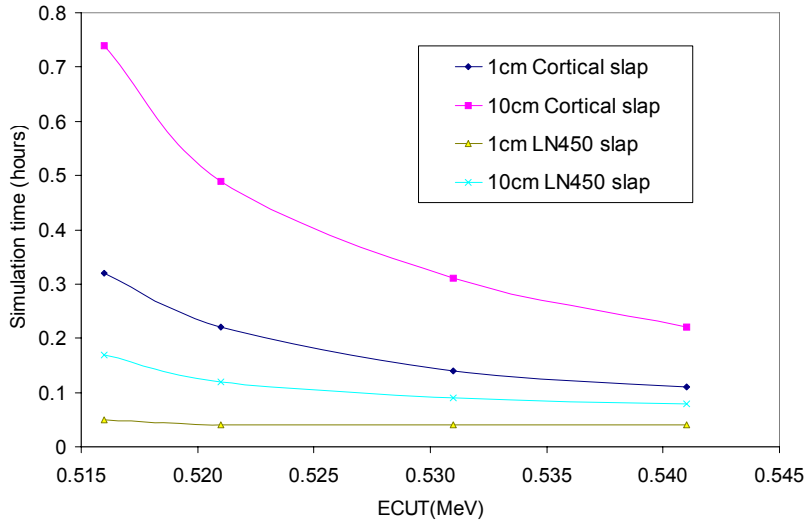

Figure 52. Effect of ECUT on duration of simulation. Effect of choosing higher ECUT values was more pronounced in simulations involving more interactions such as dense materials or thick slabs.

The time needed to perform a CT1-simulation with an ECUT value of 0.521 MeV is 18% less than the time needed when an ECUT value of 0.516 MeV is used.

Changing PCUT values did not affect the duration of the simulation. As a result, a PCUT value of 0.001 MeV was maintained throughout the simulation.

Usually 10^{10} photons are used for CT1 simulations and $5x10^8$ photons are used for CT2 simulations. If the photons in the CT1-PHSP file are less than required for the CT2-simulation (e.g. $5x10^8$), the code was allowed to repeatedly use the photons in the CT1-PHSP (recycle) until the set number of photons is achieved. The number of times that CT1-PHSP is recycled varied with the peak voltage of the incident photon spectrum. The CT1-PHSP file was recycled for 5 times with the voltage setting of 110 kV to generate $5x10^8$ incident photons for the CT2 simulation.

The simulations were carried out on two Pentium4 Linux PCs with 3GHz CPU power and 1GB RAM. The simulation of the CT1-PHSP with 10^{10} incident photons took one week of CPU time

for each set of parameters. CT2 part of the simulation required a maximum of 3 hours of CPU time to simulate $5x10^8$ incident photons.

4.5.2. X-ray tube approximation

X-ray tube was approximated by an isotropic source with a rectangular beam field. The variation of the fluence and mean energy along the two dimensions (in slice and along Z-axis of CT scanner) are shown in Figure 53 for the fully simulated X-ray tube and the isotropic source approximation.

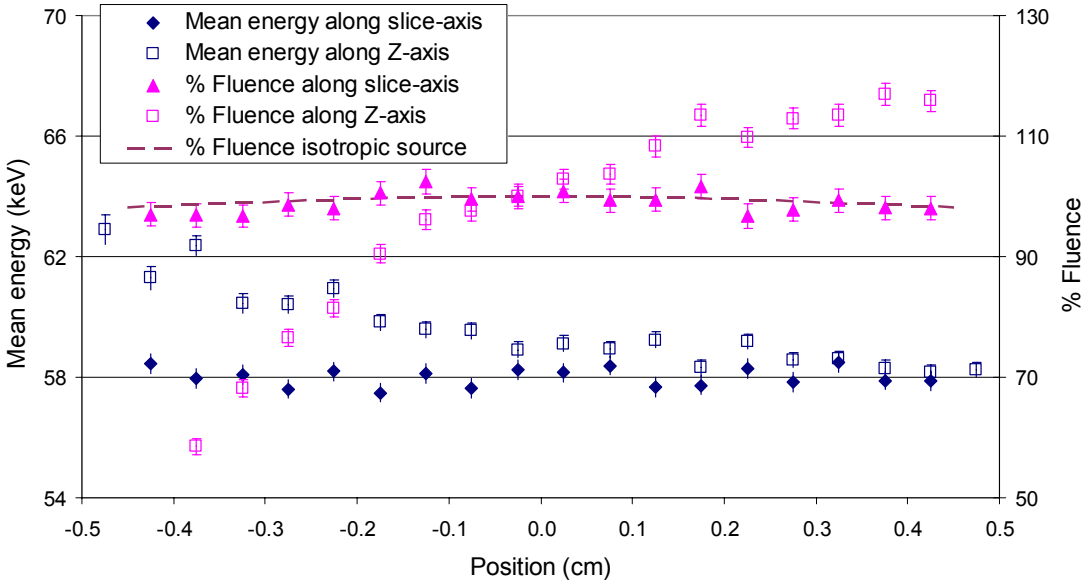

Figure 53. Quality of the approximation of X-ray tube by a point source. The points represent the change of mean energy of spectrum (scale to left) and percent fluence of photons (scale to right) generated using MC simulation of the DURA 352-MV X-rays tube with voltage setting of 110 kV. The dashed line represents the results from the approximation. The data is calculated for the slice-axis for a z-position of zero. It was calculated along the z-axis a the y-position of zero (center of the slice-axis).

Full simulation of the X-ray tube demonstrated that the fluence of emitted photons varied by 3% with position in the photon field. The approximation agrees very well with the fluence of photons within the slices. However, fluence from the isotropic source is symmetric in both the slice and the z-axis and hardly represents the beam profile along the z-axis.

The simulation also indicated that mean energy variation of 0.7% is expected along the slice-axis. Higher variations are observed along the z-axis due to the heel effect. The energy of the isotropic source approximation shows no variation along either dimension and was set to the required energy spectrum.

4.5.3. Detector response

A standard phantom containing cortical bone insert was analysed twice. The signal which was first calculated while including detector response is referred to as I_{phanCB}^{resp}. Then, the signal calculated while assuming equal weights for all photons ($I_{phanCB}^{no\_resp}$) i.e. no detector response. To calculate projection data ($-\ln(I/I_0)$), the signal when only air is in the FOV (I_0) should be

calculated. I_0 values were calculated with and without detector response, I_0^{resp} and $I_0^{no\_resp}$ respectively. The projections, when the detector response is taken into consideration, were:

$$P^{resp} = -\ln(I_{phanCB}^{resp} / I_0^{resp}).$$

Similarly, when equal weights are given to the photons, the signal was P^{no_resp}.
The maximum difference between the projection data (P^{resp} and P^{no_resp}) was observed in the central detector elements. The difference was calculated as:

$$\frac{100 \times \sqrt{\left(P^{resp} - P^{no\_resp}\right)^2}}{\left(P^{resp} + P^{no\_resp}\right)/2}.$$

It reached a maximum value of 0.09%.

As a result, no significant effect was observed on the projections due to the implementation of the detector response. Nevertheless, the detector response was applied for all simulations.

4.5.4. Scatter corrections

The signal resulting from applying the scatter corrections (see 3.6.7) is shown here for a cylinder of water, 25 cm diameter, which was simulated in the center of the FOV.

Scatter was calculated twice. First, photons were allowed to suffer multiple scattering (scatter-1 pattern) and photons were identified as scatter if they do not fulfil equation (3.11). The resulting scatter signal is equivalent to measurement conditions. Scatter-2 pattern was also assumed and photons which fulfilling equations (3.11) and (3.12) were assumed scatter-free photons. Figure 54 shows the calculated "true" and "scatter" counts for the water cylinder.

Photons which are scattered in small angles in the forward direction are assumed scatter-free photons which did not suffer any scatter on their way from the source; the result is the sharp increase of signal in central detector elements when scatter is calculated based on the angle of incidence (scatter 2). The corresponding pattern of the signal when only the scatter grid is taken into account (scatter 1) is more uniform. Furthermore, the ratio of the scatter counts to the "true" counts was 3% of the registered signal when the collimator grid position was used (scatter 1). It accumulated to 28% when "scatter 2" pattern was assumed.

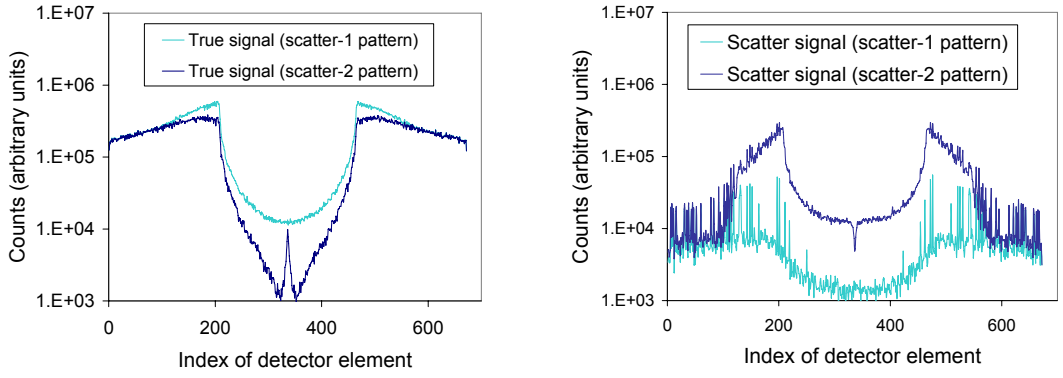

Figure 54. True and scatter signal for water cylinder which is simulated in the center of FOV using two methods to determine the scatter signal. Scatter pattern 1 is due to calculating scatter based on the position of the detector and collimating grid (light blue). Scatter 2 pattern happens when the scatter signal is calculated based on the impact angle (dark blue).

4.5.5. Beam hardening corrections

The code for beam hardening corrections (BHC) corrects the attenuation data of the projections for the chromatic energy distribution of the photons. The setting of the function $\psi(E)$ determines the targeted monochromatic energy. In this work, $\psi(E)$ was set with an effective energy of 40 kV.

To understand the effect of choosing another effective energy to perform the beam hardening corrections, 2 effective energies (40 and 120 kV) were used for beam hardening corrections. The resulting $\psi(E)$ are:

$$\psi_{40}(E) = \mu^{water}(E) / \mu^{water}_{40kV}$$

and

$$\psi_{120}(E) = \mu^{water}(E) / \mu^{water}_{120kV}.$$

Both functions are shown in Figure 55.

A homogeneous cylinder of water (25 cm diameter) was simulated using 3 voltage settings (80, 110 and 130 kV). The simulated projections were corrected for beam hardening using the two ψ functions ($\psi_{40}(E)$ and $\psi_{120}(E)$). The original polychromatic and the corrected monochromatic projections are shown in Figure 56. There, it is clear that the corrected projections are equal for a given effective energy. The absorption probability increases with decreasing effective energy and the value of the projections increases as seen from Figure 55.

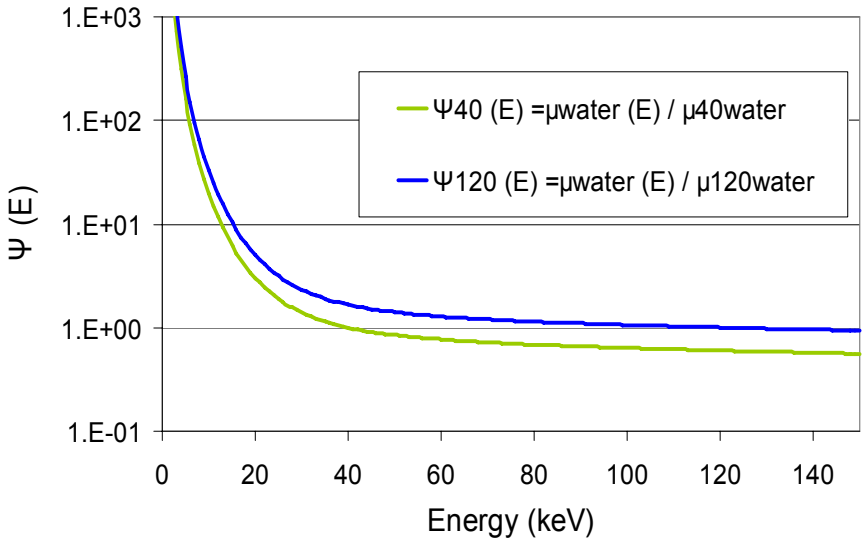

Figure 55. $\psi(E)$ defined for two effective energies (40 and 120 kV) for BHC.

The effect of applying BHC on CT-numbers is small since CT-numbers are relative values; the corrected attenuation coefficients are normalized using corrected coefficients for water. In water equivalent media, the difference between corrected CT-numbers and uncorrected values is minimal. The difference increases as the material deviates from water.

In Figure 57, simulated CT-numbers (without BHC) are compared to CT-numbers of a corrected image of Gammex substitute materials in the standard 16 cm diameter PMMA phantom. The maximum difference between the results is 17 HU which is well within the uncertainty of simulation (about 80-200 HU).

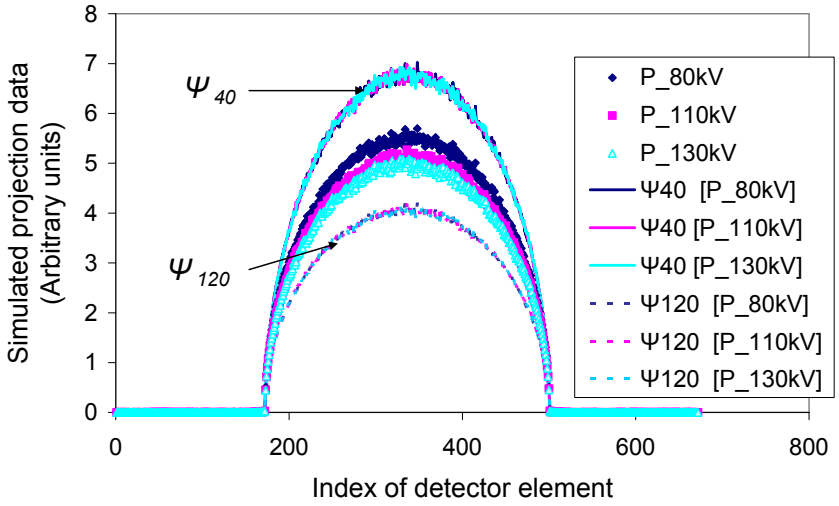

Figure 56. Effect of effective energy for beam hardening corrections on polychromatic water projections. Corrected monochromatic projections have the same effective energy. As the effective energy increases, the value of corrected projections decreases.

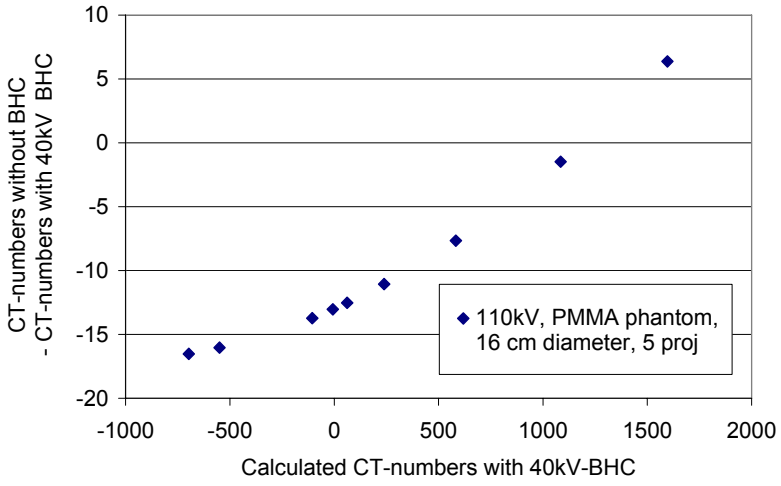

Figure 57. Difference between applying and discarding beam hardening corrections and on CT-numbers of Gammex substitutes in PMMA phantom.

However, the applied BHC assumes that all media interact with X-rays in the same way as water. This is a good approximation to most tissue types but not for bone. The best approach is to implement a weighted BHC. This is only possible if water-like media and bone-like media are distinguishable at the level of projections.

For the scope of this work only water based BHC were implemented since the uncertainty in the calculated CT-numbers is larger than the benefits expected from applying weighted BHC.

4.6. Accuracy of CT simulation

There are two aspects of the accuracy of the simulation: the uncertainties of the calculated CT-numbers and the deviation between calculated and measured CT-numbers.

4.6.1. Statistical uncertainty

The photons in CT2-PHSP are dependent on the distribution of photons in CT1-PHSP. Using different random number seeds for the simulations of the CT2 part can not completely eliminate this dependency. In Figure 58, the statistical effects of the number of incident photons, number of views, and the number of independent views are shown for a PMMA phantom with a cortical bone insert. The images show reconstructed attenuation coefficients (unnormalized CT numbers) along a line through the center of the image.

To illustrate the effect of statistical fluctuations on the reconstructed image, simulations of CT2 part of a PMMA phantom with a cortical bone insert were carried out using varying number of incident photons to calculate. As expected, increasing the number of incident photons per independent projection lowers the statistical variations in the profile across the reconstructed image (Figure 58 B and D).

Usually, 1000 views (10^6 independent projections) are reconstructed to form an image. However, a cylindrical phantom with cylindrical inserts has similar projections from all view points. The difference between the different views is more or less statistical fluctuations. The above assumption was used in this work to limit the simulation time. Few independent projections were simulated and the result of repeatedly using the projections for 1000 times. The result is that the fluctuations in the simulated projection are intensified and appear as ring artefacts in the calculated CT-image.

The simulated CT-pictures in Figure 58 A and B were calculated with varying number of independent views. The results indicate that the fluctuations in the image are clearly reduced by using more independent projections.

When a lower number of views is reconstructed, the fluctuations in the substitute region appear less but more fluctuations are seen in the phantom and base-line representing the air surrounding the phantom. Results are shown below in Figure 58 A and C.

4.6.2. Benchmarking simulation results with measured CT numbers

There are two sets of data that have been both simulated and measured: H-substitutes behaviour for 120 kV and the Gammex substitutes for 80, 110, 120 and 130 kV. The difference between simulated CT-numbers and measured values are shown in Figure 59.

The measurement results at 120 kV (see 4.2) indicate that H-materials behave differently from Gammex substitutes which closely imitate soft tissues as seen in Figure 45. The simulations of the CT-numbers of H-materials were carried out using the Emotion CT model with the voltage setting of 120 kV. Five independent projections were simulated for each of the substitutes assuming a PMMA phantom of 16 cm diameter in the center of the FOV. The difference between the measurement and simulation results is within the estimated uncertainty of the simulation as shown in Figure 59.

Measurements of Gammex-substitutes using 120 kV were performed using the Siemens Sensation 4 CT and The Siemens Sensation Open CT. Again, the simulations were performed using the Emotion model, 120 kV tube setting and 5 independent projections.

The simulation was based on the Emotion CT scanner despite the fact that it is different from either the Sensation4 scanner (used for measurements in this work) or the Somatom Plus 4 scanner (used by Jäkel et al. [7]). However, all three scanners are from Siemens and are of comparable design-generations.

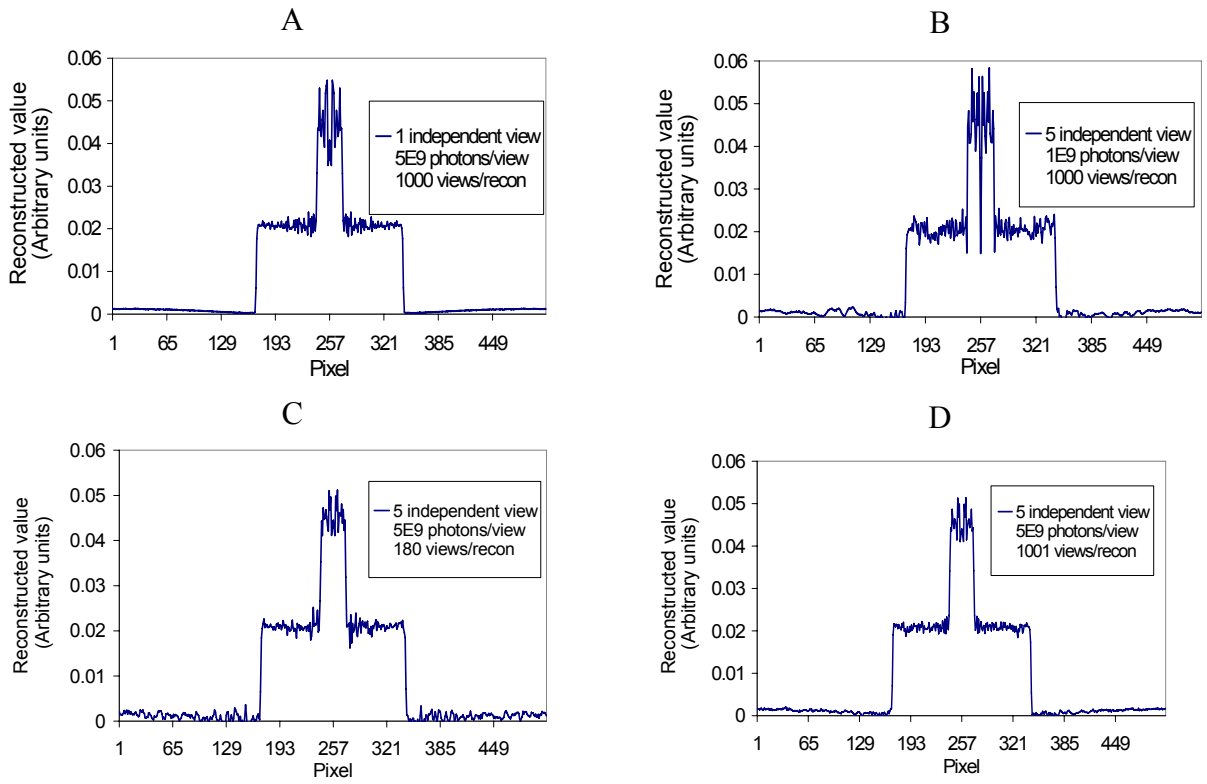

Figure 58. A profile through the center of a reconstructed CT image (512x512 pixels) from MC calculated projections of a 16 cm PMMA phantom with cortical bone substitute as an insert. The effect of number of incident photons, number of independent projections and total number of views on the reconstructed image is discussed for a profile in the center of a calculated CT-image.

The measurements of CT-numbers of Gammex substitutes which were performed using 80, 110 and 130 kV settings of the Emotion CT scanner are sown in Table 16, rows 1-3. The measurements were carried out using the nominal voltage settings of 80, 110 and 130 kV. However, the exact voltage settings of the scanner were 79.3, 101.9 and 121.7 kV.

The simulations used for the comparison are the 80, 100 and 120 kV. The simulations were calculated using 5 independent projections for both the 80 and 120 kV settings but only for one projection for the 100 kV. The effect of using one independent projection instead of five is an overestimated uncertainty in the calculated CT-numbers as seen in Figure 59.

The deviation from the measured value was always within the uncertainty of the simulation. A histogram of all the data points in Figure 59 for each data series is shown in Figure 60. The simulation results are randomly distributed around the measured values. The distribution can be described by the Gaussian function (G) such that:

$$G(x) = A \cdot \exp\left(-\frac{(x-\bar{x})^2}{2\sigma^2}\right). \qquad (4.1)$$

Here, x is the difference between measured and calculated CT-numbers; the average deviation ($\bar{x}$) is 12±5 HU. The standard deviation (σ) is 53±5 HU and A is 14±1.

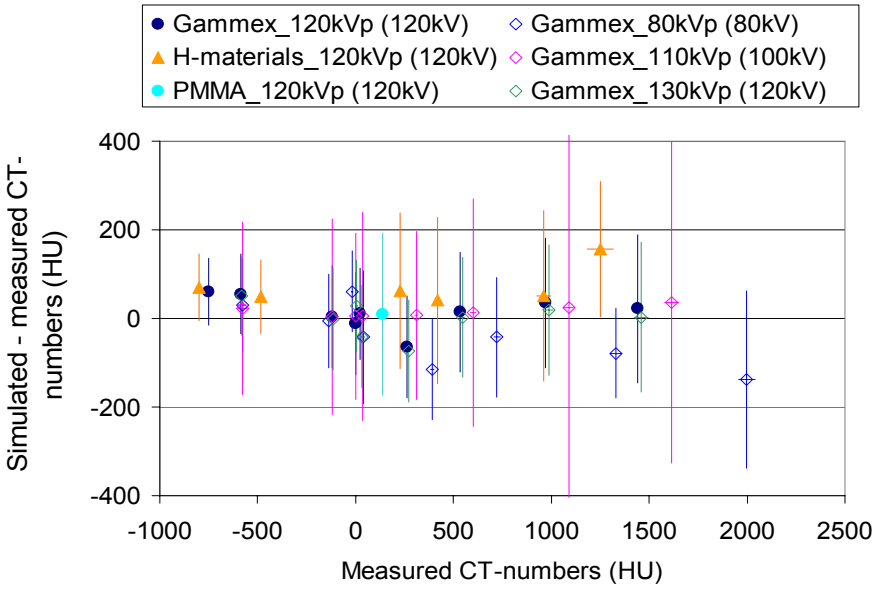

Figure 59. Difference between simulated and calculated CT-numbers vs. measured CT-numbers. The type of substitutes and the voltage setting of the CT measurements (and simulation) are indicated for each data set.

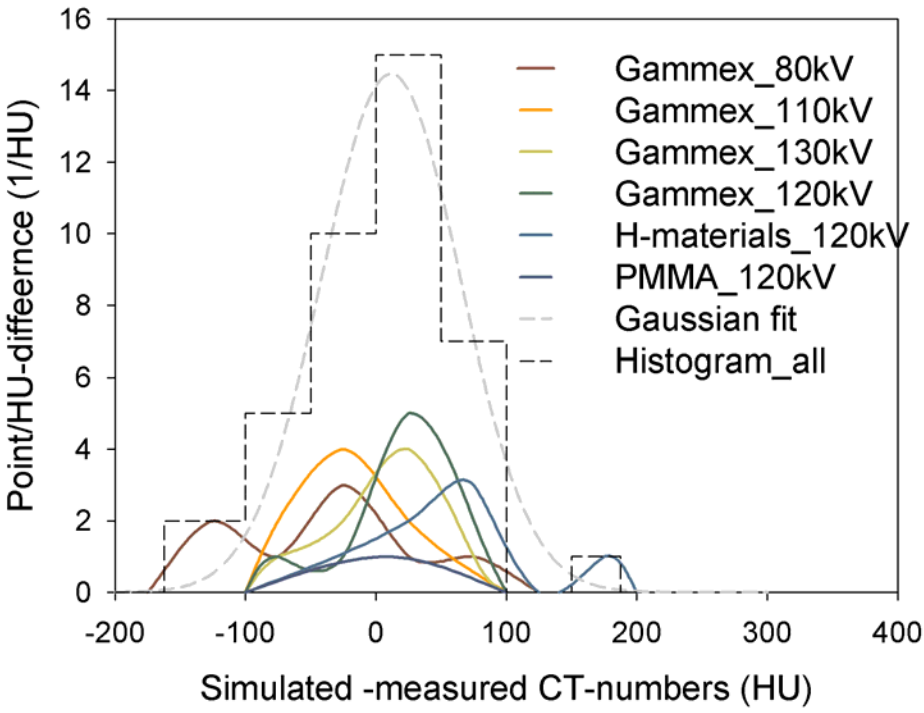

Figure 60. Distribution of the simulated CT-numbers around measured values. The graph shows the histograms of the data points as a function of the difference between the simulated and measured CT-numbers. The histogram for all the data points (Histogram_all) and the "Gaussian fit" G(x) in equation (4.1) are also shown.

4.7. Simulated effects

To study the effects on CT-numbers, the simulations were carried out for a set of parameters (see Table 3). The standard setting for the simulation is a 16 cm diameter phantom of PMMA with Gammex substitutes as inserts. The phantom is irradiated with 110 kV photon beam. The simulated CT-numbers are available in Table 18.

4.7.1. Effect of filters on energy spectrum and fluence

The two filters (Aluminium and Teflon) were studied in terms of their effect on the energy fluence and the spectral distribution at the center and the edge of the FOV. Figure 62 shows the comparison of the spectral distribution for different filters used in CT1. It is clear that the Al filter causes most of the beam hardening of the spectrum especially at the edge of the FOV. The Teflon filter, on the other hand, causes further attenuation and smoothes the beam profile as seen from the energy fluence distribution vs. position in Figure 63 which is calculated for different filters and 110 keV X-ray tube voltages. The Aluminium filter causes the attenuation of the primary beam by 44% while the Teflon filter alone causes the attenuation by 25%. However, both filters attenuate 54% of the beam, when combined.

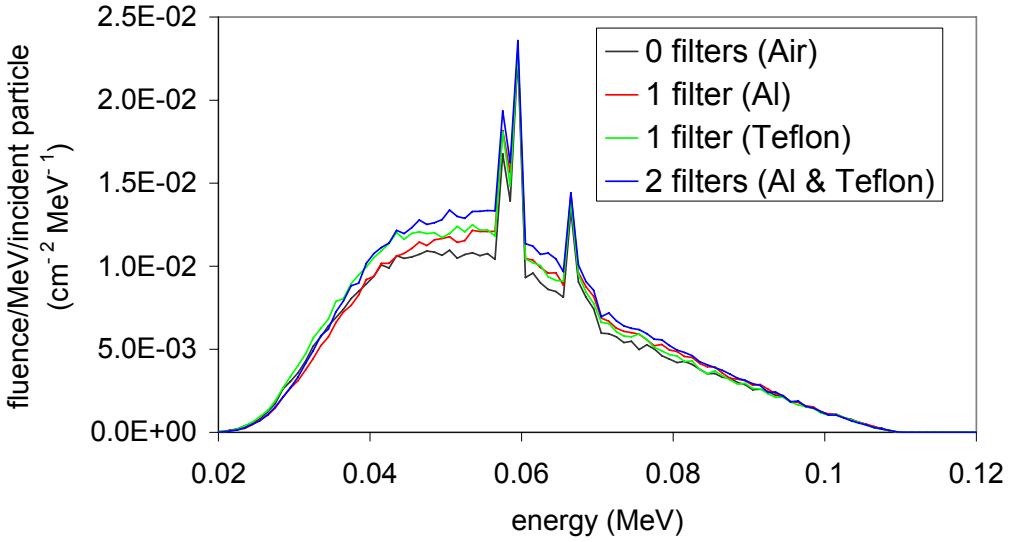

Figure 61. Photon spectral distribution for different filters used in the CT1 calculated in the centre of FOV for a 110 keV X-ray tube voltage.

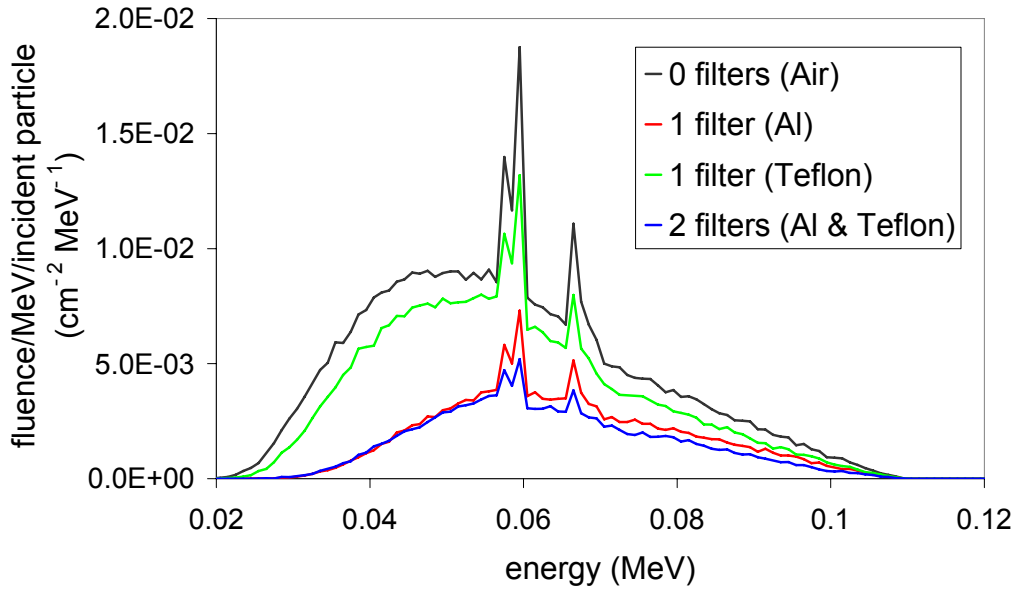

Figure 62. Photon spectral distribution for different filters used in the CT1 calculated at the edge of FOV for 110 keV X-ray tube voltage.

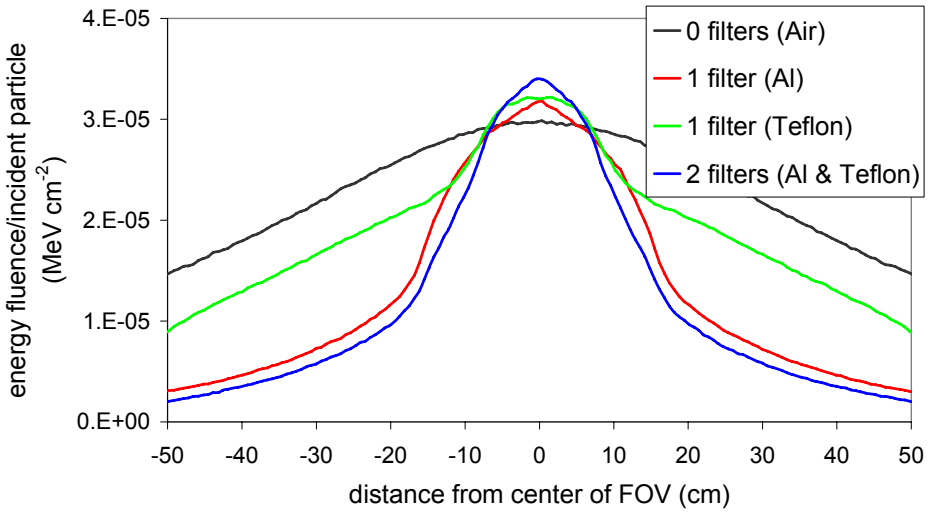

Figure 63. Energy fluence distribution vs. position in the FOV from the different filters.

The mean energy as a function of position from the center of the FOV is shown Figure 64 for the different filter arrangements in CT1. In 4.4, the measurements of the spectral distribution off axis were compared to simulation results of the CT1 with 2 filters (Aluminium & Teflon). In Figure 64, the mean energy of the measured spectra was found higher than the simulated values.

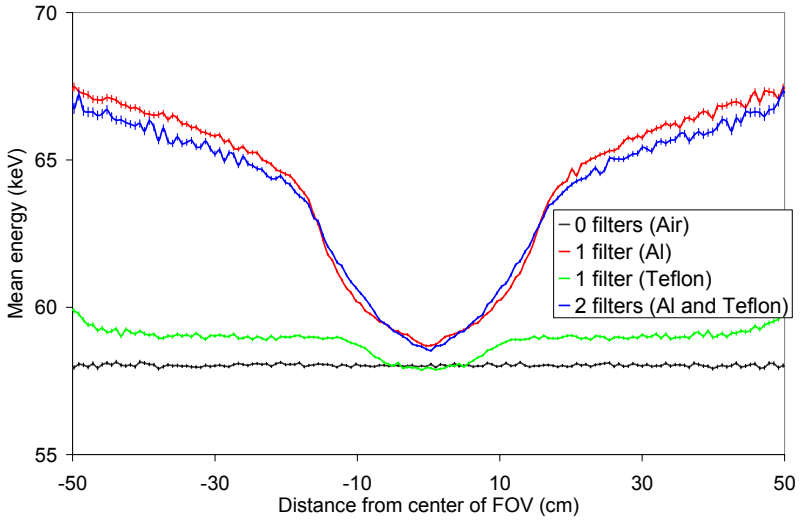

Figure 64. Mean energy as a function of the distance from the center of the FOV, calculated for different filter arrangements in the CT1-simulation.

4.7.2. Phantom inserts

4.7.2.1. Energy spectrum and fluence for Gammex substitutes

In Figure 65, the effect of the presence of Gammex substitutes in the beam path on the spectral distribution and the energy fluence is shown. Figure 65-left shows that as the electron density of the substitute increases, it causes more beam hardening. Note that there was a residual beam hardening form the PMMA phantom where the substitutes were held. The mean energy of the spectrum changed from 58.4 kV (initial spectrum of 110 kV) to 64.8 kV for the PMMA phantom with a LN300 insert and 69.9 kV for PMMA phantom with a cortical bone insert. The uncertainty in the calculated mean energy is maximum 1 kV. Moreover, as the density of the

substitute increases, the attenuation of the beam increases. Figure 65-right shows the energy fluence vs. position in the center of the FOV.

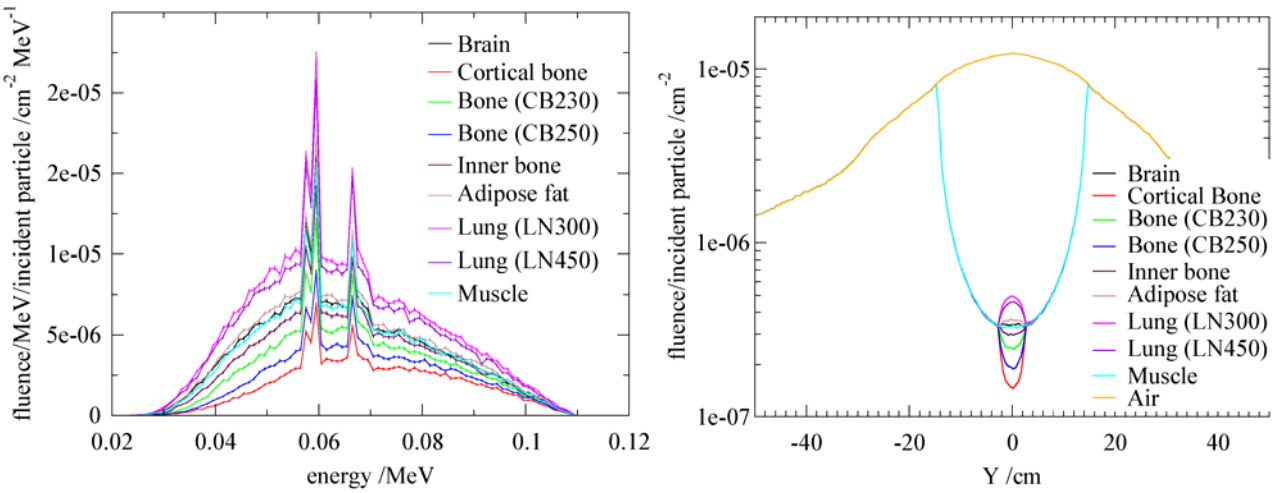

Figure 65. Effect of substitute material on spectral distribution and energy fluence. The energy spectral distribution (left) and energy fluence distribution vs. position in the FOV (right) of X-ray beam calculated after the phantom with different inserts; the number of initial particles from the source is $5x10^8$ photons; initial X-ray tube voltage is 110 keV.

4.7.2.2. CT-numbers of Gammex substitutes and H-materials

The simulations of the CT-numbers were carried out using the Emotion CT model with the voltage setting of 120 kV. 5 independent projections were simulated for each of the substitutes assuming a PMMA phantom of 16cm diameter in the center of the FOV.

Figure 66 shows the relative range (WEPL/T) as a function of CT-numbers for Gammex substitutes, H-materials and PMMA. The term “measurements” indicated measured stopping power ratios as a function of measured CT-numbers. Similarly, “simulated” indicated the simulated relative range as a function of simulated CT-numbers. The results of simulation successfully predicted the behaviour of H-substitutes (compared to Gammex substitutes).

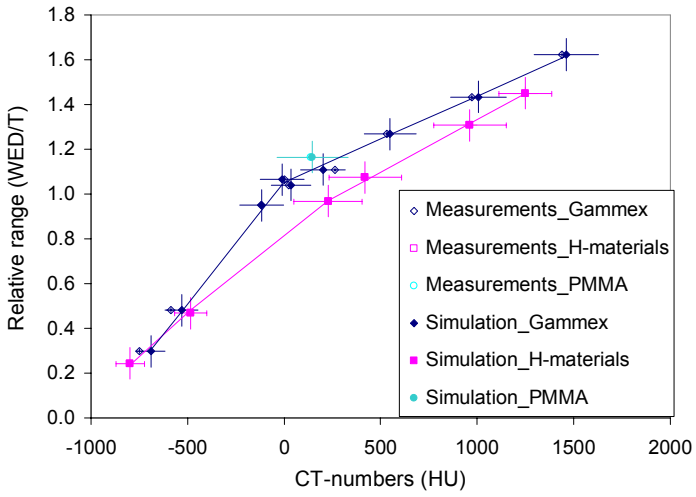

Figure 66. Comparison of calculated and measured results of relative stopping power as a function of CT-numbers for Gammex, H-materials and PMMA.

4.7.3. Voltage settings

4.7.3.1. Effect of voltage settings on spectra and energy fluence

The attenuation changes with the energy of the incident photons. Figure 67-left is a comparison of the spectral distributions calculated after a PMMA phantom and a cortical bone insert. In Figure 67-right, the energy fluence vs. position in the FOV is drawn for three initial spectra (80, 110 and 130 kV) when PMMA phantom and cortical bone insert are in the center of the FOV. For the initial spectrum of 80 kV, the initial mean energy is 49.2 kV; it increases to 57.4 kV after the interaction with the PMMA phantom and cortical bone substitute. The corresponding change for the 110 kV photons is from 58.4 to 69.9 kV and for the 130 kV is from 63.5 kV to 77.4 kV.

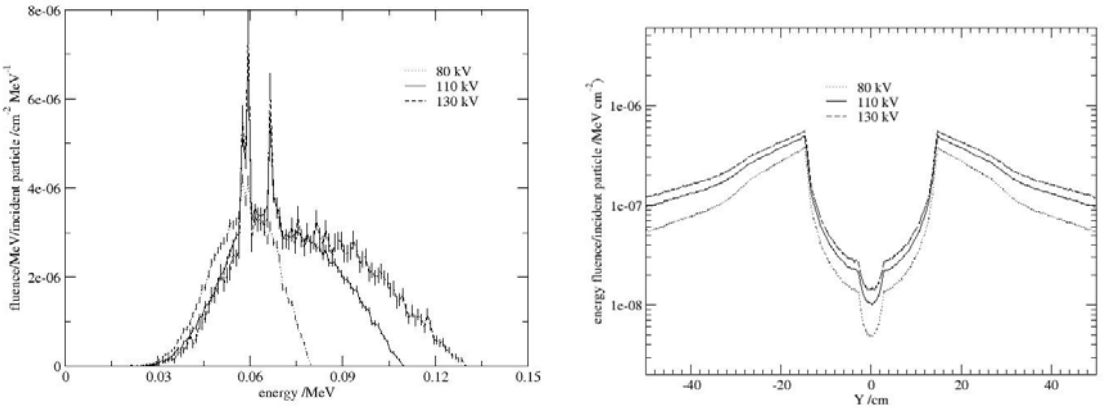

Figure 67. Effect of incident photon energy on spectral distribution and energy fluence. The spectral distribution (left) and energy fluence vs. position (right) were calculated after Plexiglas phantom of 16 cm diameter and Cortical bone insert for the incident X-ray tube voltage (80, 110, 130 kV) and $5x10^8$ photons as initial particles.

4.7.3.2. Effect of voltage settings on CT-numbers

Simulations were carried out for 7 different voltage settings[12]. However, only a subset of the simulations was carried out using 5 projections (80, 110, 120 and 130 kV). The remaining simulations were based on one independent projection. The simulations with only one independent projection carry a high uncertainty as seen in Table 18.

In Figure 68, the CT-numbers of Gammex substitutes are drawn as a function of voltage settings of the X-ray tube. The values for air and water have been used for calibration at the different voltage settings (3.6.11) therefore they are set to -1000 and 0 respectively. The CT-numbers shown in Figure 68 have not been corrected for the beam hardening effect, but little change is expected as seen from Figure 57 above.

[12] Part of the results has already been compared to measurements in Figure 59 as proof of simulation accuracy.

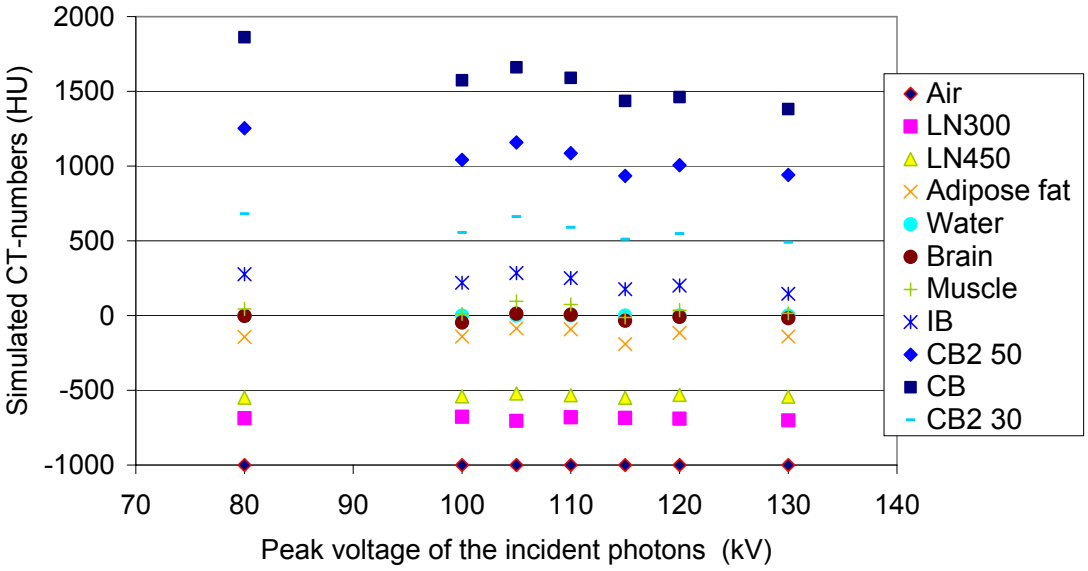

Figure 68. Effect of X-ray tube voltage on CT-numbers of Gammex substitutes. Simulations were carried out using a 16 cm diameter PMMA phantom.

The effect of voltage is important for bone-like substitutes whose electron density is larger than water and is strongest for cortical bone (-10 HU/kV). Tissue-like substitutes show almost no response to the voltage change.

The change of CT-numbers with voltage can be calculated assuming a linear relation between the simulated CT-numbers and kV. In Figure 69, the change of CT numbers with voltage is drawn as a function of the electron density of the different substitutes.

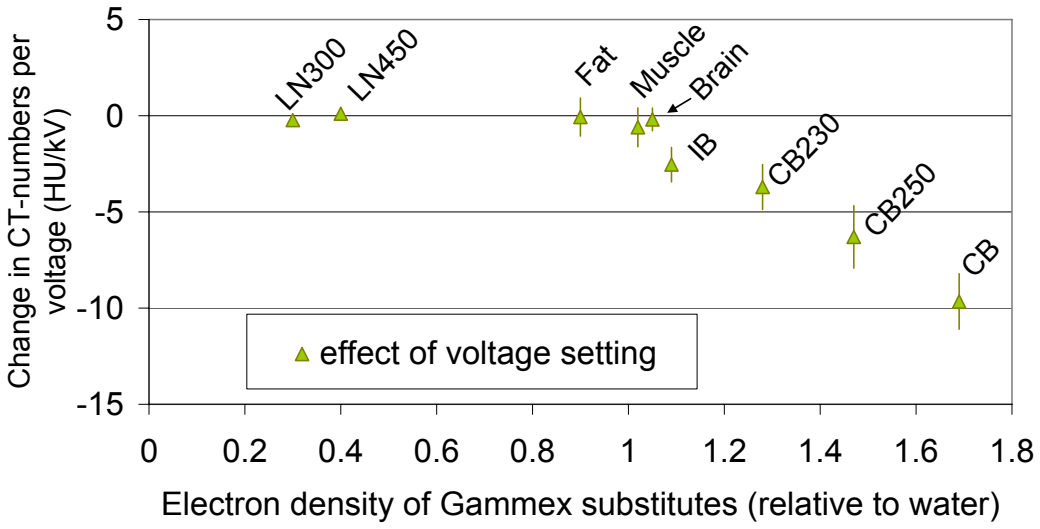

Figure 69. Change of CT-numbers per kV as a function of the electron density of the substitutes.

4.7.4. Effect of phantom size on CT-numbers

Simulations were carried out for 6 phantom sizes (12-32 cm diameter in steps of 4 cm). All the simulations were carried out using a single independent projection and 110 kV incident

photons. Beam hardening corrections were applied to each simulated projection and resulting CT-numbers are shown in Table 18.

In Figure 70, CT-numbers of Gammex substitutes are drawn as a function of phantom diameter. The diameter of the PMMA phantom appears to affect all substitute materials linearly. The effect increases with the difference of electron density to water and is strongest for cortical bone (-12 HU/cm).

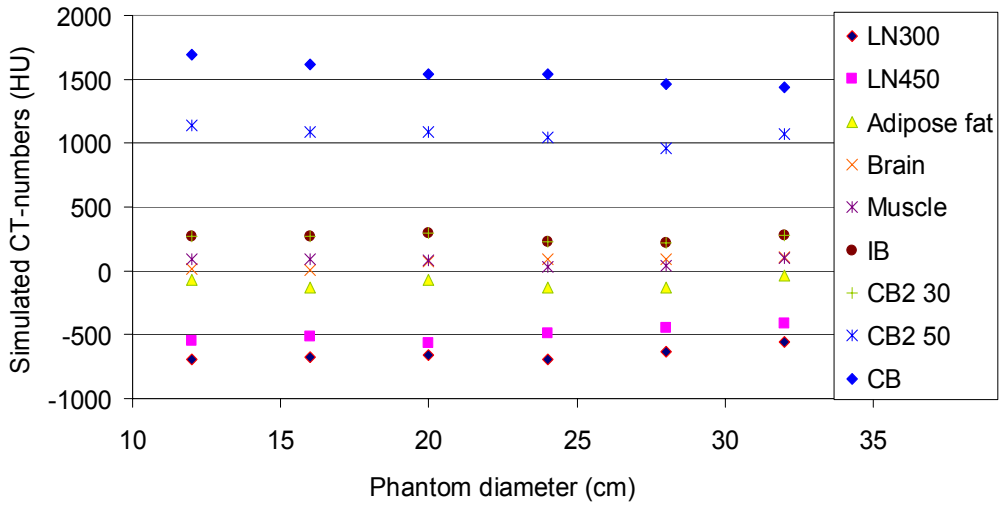

Figure 70. Effect of diameter of PMMA phantom on CT-numbers of Gammex substitutes. Simulations are using input spectra of 110 kV tube.

Figure 70 shows the change of CT-numbers as a function of electron density of substitute material. The change in CT-numbers was calculated assuming a linear relation between the simulated CT-numbers and phantom diameter.

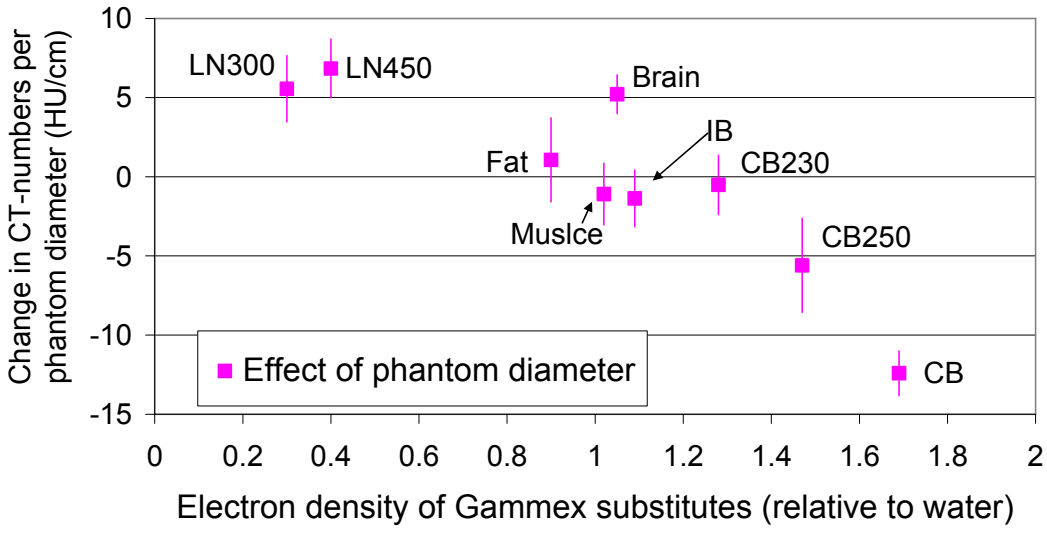

Figure 71. Change of CT-numbers per phantom diameter as a function of the electron density of the substitutes.

4.7.5. Effect of phantom material on CT-numbers

Simulations were carried out for 6 phantom materials: air, water, muscle, PMMA, RW3 and cortical bone. The assumption of air and cortical bone as phantom materials is unrealistic but they were simulated to set the lower and upper limits of applicable phantom electron densities. All the simulations were carried out using 5 independent projections for 110 kV incident photon energy and 16 cm diameter phantom of PMMA and resulting CT-numbers are shown in Table 18.

In Figure 73, CT-numbers of Gammex substitutes are drawn as a function of the electron density of the phantom materials. The effect is again strongest for cortical bone (-250 HU). Lung substitutes are also affected by extreme electron density of the air and cortical bone phantoms.

Beam hardening corrections were applied to all simulations of phantom materials. However, the applied correction is only valid for water-like medium. Therefore, CT-numbers measured in cortical bone phantom are expected to be under corrected and lower than they should have been. Nevertheless, CT-numbers tend to decrease with increasing electron density of the phantom materials. Quantitatively, it is possible to calculate the change in CT-numbers as a function of electron density for each substitute material by assuming a linear relation between the simulated CT-numbers and the electron density of the phantom materials.

The change was calculated twice, once when results of cortical bone phantom was taken into account and another when it was discarded. The resulting change per electron density of the phantom materials is shown as a function of the electron density of the substitutes in Figure 71.

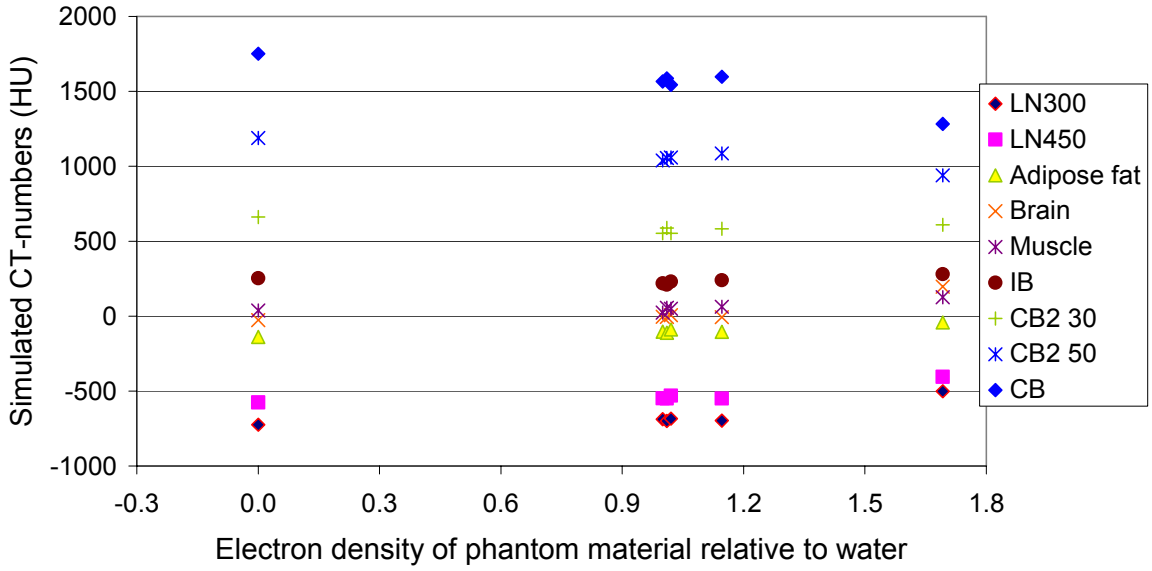

Figure 72. Effect of phantom material on the CT numbers. Simulations were carried out for a 16 cm diameter phantom and a 110 kV incident photon energy. The electron densities of the phantom materials are 0.00 for air, 1.00 for water, 1.01 for RW3, 1.02 for muscle, 1.15 for PMMA and finally 1.69 for cortical bone.

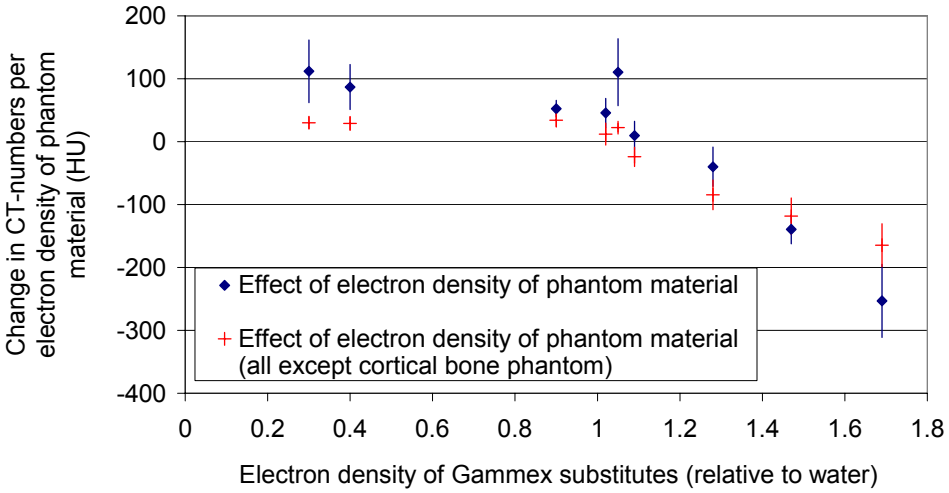

Figure 73. Change per electron density of the phantom materials is shown as a function of the electron density of the substitutes. The blue points represent the change calculated by taking all results from different phantom materials into account. The red points represent the calculated change when the results of the cortical bone phantom are discarded.

In another test, the phantoms were simulated with water as an insert. The effect of phantom material on the CT number of water is presented in Table 10. From the results, it is clear that value calculated by assuming a cortical bone phantom is very far from the other data points. The deviation of the calculated CT-numbers from the expected value (0) decreases by applying BHC.

Table 10. Effect of phantom material on CT-number of water.

phantom material	e-density of (relative to water)	CT-number (HU) without BHC	CT-number (HU) with BHC
AIR	0.00	52±16	3±16
water	1.00	20±90	6±90
RW3	1.01	14±104	-1±104
Muscle	1.02	23±115	9±116
PMMA	1.15	30±105	18±105
CB	1.69	191±600	183±622

4.8. CT calibration relations

In total, 8 calibration relations are calculated. The parameters defining the calibrations are listed in Table 4. The calibrations were based on CT-simulations to study the effect of the different CT-parameters on the relation.

The investigated calibrations were for the standard phantom, ±10 kV in the voltage settings, PMMA phantom of 30 cm diameter, substitutes scanned without a phantom (in air) and H-materials as phantom inserts. Finally two worst case scenarios for the soft-tissue region (from -100 until 120 HU) were assumed.

The simulations for the standard phantom settings were set as the reference of the comparison. The standard settings are the 110 kV photon beam which is incident on a 16 cm phantom of PMMA with Gammex inserts. The results of the simulation are shown in Table 18.

The CT-numbers of each substitute (i) at the voltages 100 (HU_i^{100}) and 120 kV (HU_i^{120}) were calculated from the simulated 110 kV using equations (3.23). The value of $(\Delta HU/\Delta U)_i$ is shown in Figure 69 for each substitute (i).

Changing the voltage by ±10 kV mainly affects the bone-like substitutes, therefore, the CT-calibration relation is unchanged for 100, 110 and 120 kV for the region of HU<0.
The resulting calibrations agree well with the measured data points for Gammex and tissue samples which were measured at 120 kV (see Figure 74).

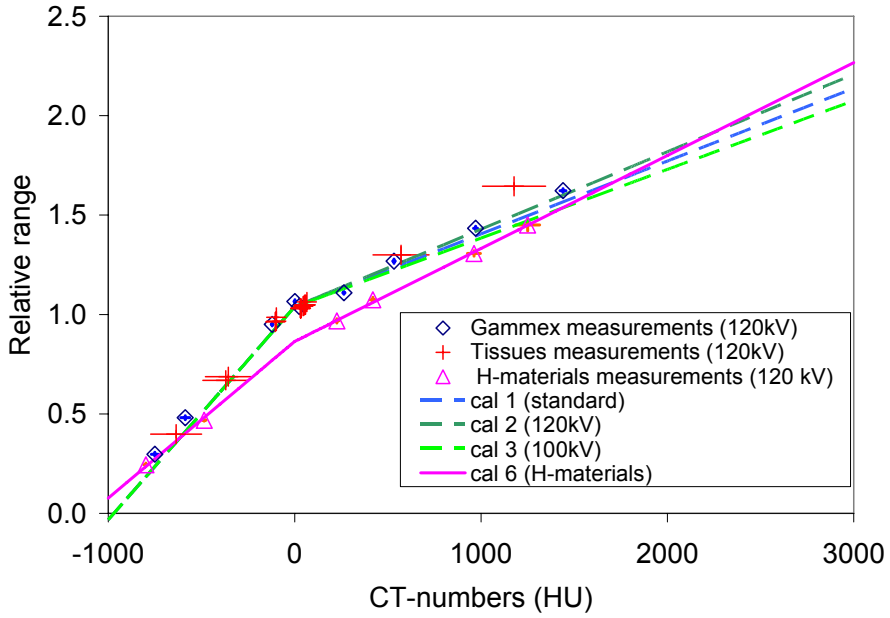

Figure 74. Calibration curves derived from simulated CT-numbers of Gammex substitutes for different voltage settings in comparison to measurements in Gammex substitutes and animal tissues. The calibration relation based on measurements in H-materials and the actual measured values are also shown for comparison. The calibrations are parameterized in Table 11.

The CT-numbers of Gammex substitutes in a PMMA phantom of 30 cm diameter (HU_i^{30cm}) were calculated from the values of the standard simulation (HU_i^{16cm}) using equation (3.24). Here, the value of $(\Delta HU/\Delta diameter)_i$ is shown in Figure 71.

The simulations of the substitutes in air and the simulations of the H-materials were also considered for studying the consequence of these settings on the CT-calibrations.

Finally, the worst case scenarios for the soft-tissue region (-100 – 120 HU) were calculated. In the first case, soft tissues were treated like fat and the relative range of all the tissues between -100 and 120 HU was set to 0.93. In the second case, soft tissues were treated like low density bone and the relative range was set to 1.08 for all the tissues between -100 and 120 HU. 0.93 and 1.08 are the values of the relative range at -100 HU and 120 HU as calculated from the standard calibration.

The remaining regions (less than -100 HU and more than 120 HU) were treated the same as the standard calibration

Calibrations 1-6 can be written as:

$$Cal^k = \begin{cases} m_1^k \times HU + b^k & -1000 < HU \le 0 \\ m_2^k \times HU + b^k & HU > 0 \end{cases}$$

Calibrations 7 and 8 can be written as:

$$Cal^k = \begin{cases} m_1^k \times HU + b^1 & -1000 \le HU < -100 \\ b^k & -100 \le HU \le 120 \\ m_2^k \times HU + b^1 & 120 < HU \end{cases}$$

The values m_1^k, m_2^k and b^k are given in Table 11.

Table 11. Fit parameters for the calibration relations 1-8.

k	Cal^k	m_1^k	m_2^k	b^k
1	cal 1 (standard)	1.07E-03	3.67E-04	1.04E+00
2	cal 2 (120 kV)	1.07E-03	3.90E-04	1.04E+00
3	cal 3 (100 kV)	1.07E-03	3.46E-04	1.04E+00
4	cal 4 (30 cm phantom)	1.22E-03	4.16E-04	1.02E+00
5	cal 5 (air)	1.03E-03	3.17E-04	1.06E+00
6	cal 6 (H-materials)	7.88E-04	4.68E-04	8.64E-01
7	cal 7 (standard - soft tissues)	1.07E-03	3.67E-04	9.31E-01
8	cal 8 (standard + soft tissues)	1.07E-03	3.67E-04	1.08E+00

The calibrations are shown in Figure 75 and in Figure 76 for the soft tissue region.

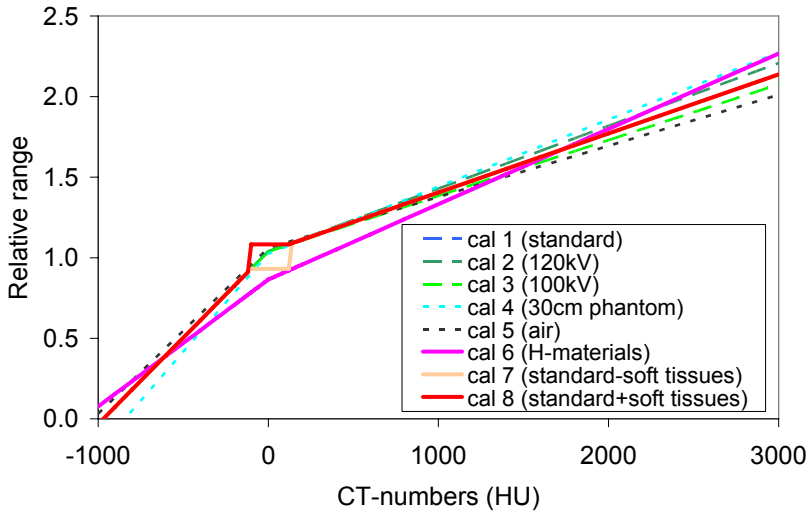

Figure 75. Calibration curves derived from simulated CT-numbers. The legends refer to the index of the calibration and its main characteristic (see Table 11).

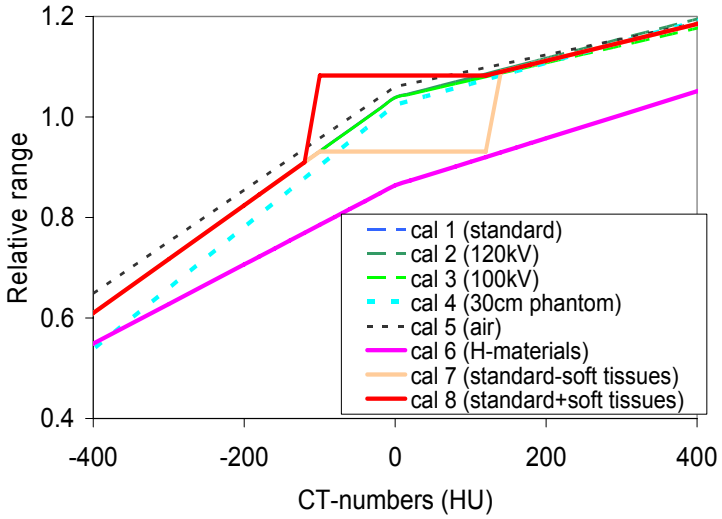

Figure 76. Close-up on Figure 75 for the soft tissue region.

4.9. Effect of CT calibrations on range calculation

To study the effect of the calibrations on the WEPL, CT data from one patient was used. The accumulated WEPL along the beam path was calculated by adding up the contributions from the pixels in the beam path starting from the entrance window (pixel 256 for the field coming from the left side) as seen in Figure 77.

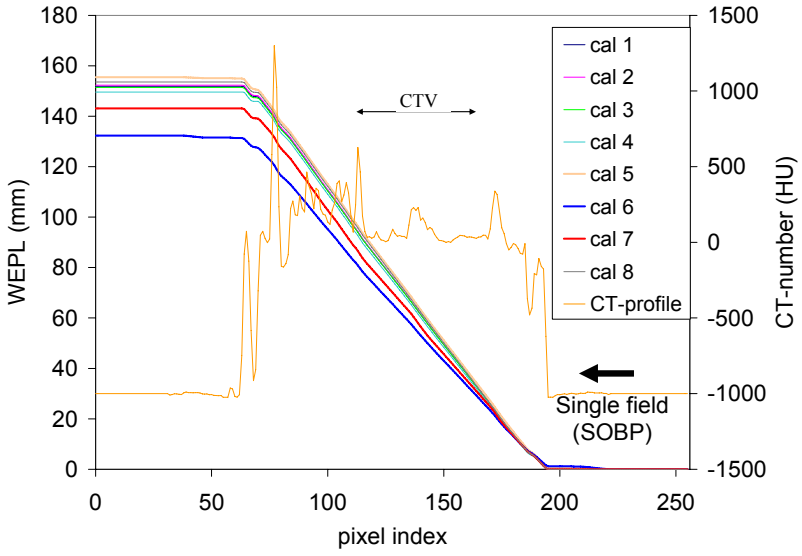

Figure 77. WEPL due to different calibration relations. The WEPL were calculated using the calibration relations in Table 11 and the CT-profile in Figure 36. The profile is also shown here.

The shift in the position of the distal edge of a SOBP of a single field ($\Delta WEPL$) is calculated using equation (3.25). Note that the distal edge for the beam coming from the left is at pixel 110; it is at pixel 160 if the beam is coming from the right. The results of $\Delta WEPL$ are shown in Table 12. From Table 12, calibrations 2, 5 and 8 cause the SOBP to stop before the assigned target margin. As for the calibrations 3, 4, 6 and 7, the SOBP will overshoot the target volume.

Table 12. The difference in position of the distal end of the SOBP due to using the different calibration curves (see Table 11).

Calibration relation	From left $\Delta WEPL$ (mm)	From right $\Delta WEPL$ (mm)
cal 1 (standard)	0.0	0.0
cal 2 (120 kV)	0.2	0.4
cal 3 (100 kV)	-0.2	-0.4
cal 4 (30 cm phantom)	-1.5	-1.3
cal 5 (air)	2.4	2.2
cal 6 (H-materials)	-13.8	-15.2
cal 7 (standard - soft tissues)	-7.7	-6.4
cal 8 (standard + soft tissues)	1.6	1.4

4.10. Effect of calibration relations on dose distributions

The calibrations (see Table 11) were fed into the treatment planning program (TRiP) to calculate the dose distributions. The selected patient suffered from chondrosarcoma at the base of the skull which was situated more to the left side of the brain. The field optimization was performed using the standard calibration for 110 kV, a PMMA phantom of 1 cm diameter and Gammex inserts (cal 1 in Table 11). Single and two-field plans were optimized. One field is characterized by the couch angle -65°, the second by the angle 90°. Only the first field is used in the single-field plan. Both are used in the two-field plan. The arrangement of the field with respect to the patient is shown in Figure 37. The resulting dose distribution is shown in Figure 78 for the standard calibration (cal 1 in Table 11).

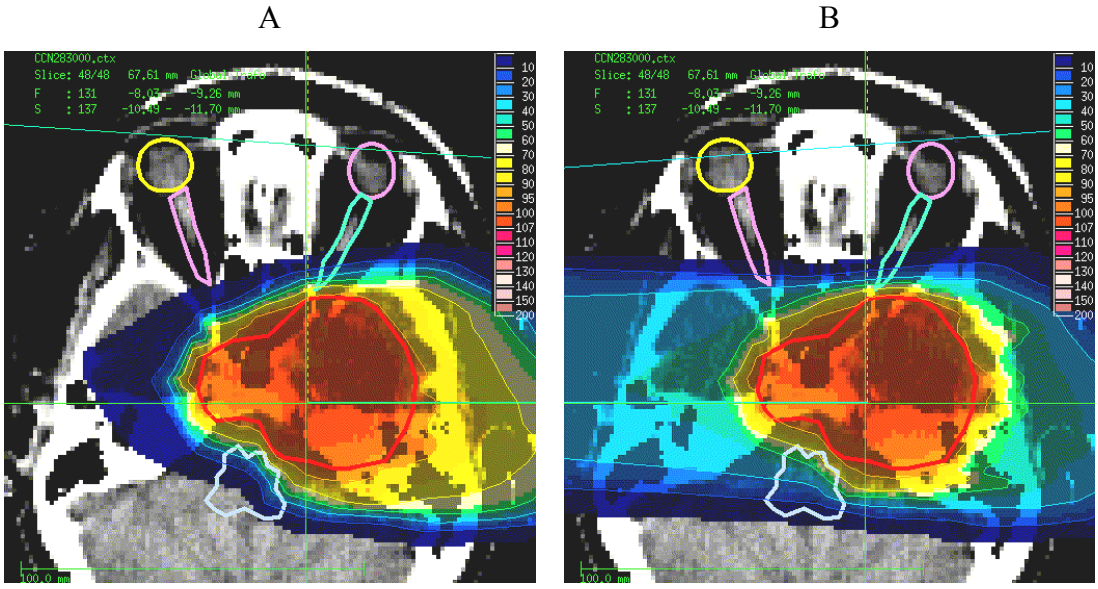

Figure 78. Calculated dose plans for the standard calibration; A: a single-field plan with couch angle of -65°. B: a two-field plan with couch angles of -65° and 90°. The colour wash represents the dose distribution calculated for cal 1 in Table 11. The dose in B is more conformal to the target.

The average dose (D_{mean}) in the specified volume and the percent of volume which is inside the 90% isodose line were calculated for the target volume (CTV) and the organs at risk (brainstem, chiasm and the left optical nerve). The results are shown in Table 13.

Table 13. Mean dose per total volume (D_{mean}) and percent of the volume which receives less than 90% of the total dose (V_{90}) of the target volume (CTV) and the critical organs (brainstem, chiasm and the left optical nerve). The total volume which receives less than 90% of the dos (ml) is also indicated for the target volume. The cells in red indicate critical over dosage in the critical organs; the cells in blue indicate under dosage in the target volume. The cells in dashed lines indicate the improvement by the two-field plan on the dose distribution. The cells in double violet line indicate where the dose distribution of the two-field plan was worse than for the single-field plan.

	CTV			Brainstem		Chiasm		L optic-nerve	
	D_{mean}	ml<V_{90}	%<V_{90}	D_{mean}	%>V_{90}	D_{mean}	%>V_{90}	D_{mean}	%>V_{90}
Single-field plan, couch angle -65°									
cal 1	99.3	0.95	0.9	13.7	0.8	19.1	0.2	22.2	1.2
cal 2	99.2	1.31	1.3	13.5	0.6	19.1	0.2	22.1	1.2
cal 3	99.3	0.66	0.6	13.9	0.9	19.1	0.4	22.4	1.2
cal 4	99.4	0.34	0.3	14.7	1.3	19.3	0.7	23.3	2.3
cal 5	97.4	9.12	8.7	11.6	0.7	18.8	0.3	19.6	0.1
cal 6	99.6	0.76	0.7	20.1	5.2	20.7	2.9	25.2	5.6
cal 7	99.4	1.34	1.3	20.1	5.3	21.6	3.6	26.1	7.0
cal 8	98.3	5.75	5.5	12.2	0.7	18.9	0.2	20.9	0.1
Two-field plan, couch angles -65° and 90°									
cal 1	99.1	0.3	0.3	27.2	0.9	41.8	0.2	23.5	1.9
cal 2	99.0	0.5	0.4	27.1	0.8	41.8	0.2	23.5	1.9
cal 3	99.1	0.2	0.2	27.2	0.9	41.7	0.2	23.5	1.9
cal 4	99.1	0.2	0.2	27.3	0.9	41.4	0.2	23.8	2.5
cal 5	97.6	7.5	7.2	27.0	0.8	43.2	1.4	23.8	0.8
cal 6	98.7	1.9	1.8	29.1	2.1	40.6	0.4	24.5	2.4
cal 7	98.4	2.1	2.0	29.1	2.2	40.9	1.1	24.9	3.6
cal 8	98.2	4.5	4.3	26.9	0.7	42.8	1.0	23.2	0.9

The largest effects are due to choosing calibrations 5 (substitutes scanned in air without phantom) and 8 (soft tissues treated as spongy bone) for dose calculation. The calibrations cause severe under dosage in the target volume. However, calibrations 6 (H-substitutes as phantom inserts) and 7 (soft tissue treated as fat) shift the isodoses into the critical organs which could cause more radiation damage.

Changing the tube voltage by ±10 kV hardly affects the volume inside the 90% isodose line (±0.2%). The effect of using a different diameter of the phantom is more pronounced, but it is within the 0.6% margin for both the CTV and the critical volume.

Choosing a two-field plan improves the dose distribution in general (see Table 13). It usually limits the dose fall-off to the target boundaries. However, it increases the average dose in the critical organs since the organs are now in the entrance region of the field which was not the case in a single-field plan. The two-field plan is not necessarily optimal for all organs at risk. In Table 13, the cells which indicate worst dose distributions with a two-field plan are framed with a double violet line.

The effects of using different calibration relations in a two-field plan are smaller than it was in a single-field plant, but they are still noticeable. This is shown in Figure 79 for the case of the cal 6 line. The graph shows the difference between the doses calculated using cal 6 and the standard calibration (cal 1) for both a single field and a two-field irradiation.

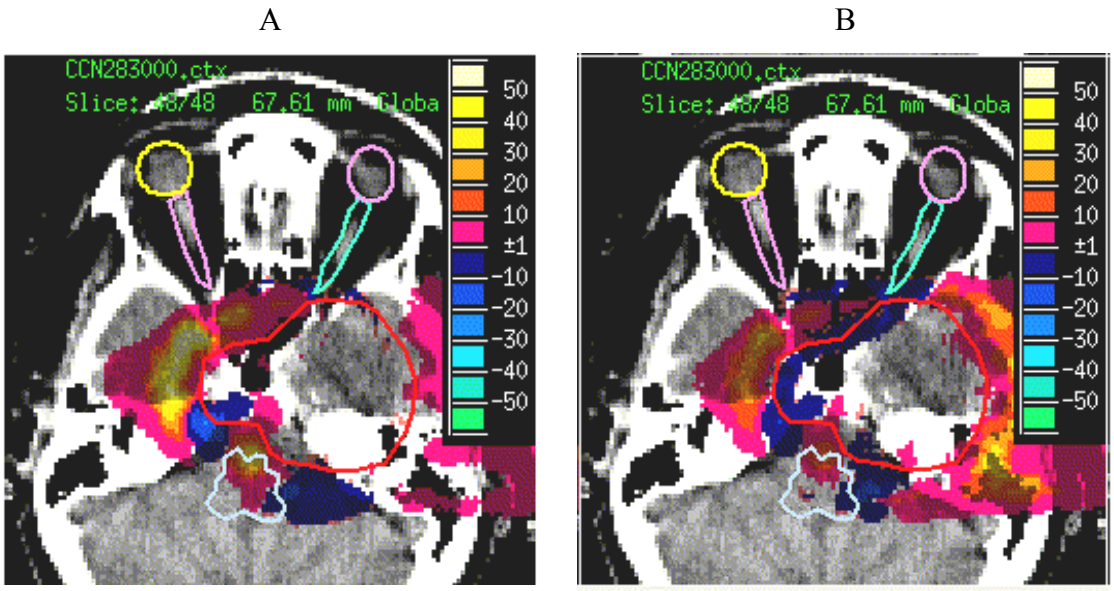

Figure 79. The dose calculated using cal 6 minus the dose calculated using cal 1. A: for a single-field plan with couch angle of -65°. B: for a two-field plan with couch angles of -65° and 90°. The colour wash represents the difference in dose distribution. The colour map shows the change of dose relative to prescribed dose in percents.

5. DISCUSSION

5.1. Effect of CT-parameters on measured CT-numbers

The influence of CT-parameters on the value of measured CT-numbers is different from one scanner to another (see 4.1). In general, the parameters (ordered from most influential on CT-numbers to least) are:

- Voltage settings of the X-ray tube
- Reconstruction kernel
- FOV
- Slice thickness

The voltage setting of the X-ray tube determines the energy of the X-ray photons. As the energy increases the photons are less likely to be absorbed; therefore tube voltage has a direct impact on CT-numbers which increase with decreasing voltage of the X-ray tube. The reconstruction kernel affects the weighting function of the information (see Figure 16). It affects the quality of the image and the level of noise. It also influences the value of CT-numbers but it is expected to have a small effect. Similarly, the FOV is only expected to have a small effect on the value of CT-numbers.

Using different CT-scanners from different vendors results in different CT-numbers, especially for CT-numbers which are greater than zero $(\mathrm{HU} > 0)$. The results shown in Figure 41 indicate that the deviations in CT-numbers reach 75 HU for cortical bone substitute when measured by different CT-scanners with comparable settings. The deviations of the measured CT-numbers are well within the measured uncertainties for lung, fat and soft tissue substitutes $(-1000 \le \mathrm{HU} \le 0)$ when measured with different scanners.

The main reason is that all manufacturers perform an air-water calibration. Hence the scaling of CT-numbers between -1000 and 0 HU is well defined. However, different scaling methods are used by the different manufacturers for the region of $(\mathrm{HU} > 0)$. Fortunately, most of the tissues are similar to water and the different scaling methods only affect the bone-like tissues.

To restrict the deviations due to measurement conditions, it is necessary to perform an air-water calibration regularly. It is also necessary to clearly define the imaging protocols which will be used for treatment planning. If more or other protocols are needed, it is recommended to first perform CT-measurements using a standard phantom and compare the results with values from the other protocols. Though using several calibration relations is uncomfortable, it is recommended to have a relation for each CT-scanner which is used for radiotherapy and for each voltage setting used. The effects of the reconstruction kernel, FOV and slice thickness were negligible for the investigated CT-scanners (less than 5% for cortical bone).

5.2. Substitute materials

The H-materials clearly behave differently than Gammex substitutes (see Figure 42). Previously, it was assumed that the WEPL is higher for the H-materials than for normal tissues. However, Figure 42 shows that the reason is a different behaviour of the CT-numbers.

The composition of the H-materials can explain the different behaviour. In addition to H, C, N O and Ca, H-materials contain significant amounts of Si (10-30%) and Sn (0.06-0.19%) [7]. The density of Si is 2.33 g/cm^3; the density of Sn is 7.31 g/cm^3. They are higher than the densities of any other element used in Gammex substitutes. Moreover, the atomic number is 14 for Si and is 50 for Sn. Therefore, the presence of Si and Sn is expected to cause more photoelectric interactions and larger attenuation of the X-ray photons than in Gammex substitutes.

Measurements of CT-numbers and relative range in real tissue samples clearly show that H-materials do not represent tissues as well as Gammex substitutes (see Figure 45). Therefore, H-materials are not suitable for CT-calibration for treatment planning with heavy ions. In fact, the calibration based on measurements in H-materials (cal 6 in Table 11) caused over dosage in the critical organs and normal tissues when compared to a calibration based on Gammex substitutes (cal 1 in Table 11).

The behaviour of the H-materials was correctly predicted by the simulation (Figure 66). This suggests that the simulation can be used to select unsuitable substitute materials based on their composition.

5.3. CT-spectra in center and off-axis

The K-lines in the Siemens spectra are at higher position than either the simulated or measured spectra of the X-ray tube. The spectra provided by Siemens locate about 5-10% more photons in the characteristic peaks than either simulated or measured spectra of the X-ray tube (Table 8). The difference between the mean energy of the three sources of data at the center of the FOV is within the calculated uncertainty of the mean energy (see Figure 50). However, the Siemens spectra appear to have a higher mean energy than the other sources, possible due to the incorrect allocation of photons to characteristic peaks in Siemens spectra.

In this work, simulated spectra were used to calculate CT-numbers. Had the measured or Siemens spectra been used to calculate CT-numbers, the effect on CT-number would be negligible in the center of the FOV.

It was expected that the mean energy increases with distance from the center of the FOV due to the filters (Figure 51). The change in the mean energy across the FOV is about 10 keV in the Siemens spectra and about 5 keV in the simulation. The measurements indicate that the attenuation across the FOV is stronger than predicted by the simulation. The measured change in the mean energy is 10-15 keV. The spectra from Siemens appear to be in better agreement with the measurement results than the simulated spectra. This suggests that either the distance of the filters to the focal spot is smaller than given by Siemens or that the description of the components in the beam path by Siemens was incomplete.

For the time being, the simulation can only be used to study objects in the center of the FOV where the simulated and measured spectra agree very well. The deviations at the edge of the FOV do not affect the simulation results for small objects. However, 10-15 keV change in the mean energy of the spectra will strongly affect the value of CT-numbers of off-axis objects. Unfortunately, such effects can not be studied using BEAMnrc. See section 5.7 for more details on the limitations of the simulation.

It is possible to estimate the fluence in the FOV by measuring the count-rates as a function of distance from the FOV using the Compton spectrometer. Such measurements can be used to estimate the effective attenuation of the filters and possibly to correct the simulated geometry. Unfortunately, such measurements require a long measurement time and were not possible during this work. The obtained data points (four in total) are not sufficient to estimate the source of deviation between measured and simulated spectra.

5.4. Accuracy of the simulation

The simulation correctly reproduced the behaviour of H-materials compared to Gammex substitutes and the effect of voltage settings of the X-ray tube. The simulation was based on the Emotion CT scanner. Measurements were performed using the Siemens Emotion scanner, the Siemens Sensation4 scanner and the Somatom Plus 4 scanner which was used by Jäkel et al. for measurements of the CT-numbers of the H-materials [7]. Though the scanners used for measurements are different, they are all manufactured by Siemens and are of comparable design-generations. This explains the remarkable result that the average deviation between measured and simulated CT-numbers was 12 ± 5 HU with $\sigma = 53 \pm 5$ HU (see Figure 60).

The difference between the measured and simulated CT-numbers is small and always within the uncertainty of the simulated CT-numbers (Figure 59). The uncertainty of the simulated CT-numbers can rise to 200 HU or more depending on the simulated geometry and number of independent projections used to reconstruct the image. The uncertainty of the simulated CT-numbers also depends on the number of incident photons. Geometries causing large attenuations such as large phantom diameters and cortical bone phantoms show the largest uncertainties (600-1000 HU). In comparison, the uncertainty of simulated CT-numbers for substitutes in air is between 6 and 68 HU. If the attenuation is too large, the photons are absorbed within the phantom and hardly reach the scoring plane. In such cases, it is necessary to simulate more photons in the CT2-part. However, increasing the number of photons in the CT2-part will lead to more recycling of the CT1-PHSP which will increase the uncertainty. The limiting factor is to obtain a sufficient number of photons (about 10^6 per detector element) in order to reconstruct an image with reasonable quality.

In this work, images are reconstructed from few independent projections. Therefore, it is important to have high number of photon counts to generate projections with low statistical fluctuations. Figure 58 shows the effect of statistical noise on the reconstructed attenuation coefficients in a profile through a reconstructed image. Usually 1000 independent views with about 10^{15} photon per view are used for imaging under clinical conditions. To simulate CT-numbers in this work, a maximum of 5 independent views with only 5x108 photons per view were used. When the projections have a low signal to noise ratio, the reconstructed image will have ring artefacts due to the correlation of the noise in the projections (Figure 80).

To lower the uncertainty in the simulated CT-numbers, it is necessary to simulate more photons and more independent projections. Therefore, it is necessary to increase the efficiency of the simulation.

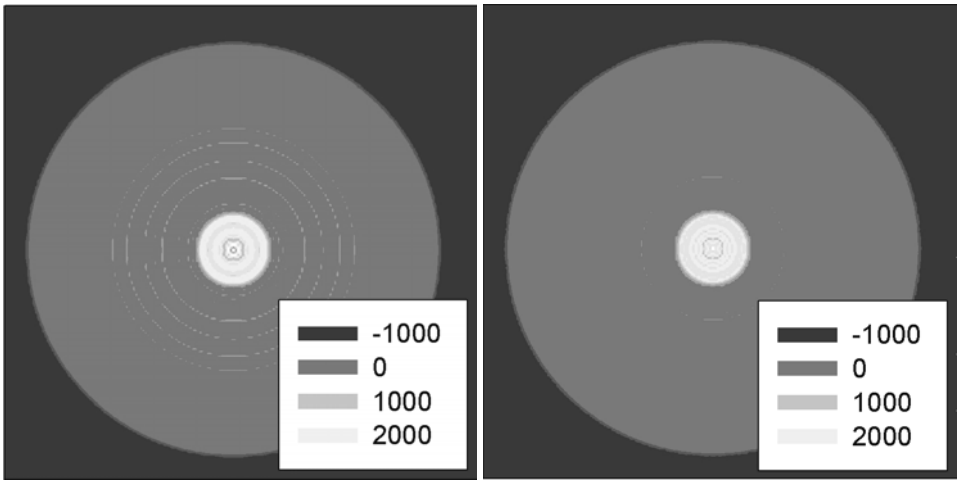

Figure 80. Effect of the number of independent projections on image artefacts. Simulated image of PMMA phantom (16 cm diameter) with cortical bone substitute as insert; the voltage setting is 110 kV and $5x10^8$ photons were simulated. Ring artefacts are visible in the image which is reconstructed using one independent projection (left). The ring artefacts disappear when the image is reconstructed from 5 independent projections (right).

5.5. Efficiency and run-time of the simulation

The efficiency of the simulation is generally poor. It is about 1% for the CT1-part of the simulation and about 5% for the CT2-part.

The low efficiencies are mainly due to the definition of the source and scoring planes in the BEAMnrc code. Scoring planes and surfaces of compound modules can only be defined as squares or circles around the central axis of the incident beam. The source should at least cover the surface of the first compound module. As a result, the beam is delivered to a 50x50 cm^2 in order to cover the FOV of 50 cm diameter. In fact, the region of interest for this work is a single central slice, 0.3 cm thick. This is equivalent to an area of 50x0.3 cm^2. Moreover, losses in the filters cause further decrease in the efficiency of the simulation.

The efficiency of the CT2-part of the simulation is slightly higher than the efficiency of the CT1-part. The beam which is used for CT2-simulations has already been collimated in CT1 (50x1 cm^2 area at 28.5 cm from the focal spot). The loss of photons in the CT2 part is due to further collimation at 94 cm from the focal spot.

One can use variance reduction algorithms (VR) to reduce the run-time needed for simulating large numbers of photons. However, using VR only results more photons per PHSP files but the photons remain highly correlated. After all, the statistical uncertainties are not improved by applying VR. Hence, variance reduction was not evaluated further in this work.

To overcome statistical noise, a large number of incident photons is used for the CT1-part of the simulation where most of the photons are lost. This leads to long computation times of the CT1-simulations since the run-time of the simulation increases with the number of incident photons. However, once a CT1-PHSP is available, it can be used repeatedly to perform CT2 simulations.

5.6. Simulated setup

The simulation imitates the CT-scanner, phantom and substitutes to the best available knowledge. However, the simulation setup includes a few approximations such as assuming that the X-ray tube is a point source to shorten the run-time of the simulation. Other approximations are the energy response of the detector, scatter and beam hardening corrections.

The beam profile due to the point-like X-ray source closely resembles the profiles obtained by the MC simulation of the X-ray tube (seen in Figure 53). However, the approximation is only valid for the central slice (along the slice-plane) and can not represent the beam profile along the Z-direction of the CT. However, this is not important since only the central slices are of importance to this work.

In general, the energy response of the detectors mostly affects the photons with energy less than 52 kV (the K-edge of Gd). The effect of the detector response on the spectrum for 110 kV tube voltage is shown in Figure 81. Detector response has a small effect on the projections. The effect is only noticeable in the central detector elements.

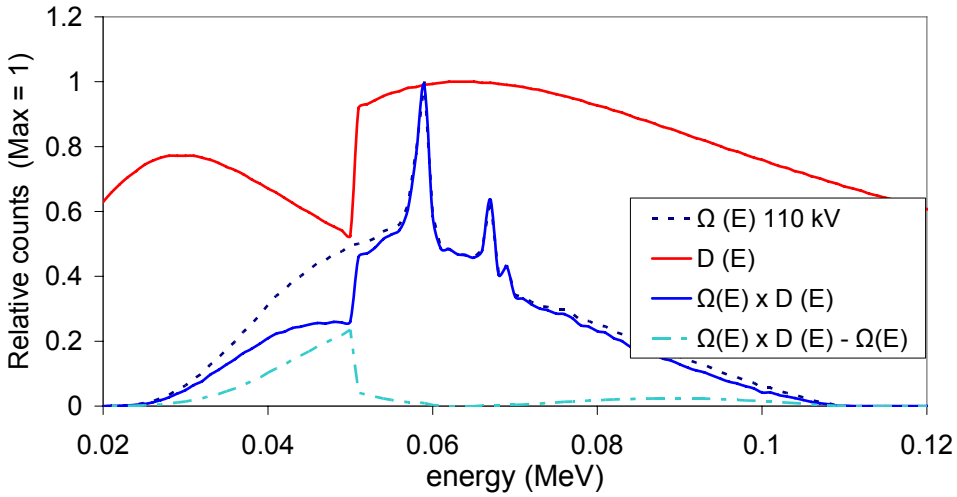

Figure 81. Effect of detector response on the spectral distribution of 110 kV photons. The detector response ($\Omega(E)$) and the spectrum ($\Omega(E)$) are both normalized so that the maximum is 100%. The effect of the detector response is estimated by the multiplication of $\Omega(E)$ times $D(E)$. The difference between the spectrum and the $D(E)$ weighted spectrum is shown as ($\Omega \times D - \Omega$).

The projections are calculated as the signal of the object relative to the signal of air ($-\ln(I / I_0)$). Any effect of the response on the native signal (signal calculated without taking detector response into account) will be reduced by calculating the relative signal (projections). An effect of the energy response of the detectors on the projections is only observed if the phantom causes strong beam hardening i.e. changes the spectral distribution of the photons. The maximum shift in the mean energy of the spectral distribution due to the presence of the phantom and substitutes at the center of the FOV is 10 kV. Therefore, only a small effect of the detector response is expected since the change to the energy spectrum is small. The phantom is cylindrical and the attenuation is strongest in the center of the FOV. Therefore, the shift in the mean energy of the spectral distribution due of the phantom decreases with the distance from the center. As a result, the effect of detector response on the projections decreases with the distance from the center of the FOV.

The influence of detector response on CT-numbers is negligible and can be disregarded in future simulations.

The change of the signal due to applying scatter corrections is shown in Figure 54. The shape of the scatter signal is similar to what is measured and predicted by Ay and Zaidi [63]. In their work, they measured and simulated the scatter signal. In this work, scatter was calculated by assuming perfect collimation by the anti-scatter grid.

Scatter-1 pattern of scatter corrections were applied to all simulation results. It is time consuming and many photon counts are lost. However, without the scatter corrections, the signal is more noisy and the value of CT-numbers is underestimated.

The applied beam hardening corrections algorithm (BHC) assumes that all media interact with X-ray is in the same way as water. This is a good approximation for most tissue types but not for bone. The effect of phantom material on the CT number of water is presented in Table 10. The deviation of the simulated CT-numbers from the expected value (0 HU) decreases by applying BHC. The difference between corrected and uncorrected CT-numbers of water in water, PMMA, muscle, RW3 and cortical bone phantoms was less than 15 HU. However, the corrections were insufficient when a cortical bone phantom is used. On the other hand, when air was used as phantom material, the CT-number was reduced from 53 to 3 HU by applying BHC.

The attenuation of photons increases as the diameter of the phantom increases and so does the beam hardening. Therefore, BHC was also applied to simulations of different diameters of the PMMA phantom. Though the applied BHC was only water based, it is sufficient to deal with the different phantom sizes especially as the phantom is made of PMMA.

For the scope of this work only water based BHC were applied. This was sufficient for most simulation purposes. A better approach is to implement a weighted BHC (see [62] for more information). However, this is only possible if water-like media and bone-like media are distinguishable at the level of projections. This could be achieved by normalizing the simulated projection data with measured projection data for known geometries. Unfortunately, measured projection data (raw data) is considered classified information.

Simulated CT-numbers (without BHC) are compared to CT-numbers of a corrected image of Gammex substitute materials in the standard 16 cm diameter PMMA phantom. In Figure 57, the maximum difference between the results is 17 HU which is well within the uncertainty of simulation (about 80-200 HU). The uncertainty in the calculated CT-numbers is larger than the corrections from the BHC algorithm.

Furthermore, BHC is a post processing correction which is applied to the simulated projections and does not increase the calculation time. Therefore, it is recommended to implement at least a water-based BHC or even a weighted BHC in future simulations.

5.7. Limitations of the MC code

The simulation can only be used to study circular symmetric bodies in the center of the FOV. The reason is that only a small number of projections are used to reconstruct an image. The simulation of oval, rectangular or asymmetric objects could not be performed at this stage. The

simulation of objects in off-axis positions is not possible either. Such geometrical arrangements require a sufficiently large number of views to construct an image (more than 5). The limitations on investigating asymmetric geometries are the low efficiency of the simulation and the limitations of the BEAMnrc code which is used to calculate the PHSP files.

BEAM is a flexible open-source code. It can model complex components but since it was designed to facilitate the simulation of radiotherapy machines, it has a few drawbacks when used to simulate CT-scanners.

- The code can only model compound modules that are perpendicular to the source axis (z-axis) and centred on it. Simulating off axis arrangements is a problematic issue as the default settings of the various compound models have to be modified and verified for such purposes.
- The scoring planes (simulation results) can only be perpendicular to the z-axis. Many scoring planes can be used within a single simulation but they can only be positioned after a compound module
- There is a variety of predefined source routines and the code is also capable of inheriting a pre-calculated phase space file as input to any part of the simulations. However the phase space file can only be used as input when it is perpendicular to the z-axis. Phase-space files from angles other than 0° can not be immediately used. The alternative is the SRCXYZ routine which helps generate a similar particle distribution. However, it can not resemble the energy distribution across the FOV due to the filters.
- The code has the ability to restart runs from the Phase space file if the input number of particles is larger than the number in phase-space file. However, the simulated particles are not totally independent and correlation between the events is visible especially if the file is recycled more often.
- The size of the phase-space files is a limiting factor. It is estimated that 1 million particles require 28 MB of disk space. The generation of smooth projections over a field of view of 50 cm diameter and 3 mm slice thickness requires $5x10^8$ particles and the sizes become about 700 MB. More important is the size of the input phase-space file after the filters and collimators. To avoid correlation, 10^{10} particles were used (about 2.8 GB).
- To correctly allocate and trace the particles at the boundaries of different compound modules, the code is designed with “boundary buffers” between the different compound models. The default thickness of buffers is reasonable for accelerators but might fail for smaller geometries and energies. The “boundary buffer” technique has also been defined between the different layers of a single compound module similar to pyramids. The default value is at least 0.01 cm. The density of the material of filters of the multi-layered compound module had to be redesigned to account for the extra gaps between the different layers. The result is that the electron density of the layers was also increased by 10%. This leads to a higher probability of Compton scattering which causes more photon dissipation in the filters. This could partially account for the very large loss of photons in the CT1 part of the simulation.
- The use of ECUT, AE and ESAVE can all affect the run-time of the simulations. The parameters strongly affect the electron energy fluence. Therefore, if the energy spectra are of importance (similar to our case here), it is necessary to use small values and therefore long calculation times.

Another problem is obtaining adequate and detailed information about the simulated machine; manufacturers are generally reluctant to provide such information because of their obvious commercial value.

5.8. Simulated effects

5.8.1. Filters

The effect of filters on the mean energy and fluence of the X-ray spectrum was investigated (see Figure 63 and Figure 64). The filters focus the beam to the central part of the FOV. When patients are scanned, they are usually positioned in the center of the FOV, where most of the mass of the patients is localized. Therefore it is important to have a high fluence of photons in the center of the FOV. The mass decreases with the distance from the center of the FOV. Hence, less attenuation is expected and less fluence is needed there. The mean energy of the incident photons increased with the distance from the center of the FOV. This is required to reduce the dose to the parts of the patient which are in the outer parts of the FOV.

The measurement of the spectral distributions off axis (see Figure 51) shows that the simulation predicts less attenuation than measured using the Compton spectrometer. The number of measurement points (4 in total) was too small to estimate the attenuation pattern and deduce the source of underestimation.

The effect of filters is expected to be stronger for large objects or for objects at the boundaries of the FOV. In this work, only cylindrically symmetric objects at the center of the FOV are simulated. Therefore, the effect of filters on simulated CT-numbers is small. It can be neglected for small phantom sizes in the center of the FOV.

5.8.2. Voltage settings of the X-ray tube

CT-numbers of bone like substitutes increase with decreasing energy of the spectrum. The reason is that the possibility of photoelectric interactions increases with decreasing energy of the photons.

The absorption in air is very small. Therefore, the effect of choosing different settings of the kV tube do not affect the signal when only air is in the FOV (I_0). On the other hand, absorption in phantom and substitutes increases when the voltage decreases. Since projections are calculated as the signals relative to I_0, the projections of phantom and substitutes increase with decreasing voltage and higher CT-numbers are expected (see Figure 68 and Figure 69).

The effect of voltage change on CT-numbers is only visible in bone substitutes. This is probably due to the fact that the possibility of photoelectric interactions is proportional to $(Z/E)^3$. For, bony tissues, Z=13.8. Z equals 7.5 for soft tissues and 7.4 for water [23]. CT-numbers are attenuation coefficients relative to water, only bone like tissues will show strong variations in CT-number with different voltages. Measurements confirm that only bone substitutes are affected by changes of the voltage settings of the X-ray tube (Figure 40).

The simulation was also used to estimate the effect of ±10 kV variation of the voltage settings of the Siemens Emotion CT scanner using equation (3.23). This is important since the air-water calibration of the Siemens Emotion CT-scanner is maintained by changing the voltage of the X-ray tube. The interface of the scanner shows only 80, 110 or 130 kV which are the nominal voltages of the scanner. The exact voltage settings can be different by up to 10 kV from the nominal voltages without notifying the user. The exact voltage settings change every time the CT is calibrated. Although the information is kept in a log-file, it is only accessible from the service interface and physicians are not entitled to the information.

It is important to know the value of the voltage settings. The voltage of the X-ray tube systematically affects CT-numbers. However, in the case of the Emotion CT-scanner, it might change from day to day and the effect can be considered as an added uncertainty. The effect of voltage variation is small. This suggests that the Siemens Emotion CT scanner can be used for radiotherapy treatment planning.

5.8.3. Phantom size

CT-numbers decrease with increasing diameter of the phantom due to the increased beam hardening. The beam hardening correction applied in the scope of this work treats all materials like water. It should, however, be able to detect the effect of different sizes of the PMMA phantom. The effect of phantom size on the value of CT-numbers is shown in Figure 70 and Figure 71. Phantom size affects the CT-numbers of all substitutes.

The size of the standard phantom is 16 cm diameter. It was designed to simulate the attenuation in the head of the patients since more than 90% of the patients treated with Carbon ion radiotherapy at GSI were treated for head and neck tumours. The commercially available calibration phantoms are usually larger. For example, the diameter of the Gammex-RMI phantoms for CT-calibration is 33 cm diameter [28][30].

The effect of phantom size on CT-calibration was recognized in earlier works [5] [13] [14] [64]. The results simulated in this work agree with the results in the literature for bone substitutes. For example, Schaffner and Pedroni used two phantoms with diameters of 15 and 30 cm to measure CT-numbers [14]. They measured a 5% deviation of CT-numbers of a bone substitute (HB/SR4) due to the different phantom sizes [14]. However, their values were reported in scaled HU i.e. CT-number plus 1000 HU; in the regular Hounsfield scale, the change in CT-number due to 15 cm difference in the diameter of the phantom is -5.9 HU/cm. In this work, the CB250 Gammex substitute (e-density is 1.47) is comparable to the HB/SR4 substitute (e-density is 1.39) [5]. The respective change in the CT-number of CB 250 is simulated as –5.6 HU/cm (see Figure 71). This suggests that the simulation results are accurate for bone substitutes.

Minohara et al. [5] and Schaffner and Pedroni [14] measured the change of CT-numbers in bone and soft tissue substitutes. The effect of phantom size was only visible for bone substitutes [5] [14]. However, in this work, it was found that phantom size also affects the simulated CT-numbers lung substitutes (see Figure 71). This behaviour for lung substitutes is significant in the results of the 28 and 32 cm phantom diameters. It could result from insufficient statistics. The uncertainty of the simulated CT-number is almost 100% for the substitutes in a phantom of 32 cm diameters even when $3x10^9$ incident photons are used.

5.8.4. Phantom material

CT-numbers decrease with increasing electron density of the phantom material (see Figure 72). Again, the effect is due to the increasing possibility of photoelectric and Compton interactions.

Compared to water, muscle (e-density is 1.02), RW3 (e-density is 1.01) and PMMA (e-density is 1.15) cause only small deviations in CT-numbers when simulated as phantom materials. They may be used as water equivalent phantoms. The maximum deviation was recorded when air (e-density is 0) and cortical bone (e-density is 1.69) were simulated as phantom materials.

Therefore, neither air nor cortical bone represent the attenuation of most tissue types. Since the purpose of the CT phantom is to resemble the attenuation properties of the body of patients, it is unlikely to ever use cortical bone as a phantom material. However, in the work of Schaffner and Pedroni, measurements of substitutes in air were used to estimate the effect of beam hardening on CT-numbers [14].

Schaffner and Pedroni reported that if the HB/SR4 bone substitute is scanned free in air, the CT numbers is 4% higher as compared to the situation when a 15 cm phantom is used. In a standard Hounsfield scale, the CT number of the HB/SR4 substitute increases by about 70 HU from the value measured by Schneider et al. (783 HU) [6]. The deviation in CT-number due to scanning of the substitute in a 15 cm diameter phantom or in air is indeed about 9% in the regular Hounsfield scale. The corresponding change in CT-number of CB250 which is comparable to the HB/SR4 substitute is 9.6% from the simulation. The simulation results again seem o be accurate for bone substitutes in air.

CT- numbers of bone substitutes in air are higher than the values when a PMMA phantom is simulated (see Figure 73). The main reason is that the X-ray beam will have a smaller mean energy without a phantom than with a phantom because the attenuation in air is negligible. The photons will interact more with the substitutes and the CT-numbers will increases. The uncertainties of the simulated CT-numbers are about 5% for bone substitutes. It turns out that the number of photons registered in the detector elements is 15 times more than the number registered when a water phantom is simulated. Between $5x10^5$ and 10^6 photons should be registered in each detector element in order to achieve less than 5% uncertainty in the simulated CT-numbers. For most simulations in this work, the number of photons per detector element is only about $5x10^4$.

The deviation of the calculated CT-numbers from the expected value (0 HU) decreases by applying BHC. However, the BHC for the cortical bone phantom is clearly insufficient in this case. The uncertainty of the simulated CT-numbers increases with increasing density of the phantom. The reason is that the attenuation in the cortical bone phantom is stronger than in the other phantom materials. The noise in the image is proportional to the square root of the number of photons in the signal which was used to reconstruct the image. The uncertainty of the CT-numbers scales with the noise in the image. Thus, the uncertainty in the CT-numbers of the substitutes in a cortical bone phantom is high while the uncertainty is very small when the substitutes are simulated without a phantom.

The CT-numbers of water when used as an insert to the different phantoms clearly confirm that the simulation results from the cortical bone phantom are inaccurate (Table 10). Another reason to disregard the results of simulations in cortical bone phantom is the unrealistic uncertainties in the simulated CT-numbers. The uncertainties are between 400 and 1000 HU. The main reason is the insufficient number of incident photons as most of the photons were absorbed within the phantom. When a cortical bone phantom is simulated, the number of photons registered in the detector elements is 18 times less than number registered when a water phantom is simulated. Bone phantoms should not be used for CT-calibrations.

5.9. Effect of CT-calibration on range uncertainties

The shift in the position of the distal edge of a SOBP ($\Delta WEPL$) is calculated using equation (3.25) . The results of $\Delta WEPL$ are shown in Table 12 for two fields, each covering the target volume (Figure 36). The deviation between the calculated $\Delta WEPL$ of both fields is due to the

different distribution of CT-numbers on both sides of the patient's head and the different number of pixels transversed by the beams.

The calibrations 2, 5 and 8 cause the SOBP to stop before the assigned margin of the target volume. As for the calibrations 3, 4, 6 and 7, the SOBP overshoots the target volume. These are systematically shifts which should be avoided if possible.

The uncertainty in patient positioning is about 1-2 mm (Karger et al. [65]). The resolution of the voxles in the CT image is estimated as half the diagonal of the voxel. The length of the side of the square voxels in CT-images is about 1 mm; the slice thickness is 3 mm. The resolution of the voxel is 1.7 mm (Jäkel et al. [66]). $\Delta WEPL$ is considered safely negligible if it is less than 2 mm. It is considered critical if it exceeds 2 mm especially if it is a systematic behaviour.

The effects of the calibrations 2 and 3 are only restricted to the bone area. Therefore, their effect was stronger when the beam is applied from the right because there are more bone structures in the beam path on the right side of the patient than on the left (see Figure 77). A ±10 kV change in the voltage settings causes a $\Delta WEPL$ of 0.4 mm, which is negligible. This is probably due to the fact that, there is only a relatively small amount of bone in the human body (less than 20 %). Furthermore, there are different types of bone, distributed between 200- 1800 HU.

A histogram of the CT-data for a patient (see Figure 35) is presented in Figure 82. The CT-numbers corresponding to the structures in the histograms are pointed out. The peak at -1000 HU refers to the air surrounding the patient. The peak at 3050 HU is an artefact because the scale of CT-number is from -1024 to 3071 HU and all the pixels with a CT-number higher than 3071 are set to have the maximum possible CT number.

This suggests that the Siemens Emotion CT scanner can be used for radiotherapy treatment planning despite the fact that the air-water calibration is maintained by changing the voltage of the X-ray tube without notifying the user. The effect of voltage is systematic, but since the Siemens Emotion scanner is calibrated every day, the exact voltages changes from day to day. However, this is by no means an invitation to overlook the dependency of CT-numbers especially for bone on voltage settings of the X-ray tube. Each of the nominal voltage settings of the Emotion scanner should be represented by a separate calibration relation when used for radiotherapy.

While, the effect of phantom size on CT-calibration was measured by Minohara et al. and also by Schaffner and Pedroni using [5][14], neither the voltage of the X-ray tube nor the material of the phantom was noted in either works. Nevertheless, the results are compared with cal 1 and cal 4 in Figure 83.

The simulation results are very close to the calibrations found in literature. The main difference is in the region of HU<0. While simulated CT-numbers suggest that phantom size affects all substitutes materials including lung, only bone substitutes are affected by the change in the phantom diameter as reported in literature.

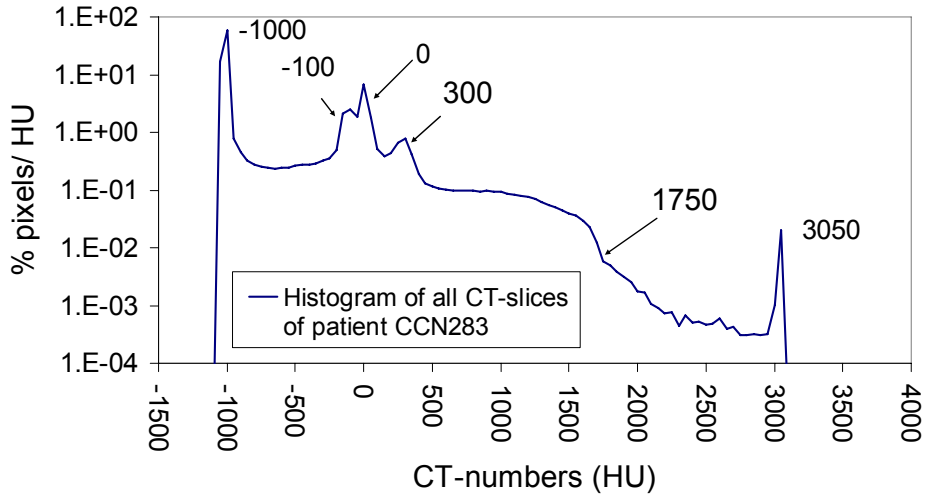

Figure 82. Histogram of CT-data for the patient. The CT-number corresponding to the structures in the histograms are pointed out. The peak at -1000 HU refers to the air surrounding the patient. The peak at 3050 HU is an artefact due to the truncation of the HU scale at 3071 HU. The binning is 50 HU.

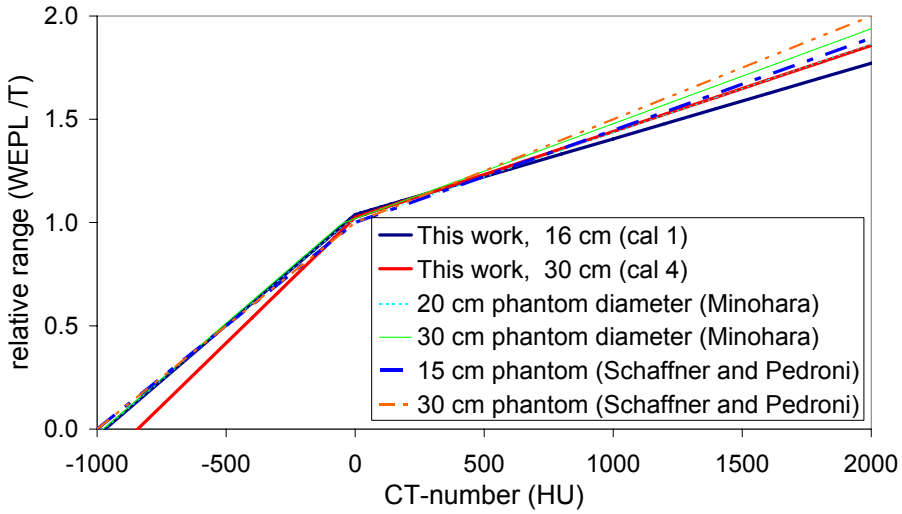

Figure 83. Comparison of calibration relations for ion treatment with literature data for different phantom sizes.

The magnitude of the change in relative range due to change of phantom size can be estimated from the change of the slope of the calibration curves divided by the respective change in the diameter of the phantom ($\Delta slope / \Delta diameter$) which is shown in Table 14. The effect estimated in this work is comparable with results in the literature for CT-numbers larger than zero. The difference in $\Delta slope / \Delta diameter$ is considerably large for the range of CT-numbers below zero. For comparison, the slope of the standard calibration (cal 1) is 3.86E-04 HU^{-1} in the bone part of the calibration and 1.09E-03 HU^{-1} for CT-numbers below zero. A change by 3.57E-06 HU^{-1} cm^{-1} in the slope is equivalent to 9.2% for 10 cm change in phantom diameter.

Quantitatively, the effect of the diameter of PMMA phantom on $\Delta WEPL$ is about -1.4 mm which is still less than the margin of 2 mm and can be considered negligible. The reason is that the difference is considerable only for CT-numbers less than -200 HU. Fortunately, less than 10% of the all the pixels in the CT-image of a patient have a CT-number below the -200 HU limit (Figure 82).

Table 14. Change of slope of the calibration curve due to change of phantom size ($\Delta slope / \Delta diameter$) estimated from results of Minohara et al. [5], Schaffner and Pedroni [14] and the values for cal 1 and cal 4 in Table 11.

	$\Delta slope / \Delta diameter$ (HU^{-1} cm^{-1})	
	CT-number < 0 HU	CT-number > 0 HU
Minohara et al.	1.00E-06	3.21E-06
Schafner and Pedroni	0.00E+00	3.57E-06
This work	1.03E-05	3.57E-06

The effect of the phantom size changes from one CT to the other due to the filters. Therefore, it is recommended that the phantom used for calibration purposes represents the body part of interest to the treatment planning. The effect of size can possibly be calculated for the bone part of the calibration without the need for further measurements using $\Delta slope / \Delta diameter$, provided that the phantom material is water equivalent.

Scanning the substitutes in air is presented by calibration 5 which appears to have a different slope when compared to the standard calibration (cal 1). The effect of the calibrations on $\Delta WEPL$ is about 2.3 mm, which is no longer negligible. Such a calibration does not represent the attenuation of photons in the body well and should not be used for treatment planning. However, it can be used to estimate safety margins similar to the work of Schaffner and Pedroni [14].

The worst case scenarios (calibrations 7 and 8) caused shifts in different directions. The difference between the standard calibration and calibration 8 is larger than the difference between the standard calibration and calibration 7. Therefore, $\Delta WEPL$ due to calibration 8 is larger. The calibration 8 only influences the soft tissue area (-120 to 100 HU), but it causes up to -7 mm shift in the distal edge of SOPB. The reason is that more than 70% of the voxels in a CT-image of a patient are within the affected range (see Figure 82). Special care should therefore be given to this part of the calibration.

Calibration 6, which is based on measurements in H-materials, proved worse than the worst case scenario (cal 8), its effect was more dramatic than calibration 7. Calibration 6 did not only have a different behaviour in the soft tissue region than expected by normal tissues, it underestimated the relative range for almost the entire scale. The $\Delta WEPL$ of -14.5 mm is not surprising. This confirms that H-materials are not suitable substitutes for CT-calibrations. Therefore, substitutes which do not represent tissues (for example H-materials) are not suitable for CT-calibration for ion therapy.

5.10. Effect of CT-calibration on dose calculation

The CT calibration relations were fed into the treatment planning program (TRiP) to calculate the dose distributions. The field optimization was performed using the standard calibration (calibration 1). Single and two-field plans were optimized. The results are shown in Table 13.

The results have all been calculated for a single tumour position and a single patient. Some conclusions can be drawn , however they can not be generalized. The largest effects on the CTV are due to choosing calibrations 5 (substitutes scanned in air without phantom) and 8 (soft tissues treated as spongy bone) for dose calculation. Both calibrations cause the beam to stop before the required distal end of the target volume which results severe under dosage in the

target volume. Calibrations 6 (H-substitutes as phantom inserts) and 7 (soft tissue treated as fat) shift the isodoses into the critical organs which could cause more radiation damage because these calibration cause the SOBP to overshoot the target volume.

Changing the tube voltage by ±10 kV hardly affects the dose distribution. The effect of using a different diameter of the phantom is more pronounced, but it is still negligible.

Two-field plans result in a more homogenous dose distribution than single-field plans. The dose calculated using two-field plans is more conformal to the target volume (see Figure 78). However, the average dose in the critical organs increases when a two-field plan is used because the organs are now in the field of radiation which was not the case in a single-field plan.

The effects of using different calibration relations in a two-field plan are generally smaller than it was in a single-field plant. The reason is that the imperfect dose distribution of one field will be compensated by the other field. Yet, the effects of calibrations 5 and 8 still cause around 5% under dosage in the CTV. The reason is that the ions do not cover the target volume in the single fields and could not do so in a two-field plan. Hence, it could be concluded that if the calibration relation underestimates the range, its effect on the dose calculation decreases when more fields are planned. The effect of the calibrations which overestimate the range is not immensely improved by choosing a more fields in a plan.

6. CONCLUSION

This work has presented a method for calculating the CT-numbers from MC simulations. This is the first study of the accuracy of CT-numbers based on MC simulations of a CT-scanner. Previous studies were based on measurement results in known substitutes. The average deviation between measured and simulated CT-numbers was 12 ± 5 HU with $\sigma = 53 \pm 5$ HU (see Figure 60). This is a remarkable result, particularly since the uncertainty of simulated CT-numbers can rise to 200 HU or more depending on the simulation setup.

The method presented here could therefore be used to estimate the effect of different parameters on CT-numbers. For example, measurements performed in this work indicate that the voltage of the X-ray tube has a strong effect on CT-numbers of bones. The effect was correctly reproduced by the simulation. This method could also be used to investigate the suitability of substitutes to perform CT-calibrations. For example, H-materials were found unsuitable to perform CT-calibrations, whereas Gammex substitutes closely resemble the behaviour of body tissues [7]. This was confirmed by measurements of CT-numbers and ion ranges in real tissues. Again, the simulation correctly predicted the CT-numbers of H-material and distinguished them from Gammex substitutes.

The results of the simulation were used to estimate the effects of different phantom materials, phantom size and voltage setting of the X-ray tube on the value of CT-numbers. The simulated results were presented as calibration relations and were used for rand and dose calculation for a typical patient with a tumour at the skull base. The results show that:

- Substitutes which do not represent tissues (e.g. H-materials) are not suitable for CT-calibration especially for ion therapy
- Changing the settings of the X-ray tube by ±10 kV causes a small effect on the calculated dose because it only affects the bone-part of the calibration and there is only a small percentage of bone in the human body.
- Variations in the CT-numbers of soft-tissues (-100-120 HU) have the strongest effect on dose, since soft tissues represent about 70% of the total volume in the patient. This might be even more important in other tumour locations e.g. pelvic tumours.
- The calibration calculated when the substitutes are scanned without a phantom (in air) has a totally different slope from the standard calibration. It should not be used for treatment planning in ion therapy.
- Phantom size has an effect on the CT-calibration and the subsequent dose calculation. The size of the phantom should represent the body part in question.

The method presented here can correctly estimate CT-numbers for cylindrical objects in the center of the FOV. However, oval, rectangular or asymmetric objects which cannot be approximated by a few independent views cannot be simulated, yet.

7. OUTLOOK

7.1. Suggested improvements to the simulation

Reading raw data and applying weighted BHC at the projections level
Raw data of CT measurements are classified information. The raw data format was available from Siemens. However, it is not trivial to extract the information. Obtaining data on the projection level can be used to normalize the simulation results and implement weighted BHC.

Calculating the shape of the filters by measuring spectra at different angles off axis
It is possible to calculate the total attenuation due to the filters by measuring the spectral distribution at many points in the FOV. This has been applied to estimate the shape of the filters on the Toshiba scanner by W. Stiller and B. Ackermann [67]. The same method can be used to estimate the source of error in the simulation of the filters as seen in Figure 51.

Asymmetric phantoms and multi-angular projections
A small number of independent projections (maximum five) are used to reconstruct an image. Therefore, the simulation can only be used to study circularly symmetric bodies in the center of the FOV. It is important to modify the method in order to simulate oval, rectangular or asymmetric objects. There are two issues here; the efficiency of the simulation and the limitations of the BEAMnrc code.

Currently, the efficiency of the simulation is low. It is important to improve the efficiency of the simulation because more projections are needed and therefore more time will be consumed by simulation. it is possible to define a new source profile which describes the fluence of particles Using the beam profiles from CT1-PHSP. Introducing the energy attenuation due to the filters can be performed by assigning beam angles to a Look-up-table which is created from full simulation of the filters or spectra measurements. The new source profile could also be used with modified SRCXYZ source code to model radiation from different angles using the description of a phase space fie. The implementation of such approaches in ARC therapy by Chow 2003 [68] and IMRT by Ma [69] and [70] has been successful for dose calculation purposes.

BEAM is a flexible open-source code. It can model complex components but since it was designed to facilitate the simulation of radiotherapy machine, it has a few drawbacks when used to simulate CT-scanners. The limitations of the BEAMnrc code (see section 5.7) can not be easily overcome. They require modification of available compound modules or the introduction of new ones. Another approach is building the CT2 part of the simulation in other MC codes. For example EGSnrc offers the chance of introducing asymmetric geometry better than BEAMnrc at the cost of longer simulation times. The Monte Carlo code MCNP has been used efficiently by Ay and Zaidi to simulate CT-scanners for imaging purposes [63].

7.2. Metal artefacts

Due to the strong absorption in metals, the CT-number of metals exceeds 3000 HU. The cut of for large CT-numbers is applied by the software of most CT-scanners. Therefore, range calculation in metals can not be based on measured CT-numbers for patients with metal implants. In ion therapy, metal artefacts in the CT-image can lead to excluding patients from

the therapy. The effect of metals is a dramatic shift in the position of the Bragg peak. The relative range of metals is 3-10, depending on the type of the metal investigated. For comparison, the relative range in cortical bone is 1.7. In order to overcome the problem of metal implants in treatment planning, the correct range of ions is usually assigned directly to the CT-data. Ion ranges in metals have been experimentally measured for gold, stainless-steel and Titanium [71]. However, it is not always possible to define the geometric boundaries of the metallic objects from the image because of the streak artefacts.

There were also attempts to use an extended CT-calibration for metals [72]. However, there remains the danger of miss assignment of the electron density of the metal due to shortcomings in the TPS [73]. In the study by Coolens and Childs, it was recommended to use such calibrations only to identify the type of metal and assign the appropriate electron density manually [72].

The effect metal artefacts on CT-numbers could be systematically investigated using the simulation method suggested in this work, provided that sufficient photon numbers are used.

7.3. Assigning data in MC-based treatment planning

CT data is the only quantitative information for input data on patients or phantoms. In MC-based treatment planning, it is necessary to assign more data to the matrix to correctly perform MC dose calculations. For example, water and soft tissues have comparable CT-numbers, but water has a slightly higher mass energy absorption coefficient than soft tissues [13]. The art of assigning data based on CT-numbers for MC calculations was initiated by Du Plessis et al. [75] and Schneider et al. [77]. The miss assignment of material data can cause larger dose errors than only assigning mass or electron density information. Verhaegen and Devic 2005 [13] proved that the miss assignment of material information in DOSEXYZnrc leads to 10% dose errors in megavolt photons rising to 40% error for kilovolt photons. The effect was estimated to be 30% for 18 MeV electrons. The effect of miss assigning electron density of metals was investigated using the Helax TMS pencil beam algorithm [73].

The miss assignment increases with the inherited uncertainties of CT-numbers due to the material of the CT phantom which has been used for CT-calibration and the voltage settings of the X-ray tube [13]. The effects of these parameters have been investigated in this work and could be used to deduce the correct CT-numbers corresponding to the investigated geometry.

REFERENCE

[1] Kraft G 2000 Tumor therapy with heavy charged particles *Pros. Part. Nucl. Phys.* **45** S473-S544

[2] Hsieh J Computed tomography: principles, design, artefacts, and recent advances (Bellingham, Washington, 2002)

[3] Mustafa A A Jackson D F 1983 The relation between X-ray CT numbers and charged particle stopping powers and its significance for radiotherapy treatment planning *Phys. Med. Biol.* **28** 169-176

[4] Chen G T Y Singh R P Castro J R Lyman J T Quivey J M 1979 Treatment planning for heavy ion therapy *Int. J. Radiat. Oncol. Biol.*, Phys. **5** 1809-1819

[5] Minohara S Kanai T Endo M Kawachi K 1993 Effects of object size on a function to convert X-ray CT numbers into the water equivalent path length of charged particle beam **In Proceedings** *Third Workshop on Physical and Biological Research with heavy ions*, Chiba 14-15

[6] Schneider U Pedroni E Lomax A 1996 The calibration of CT Hounsfield units for radiotherapy treatment planning *Phys. Med. Biol.* **41** 111-124

[7] Jäkel O Jacob C Schardt D Karger C Hartmann G H 2001 Relation between carbon ion ranges and X-ray CT numbers *Med. Phys.* **28,** 4 701-703

[8] Kanematsu N Matsufuji N Kohno R Minohara S Kanai T 2003 A CT calibration method based on the polybinary tissue model for radiotherapy treatment planning *Phys. Med. Biol.* **46** 1053-1064

[9] Cozzi L Foglieta Antonella Buffa Francesca Bieri Sabine 1998 Dosimetric impact of computed tomography calibration on commercial treatment planning systems for external radiation therapy *Radiotherapy and Oncology* **48** 335-338

[10] Kilby W Sage J Rabett V 2002 Tolerance levels for quality assurance of electron density values generated from CT in radiotherapy treatment planning *Phys. Med. Biol.* **47** 1485-1492

[11] Thomas S J 1999 Relative electron density calibration of CT scanners for radiotherapy treatment planning *The British Journal of Radiology* **72** 781-786

[12] Ramm U Damrau M Mose S Manegold K-H Rahl C G Böttcher H-D 2001 Influence of CT contrast agents on dose calculation in a 3D treatment planning system *Phys. Med. Biol.* **46** 2631-2636

[13] Verhaegen F Devic S 2005 Sensitivity study for CT images in Monte Carlo treatment planning *Phys. Med. Biol.* **50** 937-946

[14] Schaffner B Pedroni E 1998 The precision of proton range calculations in proton radiotherapy treatment planning : experimental verification of the radiation between CT-HU and proton stopping power *Phys. Med. Biol.* **42** 1579-1592

[15] Homolka P Gahleitner A Nowotny R 2002 Temperature dependence of HU values for various water equivalent phantom materials *Phys. Med. Biol.* **47** 2917-2923

[16] Attix F H Introduction to Radiological physics and radiation dosimetry (New York, 1986)

[17] GSI website www-aix-old.gsi.de/~bio/MISC/pictures.html

[18] Krämer M Jäkel A Haberer T Kraft G Schardt D Webber U 2000 Treatment planning for heavy ion radiotherapy: physical beam model and dose optimization *Phys. Med. Biol.* **45** 3299-3317

[19] 3D Conformal radiation therapy, a multi introduction to methods and techniques ed Wolfgang Schlagel and Andreas Mahr (Springer, Berlin, 2001)

[20]Leo W R Techniques for nuclear and particle physics experiments: a how to approach (Springer-Verlag, Berlin, 1987)
[21]Jacob C Reichweite CT-Zahl Beziehung von Phantommaterialien und Messungen mit einer neuentwickelten multisegmentierten Ionisationskammer zur Dosisverifikation bei Schwerionenbestrahlung Dissertation for the University of Heidelberg 1997
[22]Kalender W Computed tomography: fundamentals, system technology, image quality, applications (Publicis-MCD-Verl, München 2000)
[23]Dowset D J Kenny P A. and Johnston R E *The physics of diagnostic imaging* (Chapman and Hall Medical, London 1998)
[24]Bushberg et al. *The essential physics of medical imaging* (Lippencott Williams and Wilkins, Philadelphia, USA 2001)
[25]Jackson D F 1982 Chemical effects in X-ray transmission measurements *Nuclear Instruments and Methods* **193** 387-389
[26]Jackson D F Hawkes D J 1980 X-ray attenuation coefficients of elements and mixtures *Physics Reports* **70** 169-233
[27]Kak and M. Slaney Principles of computerized tomography Imaging IEEE press (1988)
[28]Constantinou C Harrington J C DeWerd L A1992 An electron density calibration phantom for CT-based treatment planning computers *Med. Phys.* **19** 325-327
[29]Heismann B J Leppert J Stierstorfer K 2003 Density and atomic number measurements with spectral X-ray attenuation method *Journal of Applied Physics* **94** 2073-2079
[30]Gammex data sheet.
[31]Romanchikova M Monte Carlo Simulation des Röntgenspektrums einer computertomographischen Röntgenröhre Diplomarbeit for The University of Heidelberg 2006
[32]Knoll G F Radiation detection and measurement New York (1999)
[33]Matscheko G Ribberfors R 1987 A Compton scattering spectrometer for determining X-ray photon energy spectra *Phys. Med. Biol.* **32** 577-594
[34]Matscheko G Carlsson G A 1989 Measurements of absolute energy spectra from a clinical CT machine under working conditions using a Compton spectrometer *Phys. Med. Biol.* **34** 209-222
[35]Matscheko G Carlsson G A 1989 Compton spectroscopy in the diagnostic X-ray energy range. I. Spectrometer design *Phys. Med. Biol.* **34** 185-197
[36]Matscheko G Carlsson G A Ribberforst R 1989 Compton spectroscopy in the diagnostic X-ray energy range. II. Effects of scattering material and energy resolution *Phys. Med. Biol.* **34** 199-208
[37]Spectro-X Compton spectrometer Manual
[38]Matscheko G Ribberfors R 1989 A generalised algorithm for spectral reconstruction in Compton spectroscopy with corrections for coherent scattering *Phys. Med. Biol.* **34** 835-841
[39]Germanium detectors: user's manual (Canberra Industries Inc. Meridon USA, 2003)
[40]Bhat M Pattison J Bibbo G Caon M 1998 Diagnostic X-ray spectra: a comparison of spectra generated by different computational methods with a measured spectrum *Med. Phys.* **25** 114-120
[41]Caon M Bibbo G Pattison J Bhat M 1998 The effect on dose to computed tomography phantoms of varying the theoretical X-ray spectrum: a comparison of four diagnostic spectrum calculating codes *Med. Phys.* **25** 1021-1027
[42]Ay M R Shahriari M Sarkar S Zaidi H 2004 Monte Carlo simulation of X-ray spectra in diagnostic radiology and mammography using MCNP4C *Phys. Med. Biol.* **49** 4897-4917
[43]Ay M R Sarkar S Shahriari M Zaidi H 2005 Assessment of different computational models for genration of xray spectra in diagnostic radiology and mammography *Phys. Med. Biol.* **32** 1660-1675

[44]Atherton J V Huda W 1995 CT dose in cylindrical phantoms *Phys. Med. Biol.* **40** 891-911
[45]Jarry G DeMacro J J Beifuss U Cagnon C H 2003 A Monte Carlo-based method to estimate radiation dose from spiral CT : from phantom testing to patient-specific models *Phys. Med. Biol.* **48** 2645-2663
[46]Salvado M Lopez M Morant J J Calzado A 2005 Monte Carlo calculations of radiation dose in CT examination using phantom and patient tomographic models *Radiation Protection Dosimetry* **114** 364-368
[47]Tzedakis A Perisnakis K 2006 The effect of z overscanning on radiation burden of pediatric patients undergoing head CT with multidetector scanners : A Monte Carlo study *Med. Phys.* **33 7** 2472-2478
[48]Rogers D W O 2002 Monte Carlo techniques in Radiotherapy *Med. Phys.* **58** 63-70
[49]Carrier J F Archambault L Beaulieu L Roy R 2004 Validation of GEANT4, an object oriented Monte Carlo toolkit, for simulations in medical physics *Med. Phys.* **31** 484-492
[50]Chibani O Li X A 2001 Monte Carlo dose calculation in homogeneous media and at interfaces: a comparison between GES, EGSnrc, MCNP and measurements *Med. Phys.* **29** 835-847
[51]Verhaegen F Nahum A E Van de Putte S Namito Y 1999 Monte Carlo modelling of radiotherapy kV X-ray units *Phys. Med. Biol.* **44** 1767-1789
[52]Verhaegen F 2002 Evaluation of the EGSnrc Monte Carlo code for interference near high-Z media exposed to kilovolt and ^{60}Co photons *Phys. Med. Biol.* **47** 1691-1705
[53]Kawrakow I 2000 Accurate condensed history Monte Carlo simulation of electron transport. EGSnrc, the new EGS4 version *Med. Phys.* **27** 485-498
[54]Bhat M Pattison J Bibbo G Caon M 1999 Off-axis X-ray spectra: a comparison of Monte Carlo simulated and computed X-ray spectra with measured spectra *Med. Phys.* **26** 303-309
[55]Rogers D W O Faddegon B A Ding G X Ma C M We J Mackie T R 1995 BEAM: A Monte Carlo code to simulate Radiotherapy treatment units *Med. Phys.* **22** 503-524
[56]Kawrakow I 2004 EGSnrc *NPL Workshop March 17-18 2004* www.npl.co.uk/ionrad/training/montecarlo/mc2004/workshop/egsnrc_slides.pdf
[57]Marianno C M Higley K A Palmer T.S. 2000 A comparison between default EGS4 and EGS4 with bound Compton cross sections when scattering occurs in bone and fat *Health Physics* **78** 716-720
[58]Kawrakow I. and Rogers D. W. *The EGSnrc Cod System: Monte Carlo simulation of electron and photon transports* Technical report PRIS-701 National Research Council of Canada Ottowa, Canada (2003)
[59]Namito Y Hirayama H Ban S 1998 Improvements of low-energy photon transport in EGS4 *Radiation Physics and Chemistry* **53** 283-294
[60]Rogers D W O Ma C –M Walters B Ding G X Sheikh-Bagheri D and Zhang G *BEAMnrc Users manual* NRCC report PRIS-0509(A) rev G National Research Council of Canada Ottowa, Canada (2001)
[61]Kachelrieß M Sourbelle K Kalender W 2006 Empirical cupping corrections: a first-order raw data precorrection for cone beam computed tomography *Phys. Med. Biol.* **33** 1269-1274
[62]Kachelrieß M Kalender W 2005 Improving PET/CT attenuation correction with iterative CT beam hardening corrections *Nuclear Science Symposium Conference Record, 2005* IEEE **4** 2005
[63]Ay M R Zaidi H 2005 Development and validation of MCNP4C-based Monte Carlo simulator for fan and cone beam X-ray CT *Phys. Med. Biol.* **50** 4863-3885
[64]Siegel M J Schmidt B Bradley D Suess C Hildebolt C 2004 Radiation dose and image quality in pediatric CT: effect of technical factors and phantom size and shape *Radiology* ***233*** 515-522

[65]Karger C P Jäkel O Debus J Kuhn S Hartmann G H 2001 Three-dimensional accuracy and interfractional reproducibility of patient fixation and positioning using a stereotactic head mask system *IJROBP* **49** 1493-1504
[66]Jäkel O Hartmann G H Karger C P Heeg P Rassow J 2000 quality assurance for treatment planning system in scanned ion beam therapy *Med. Phys.* **27** 1588-1600
[67]Personal contact
[68]Chow J C L Wong E Chen J Z Van Dyk J 2003 Comparison of dose calculation algorithms with Monte Carlo methods for photon arcs *Med. Phys.* **30** 2686-2694
[69]Ma C M Li J S Pawlichi T Jiang S B Deng J Lee M C Koumrin T Luxon M Brian S 2002 A Monte Carlo dose calculation tool for radiotherapy treatment planning *Phys. Med. Biol.* **47** 1671-1690
[70]Ma C M Pawlicki T Jiang S B Li L S Ding J Mok E Kapur A L L Xing A L Ma Boyer 2000 Monte Carlo verification of IMRT dose distributions from commercial treatment planning optimization system *Phys. Med. Biol.* **45** 2483-2495
[71]Jäkel O 2006 Range of ions in metals for use in particle treatment planning *Phys. Med. Biol.* **51** N173-N177
[72]Coolens C Childs P J 2003 Calibration of CT Hounsfield units for radiotherapy treatment planning of patients with metallic hip prostheses: the use of the extended CT-scale *Phys. Med. Biol.* **48** 1591-1603
[73]Roberts R 2001 How accurate is a CT-based dose calculation on a pencil beam TPS for a patient with metallic prosthesis? *Phys. Med. Biol.* **46** N227-N234
[74]Verhaegen F Das I J 2002 Interface dosimetry for kV and MV photon *AAPM Proceedings book* **Proceedings No 13** 268-87
[75]Du Plessis F C P Willemse C A Lötter M G 1998 The indirect use of CT to establish material properties needed for Monte Carlo calculations for dose distributions in patients *Med. Phys.* **25** 1195-201
[76]Sennst D A Kachelriess M Leidercker C Schmidt B Watzke O Kalender W A 2004 An Extensible Software-based Platform for Reconstruction and Evaluation of CT images *Radiographics* **24** (2) 601-613
[77]Schneider W Bortfeld T Schlegel Wolfgang 2000 Calibration of CT numbers and tissue parameters needed for Monte Carlo simulations of clinical dose distributions *Phys. Med. Biol.* **45** 459-478
[78]Andreo P 1991 Monte Carlo techniques in medical radiation physics *Phys. Med. Biol.* **36** 861-920
[79]Geithner O Andreo P Sobolevsky N Hartmann G Jäkel O 2006 Calculation of stopping power ratios for carbon ion dosimetry *Phys. Med. Biol.* **51** 2279-2292
[80]Boone J M Chavez A E 1996 Comparison of X-ray cross sections for diagnostic and therapeutic medical physics *Med. Phys.* **23** 1997-2005
[81]Boone J M Cooper V N Nemzek WR McGahan J P Seibert J A 2000 Monte Carlo assessment of computed tomography dose to tissue adjacent to the scanned volume *Med. Phys.* **27** 2393-2407
[82]Caon M Bibbo G Pattison J 1997 A comparison of radiation dose measured in CT dosimetry phantoms with calculations using EGS4 and voxel-based computational mode *Phys. Med. Biol.* **42** 219-229
[83]Devic S Monroe J I Mutic S Whiting B Williamson J F 2000 Dual energy CT tissue quantification for Monte Carlo based treatment planning for radiotherapy *Proc. 22nd Annual Int. Conf. Of the IEEE Engineering in Medicine and Biology Society* 364
[84]Glover G H 1982 Compton scatter effects in CT reconstruction *Med. Phys.* **9** 860-867
[85]Hawkes D J Jackson Daphne F 1980 An accurate parameterisation of the X-ray attenuation coefficient *Phys. Med. Biol.* **25** 1167-1171

[86]Herman T. Image reconstruction from projections: implementations and principles Springer-Verlag Berlin (1979)
[87]Ioppolo J L Price R I Tuchyna T Buckley C E 2002 Diagnostic X-ray dosimetry using Monte Carlo simulations *Phys. Med. Biol.* **47** 1707-1720
[88]Kanamori H Nakamori N Inoue K Takenaka E 1985 Effects of scattered X-ray on CT image *Phys. Med. Biol.* **30** 239-249
[89]Kumar U Ramakrishna G S Pendharkar A S Singh G 2002 Behavior of reconstructed attenuation values with X-ray tube voltage in an experimental third-generation industrial CT system using Xscan linear detector array *Nuclear Instruments and Methods in Physics Research A* **409** 379-391
[90]Kyriakou Y Riedel T Kalender W 2006 Combining deterministic and Monte Carlo calculations for fast estimation of scatter intensities in CT *Phys. Med. Biol.* **51** 4567-4586
[91]Matsufuji N Tomura H Futami Y Yamashita H Higashi A Minohara S Endo M Kanai T 1998 Relationship between CT number and electron density scatter angle and nuclear reaction for Hadron-therapy treatment planning *Phys. Med. Biol.* **43** 3261-3275
[92]McCullough E C Holmes T W 1985 Acceptance testing computerized radiation therapy treatment planning systems : direct utilization of CT scan data *Med. Phys.* **12** 2597-2621
[93]McCullough E C 1975 Photon attenuation in computed tomography *Med. Phys.* **2** 307-320
[94]Merritt R B Chenery S G 1986 Quantitative CT measurements : the effect of scatter acceptance and filter characteristic on the EMI 7070 *Phys. Med. Biol.* **31** 55-63
[95]Midgley S M 2003 A parameterization scheme for the X-ray linear attenuation coefficient and energy absorption coefficient *Phys. Med. Biol.* **49** 307-325
[96]Palmans H Verhaegen F 2005 Assigning nonelastic nuclear interactions cross sections to Hounsfield units for Monte Carlo treatment planning of proton beams *Phys. Med. Biol.* **50** 991-1000
[97]Perisinakis K Raissaki M Tzedakis A Theocharopoulus N 2005 Reduction of eye lens radiation dose by orbital bismuth shielding in pediatric patients undergoing CT of the head : a Monte Carlo study *Med. Phys.* **32** 1024-1030
[98] International Electronic Commission *Nuclear instrumentation MCA histogram data interchange format for nuclear spectroscopy* International standard IEC 1455 International Electronic Commission Geneva, Switzerland (1995)
[99]Quivey J M 1979 Treatment planning for heavy ion radiotherapy *Int. J. Radiat. Oncol. Biol. Phys.* **5** 1809-1819
[100] Rietzel E Geiß O Schardt D Voss B Krämer M Kraft G 2000 Correlation between CT number and water equivalent thickness for heavy charged particles *XIII ICCR, Heidelberg, Germany* 362-364
[101] White D R 1977 An Analysis of the Z-dependence of photon and electron interactions *Phys. Med. Biol*. **22** 219-228

LIST OF FIGURES

LIST OF TABLES

APPENDIX A: MEASUREMENTS OF CT-NUMBERS AT VARIOUS SCANNERS

Table 15. CT protocols used for CT-number measurements in Gammex substitutes. Measurement results are shown in Table 16. Table headings refer to the name of the protocol (bold letters) and its specifications (kV, mAs, Reconstruction kernel, diameter of FOV in mm, slice thickness in mm).

	CT - scanner	**Protocol**	kV	mAs	Recon	FOV	Slice
1[+]	Siemens Emotion**	**Head**	80 (79.3)	300	H40s	287	3
2[+]	Siemens Emotion**	**Head**	110 (101.9)	300	H40s	287	3
3[+]	Siemens Emotion**	**Head**	130 (121.7)	300	H60s	287	3
4	Siemens Sensation 4	**Head**	120	300	H40s	287	3
5	Siemens Sensation 4	**Head and neck -1**	120	300	H40s	500	3
6	Siemens Sensation 4	**Head and neck-2**	120	300	H60s	500	3
7	Siemens Sensation 4	**Body-1**	120	300	B40s	500	1
8	Siemens Sensation 4	**Body-2**	120	300	B40s	500	5
9	Siemens Open	**Head**	120	300	H40s	287	3
10	Siemens Open	**Head and neck-1**	120	300	H40s	500	3
11	Siemens Open	**Head and neck-2**	120	300	B40s	500	3
12	Siemens Open	**Head and neck-3**	120	300	B60s	500	3
13	Siemens Open	**Body-1**	120	300	B40s	500	3
14	Siemens Open	**Body-1**	120	300	B70s	500	3
15	Toshiba Aquilion16	**Head**	120	300	FC48	500	3
16	Toshiba Aquilion16	**Body**	120	300	FC10	500	3
17	Toshiba Aquilion16	**FC69_500**	120	300	FC69	500	3
18	Toshiba Aquilion16	**FC10_500**	120	300	FC10	500	3
19	Toshiba Aquilion16	**FC48_500**	120	300	FC48	500	3
20	Toshiba Aquilion16	**FC69_400**	120	300	FC69	400	3
21	Toshiba Aquilion16	**FC10_400**	120	300	FC10	400	3
22	Toshiba Aquilion16	**FC48_400**	120	300	FC48	400	3
23	Toshiba Aquilion16	**FC69_320**	120	300	FC69	320	3
24	Toshiba Aquilion16	**FC10_320**	120	300	FC10	320	3
25	Toshiba Aquilion16	**FC48_320**	120	300	FC48	320	3
26	Toshiba Aquilion16	**FC69_240**	120	300	FC69	240	3
27	Toshiba Aquilion16	**FC10_240**	120	300	FC10	240	3
28	Toshiba Aquilion16	**FC48_240**	120	300	FC48	240	3
29	Philips MX8000	**C 500**	120	300	C	500	3
30	Philips MX8000	**C 400**	120	300	C	400	3
31*	Philips MX8000	**C 320**	120	300	C	320	3
32	Philips MX8000	**C 240**	120	300	C	240	3
33	Philips MX8000	**C 180**	120	300	C	180	3
34	Philips MX8000	**EC 500**	120	300	EC	500	3
35	Philips MX8000	**EC 400**	120	300	EC	400	3
36*	Philips MX8000	**EC 320**	120	300	EC	320	3
37	Philips MX8000	**EC 240**	120	300	EC	240	3
38	Philips MX8000	**EC 180**	120	300	EC	180	3
39	Philips MX8000	**D 500**	120	300	D	500	3
40	Philips MX8000	**D 400**	120	300	D	400	3
41*	Philips MX8000	**D 320**	120	300	D	320	3
42	Philips MX8000	**D 240**	120	300	D	240	3
43	Philips MX8000	**D 180**	120	300	D	180	3

[+] Nominal voltage settings are different from actual (in brackets).

* Protocol compared to head protocol measurements of the vendors.

Table 16. Measured CT-numbers in Gammex substitutes. Measurements were performed using the protocols descried in Table 15 above. The heading of the table shows the name, mixture number and electron density of each substitute material.

	Lung	Adipose fat	Breast	Solid water	Muscle	Brain	Liver	Inner bone	B200	CB2 30%	CB2 50%	Cortical bone
	LN450	AP6	BR12	RMI457	RMI452	SR2	LV1	IB	B200	CB230	CB250	SB3
	0.4	0.9	0.96	0.99	1.02	1.05	1.07	1.09	1.11	1.28	1.47	1.69
1**	-578±20	-137±4	-67±4	7±5	40±5	-17±4	82±5	391±9	399±9	723±16	1332±28	1999±41
2**	-577±23	-121±4	-59±5	2±5	35±5	1±5	76±5	311±7	320±7	600±13	1088±24	1616±36
3**	-583±20	-114±4	-56±5	-1±4	31±5	7±4	73±5	274±6	283±7	546±11	987±22	1459±36
4	-587±24	-120±5	-63±5	-8±6	25±6	1±5	66±6	265±6	273±6	533±7	971±11	1440±16
5	-585±27	-120±5	-62±5	-8±6	25±6	2±5	66±5	265±6	273±7	534±6	972±13	1441±19
6	-564±52	-113±17	-57±18	-5±16	32±21	4±18	66±18	259±19	268±21	521±20	944±23	1399±28
7	-557±27	-107±6	-53±6	-4±7	28±8	9±6	66±7	244±7	253±7	496±8	900±10	1339±13
8	-556±23	-107±5	-53±5	-4±6	27±6	9±5	66±6	244±6	253±6	496±6	899±8	1338±11
9	-608±27	-123±6	-64±6	-10±6	23±7	2±6	68±6	264±6	273±7	536±22	972±11	1443±18
10	-609±25	-124±6	-65±5	-10±6	23±7	3±5	66±6	263±6	273±7	535±7	972±11	1443±17
11	-556±26	-107±6	-52±7	-2±7	29±8	9±6	68±7	249±8	258±8	500±8	904±10	1339±11
12	-553±52	-107±19	-52±20	-2±20	29±21	9±19	68±21	248±22	258±22	499±22	901±26	1335±28
13	-559±25	-108±6	-53±6	-3±7	29±8	9±6	68±7	249±7	257±8	500±8	905±9	1341±13
14	-557±59	-108±23	-52±22	-3±24	29±24	9±22	68±23	248±25	256±25	499±26	901±27	1336±32
15	-610±23	-124±5	-62 ±6	2 ±6	35 ±7	2 ±6	78 ±6	311 ±6	320 ±7	602 ±7	1078 ±9	1581±16
16	-612±24	-129±4	-64±5	-2±5	31±6	-2±5	74±5	308±5	317±6	599±5	1076±9	1579±14
17	-726±27	-118±5	--	23±5	36±4	--	--	229±9	--	--	--	1435±9
18	-784±27	-119±5	--	30±6	42±5	--	--	262±9	--	--	--	1540±17
19	-789±30	-122±5	--	26±6	38±6	--	--	259±9	--	--	--	1538±18
20	-723±37	-133±5	--	32±5	42±6	--	--	236±10	--	--	--	1451±9
21	-759±35	-111±5	--	39±6	47±6	--	--	261±10	--	--	--	1514±19
22	-762±39	-112±5	--	37±6	45±6	--	--	260±10	--	--	--	1515±20
23	-727±38	-145±6	--	24±6	35±6	--	--	219±10	--	--	--	1422±8
24	-754±34	-118±5	--	24±6	33±6	--	--	230±10	--	--	--	1430±15
25	-755±38	-118±5	--	23±6	33±6	--	--	230±10	--	--	--	1432±16
26	-719±35	-112±6	--	25±6	37±6	--	--	220±11	--	--	--	1418±8
27	-734±32	-112±5	--	27±6	38±6	--	--	230±10	--	--	--	1410±16
28	-736±35	-112±5	--	27±6	38±6	--	--	230±10	--	--	--	1412±17
29	-548±16	-98±5	-44±6	6±5	36±6	18±5	75±6	253±7	261±7	503±6	907±7	1344±8
30	-547±17	-98±5	-43±6	7±6	37±7	19±6	76±6	253±7	262±7	503±7	906±8	1345±10
31*	-548±17	-97±6	-43±6	7±6	36±7	19±6	76±6	254±7	263±7	503±7	907±8	1344±7
32	-554±15	-96±5	-42±6	7±6	38±6	20±5	78±6	255±7	263±7	504±8	907±80	1346±9
33	-547±17	-97±6	-42±6	7±6	38±7	20±6	78±6	255±7	264±7	504±7	908±8	1347±9
34	-593±13	-105±4	-47±5	8±4	41±5	22±4	83±5	276±6	285±5	547±5	985±7	1457±9
35	-597±16	-105±5	-46±4	9±4	41±5	21±5	84±5	277±5	286±5	548±6	988±9	1465±13
36*	-586±16	-104±0	-47±4	8±5	41±5	21±4	84±5	277±6	286±6	547±5	986±9	1459±10
37	-596±16	-104±4	-45±4	9±5	42±5	23±4	85±4	279±5	288±5	550±6	989±9	1466±13
38	-595±16	-104±4	-45±4	9±4	43±5	23±4	85±5	279±5	288±5	549±6	990±9	1468±14
39	-587±28	-108±10	-51±11	3±10	35±10	17±9	76±11	267±13	276±12	534±12	965±14	1431±18
40	-592±33	-109±12	-51±12	3±12	36±13	16±13	77±13	268±14	277±14	536±15	969±18	1439±23
41*	-593±34	-109±13	-51±14	3±13	35±15	16±14	77±15	268±16	277±16	534±16	966±19	1433±22
42	-592±34	-108±13	-51±13	4±14	36±14	17±14	78±14	270±16	279±16	537±17	970±20	1440±24
43	-591±32	-108±14	-50±14	4±14	37±15	17±14	78±15	270±15	279±16	537±17	971±19	1442±26

* protocol compared to head protocol measurements of the vendors.

** data extracted using Dicom works (no information on the SD in the slice)
reported SD is estimated from previous measurements

APPENDIX B: SIMULATED CT-NUMBERS

Table 17. Parameters used for simulations of CT-numbers. The table describes the number of independent views per reconstructed image (# view), the peak voltage of the photon spectrum (KV), if scatter corrections were applied (SC), if beam hardening corrections were applied (BHC), type of simulated phantom material (phan-material), the electron density of the phantom material relative to water (e-density) , the simulated diameter of the phantom (diameter) in cm, and finally the type of inserts(inserts) used for the phantom. All the beam hardening corrections were performed using ψ_{40kV} defined in 3.6.8

			Corrections		Phantom			
	# view	kV	scatter	BHC	Material	e-density	Diameter (cm)	Inserts
1+	5	110	yes	yes	PMMA	1.15	16	Gammex subs
2+	5	110	yes	yes	water	1.00	16	Gammex subs
3+	5	110	yes	yes	RW3	1.01	16	Gammex subs
4+	5	110	yes	yes	muscle	1.02	16	Gammex subs
5+	5	110	yes	yes	CB	1.69	16	Gammex subs
6+	5	110	yes	yes	AIR	0.00	16	Gammex subs
7	1	110	yes	yes	PMMA	1.15	12	Gammex subs
8	1	110	yes	yes	PMMA	1.15	16	Gammex subs
9	1	110	yes	yes	PMMA	1.15	20	Gammex subs
10	1	110	yes	yes	PMMA	1.15	24	Gammex subs
11	1	110	yes	yes	PMMA	1.15	28	Gammex subs
12	1	110	yes	yes	PMMA	1.15	32	Gammex subs
13	5	130	yes	no	PMMA	1.15	16	Gammex subs
14	5	120	yes	no	PMMA	1.15	16	Gammex subs
15	1	115	yes	no	PMMA	1.15	16	Gammex subs
16	5	110	yes	no	PMMA	1.15	16	Gammex subs
17	1	105	yes	no	PMMA	1.15	16	Gammex subs
18	1	100	yes	no	PMMA	1.15	16	Gammex subs
19	5	80	yes	no	PMMA	1.15	16	Gammex subs
20	5	120	yes	no	PMMA	1.15	16	H-materials

+ The simulations 1-6 in Table 17, were also carried out for water as a phantom insert, results are sown in Table 10

Table 18. Simulated CT-numbers corresponding to the settings in Table 17.

	LN300	LN450	Adipose fat	Brain	Muscle	IB	CB2 30	CB2 50	CB
1	-697±110	-550±110	-105±79	-7±120	62±103	239±114	583±118	1085±261	1597±180
2	-688±80	-548±79	-104±92	-4±129	23±94	219±89	553±97	1038±117	1566±140
3	-700±48	-550±72	-111±92	-5±88	56±81	209±112	588±94	1055±117	1586±182
4	-684±67	-530±76	-89±88	6±93	49±107	230±90	553±136	1058±143	1543±173
5	-501±593	-404±471	-42±430	197±698	126±526	281±774	609±671	939±441	1282±1030
6	-725±7	-576±11	-139±11	-27±17	37±13	253±19	661±21	1189±40	1751±68
7	-694±97	-545±141	-71±172	18±102	92±101	267±163	657±159	1141±70	1691±278
8	-676±232	-516±244	-132±172	1±208	93±233	274±240	601±313	1092±252	1616±351
9	-663±303	-561±252	-73±449	70±425	80±320	292±252	577±682	1087±417	1537±465
10	-694±252	-489±390	-126±628	91±508	31±563	230±557	627±701	1046±867	1540±940
11	-634±286	-445±248	-127±264	88±350	40±234	218±416	601±283	959±612	1461±334
12	-557±437	-411±448	-34±339	108±355	103±440	274±518	633±494	1072±575	1436±633
13	-701±102	-543±124	-140±101	-18±119	15±110	146±112	490±116	940±119	1381±166
14	-690±74	-532±87	-116±115	-10±115	35±103	200±115	548±135	1006±145	1462±166
15	-684±167	-551±150	-190±228	-35±181	-12±161	177±127	511±208	934±245	1436±261
16	-681±110	-534±110	-91±79	6±119	74±103	250±113	590±117	1086±257	1590±177
17	-704±189	-522±245	-86±274	13±139	95±258	284±212	663±238	1158±243	1661±342
18	-677±155	-541±193	-140±220	-46±235	10±188	220±189	556±256	1042±428	1575±360
19	-686±115	-549±102	-143±106	-2±150	44±91	277±113	681±134	1253±97	1862±196

	H-800	H-500	H+200	H+400	H+900	H+1200	PMMA
20	-729±75	-436±83	289±176	461±187	1013±189	1407±137	147±182

APPENDIX C: ELEMENTAL COMPOSITION OF SIMULATED MATERIALS

Table 19.Composition of materials used CT-simulation (phantom & inserts) [7] [21] [28] [30].

MATERIAL	Physical Density	Electron Density Relative to Water	%H	%C	%N	%O	%Mg	%Si	%P	%Cl	%Ca	%Ti	%Sn	%Ar
Gammex substitutes														
lung (LN300)	0.30	0.29	8.46	59.38	1.96	18.14	11.19	0.78		0.10				
lung (LN450)	0.45	0.44	8.47	59.57	1.97	18.11	11.21	0.58		0.10				
Adipose fat	0.92	0.90	9.06	72.30	2.25	16.27				0.13				
Breast	0.98	0.96	8.59	70.11	2.33	17.90				0.13	0.95			
CT Solid Water	1.02	0.99	8.00	67.30	2.39	19.87				0.14	2.31			
Muscle	1.05	1.02	8.10	67.17	2.42	19.85				0.14	2.32			
Liver	1.04	1.01	8.06	67.01	2.47	20.01				0.14	2.31			
Brain	1.05	1.05	10.83	72.54	1.69	14.86				0.08				
CB230	1.34	1.29	6.68	53.48	2.12	25.61				0.11	12.01			
CB250	1.56	1.47	4.77	41.63	1.52	32.00				0.08	20.02			
Cortical bone	1.82	1.69	3.41	31.41	1.84	36.50				0.04	26.81			
Bone Mineral	1.15	1.10	6.65	55.52	1.98	23.64			3.24	0.11	8.87			
Inner Bone	1.13	1.09	6.67	55.64	1.96	23.52			3.23	0.11	8.86			
H-materials														
H-800	0.23	0.22	7.96	64.21		16.29		11.48					0.06	
H-500	0.47	0.46	8.04	45.93		19.41		26.48					0.14	
H+200	1.04	1.01	7.70	31.50		22.99		35.66			1.96		0.19	
H+400	1.12	1.07	6.35	28.07		27.38		29.40			8.64		0.16	
H+900	1.43	1.33	3.72	21.41		35.93		17.21			21.64		0.09	
H+1200	1.65	1.52	2.40	18.07		40.21		11.10			28.16		0.06	
Phantom materials														
Air	10^{-3}	0.00		0.01	75.27	23.17								1.28
Water	1.00	1.00	11.19			88.81								
PMMA	1.18	1.15	8.05	59.98		31.96								
RW3	1.05	1.01	7.59	90.41		0.80						1.20		

APPENDIX D: CALCULATION OF WEPL USING SHIELD-HIT V2

The WEPL can be calculated using the Shield-HIT v.2. when no measurements are available. Shield-HIT v.2. is a MC code for Carbon ion simulation (for more information see [79]). The simulated geometry in Figure 84 represents a water cylinder of 40 cm thickness. The first cm at beam entrance is water; the second cm was defined as different compounds and mixtures of tissue and substitute materials. The remainder of the tube was simulated as water. The energy deposition was simulated using 0.01 cm thick spacing.

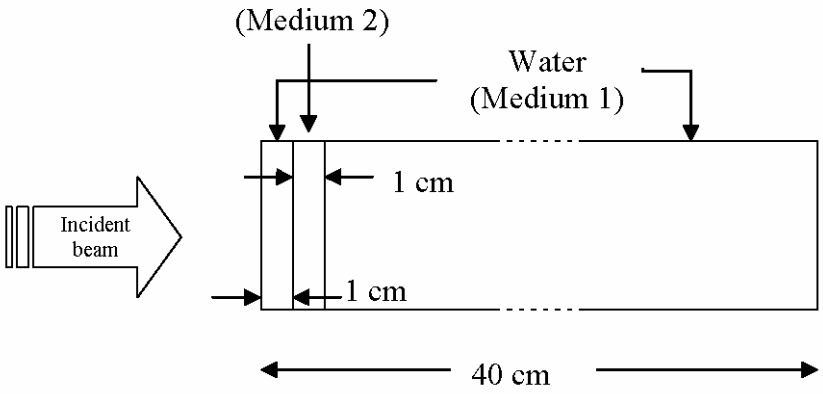

Figure 84. Schematic diagram of simulated geometry for WEPL calculation using Shield-Hit v.2.

The incident beam was ^{12}C with energies 184 and 270 MeV/u. The number of incident particles was 5000 and the simulation included nuclear reactions, multiple scattering interactions and Gaussian straggling pattern. ICRU data was used for information on the stopping power ratios. The ionization potential of the compounds and mixtures were calculated for each material using the Bragg rule from the ionization potentials of the single elements.

The simulation was first performed setting “medium 2” as water for the reference simulation of the Bragg-peak position. The simulation was redone setting medium 2 as one of the examined tissues or substitutes. The water Equivalent Depth (WEPL) was calculated from the simulated depth dose curves as a function of the difference in the peak positions ($\Delta Peak$) as:

$$WEPL = \left(\Delta Peak_{Water} + 1cm\right)/1cm \,. \qquad \text{(D.1)}$$

Depending on the calculated ionization potential of the mixtures and compounds the uncertainty in the peak position is calculated. Its is estimated that 2 eV deviation in the ionization potential cause a peak shift of 0.05 cm.

The executable version of the Shield Hit v.2. code required the modification of the source code to accept more than 8 elements in material composition, to have 0.01 spacing in scoring planes and to have double precision storage of the energy deposition per position. The executable version of the code was used to simulate the depth dose profiles for the H-substitutes, the Gammex substitutes and for ICRU tissue compositions. The output of the simulation agrees very well with experimental results.

Acknowledgements

This work wouldn't have seen light without the help and support of the following generous people. The contributions they made towards the development of this work are briefly listed here.

From the department of Medical Physics in Radiation Oncology of DKFZ, I especially thank: **Prof. Dr. Wolfgang Schlegel**, head of department of Medical Physics in Radiation Oncology. He has always supported the work and allowed the funding to purchase equipments for many thousands of euros. **Prof. Dr. Oliver Jäkel**, head of the heavy ion research group and my direct supervisor for the last four years. His confidence in the work and constant encouragement never wavered. **Dr. Malte Ellerbrock.** He has been my primary discussion partner on this work. He had to put up with my impatience. Yet, he always pulled me out of the tight spots I regularly found myself in. **Benjamin Ackermann** was highly supportive and a great help. He never failed to help in either the scientific or labour parts of the work such as carrying heavy phantoms, refilling liquid nitrogen tanks or performing CT-measurements and discussing them. **Dr. Christian Karger** and **Prof. Dr. Günter Hartmann** supported the work and raised many enlightening discussions. **Dr. Oksana Geithner** provided an executable version of the Shield HIT v.2. code for WEPL simulations. **Ms. Marina Romanchikova** provided most of the simulated X-ray spectra.

Dr. Anna Wysocka, from the Andrzej Sołtan Institute for Nuclear Studies in Świerk -Poland, introduced me to BEAMnrc and helped in laying out the structure of the work and in performing MC simulations. **Prof. Dr. Marc Kachelriess** and **Dr. Christian Penssel**, from the Institute of Medical Physics in Erlangen-Germany, provided the BHC and the reconstruction code. **Dr. Dieter Schardt**, from the GSI, provided the expertise, equipments and time needed to perform WEPL measurements. **Dr. Stefan Ulzheimer**, **Dr. Wallschläger** and **Dr. Heismann**, from Siemens Medical Solutions, provided technical data on the Emotion CT, X-ray spectra and the response function of the detectors. Last but not least, **Prof. Dr. Hüfner**, from the physics department of Heidelberg University. His support allowed me to enrol in the PhD-program.

This work was funded by the **PhD program** of the German Cancer Research Center (DKFZ) in Heidelberg, Germany.

On a personal level, thanks are dearly due to:

My gorgeous family: Mum, who neither stopped worrying about me nor praying for me; Dad, my rock and energy well; Lama & Isam, Ghadeer & Tareq, Hakam, Nura and Malak, whose love, advice, emotional and financial support kept me on my feet. I can never say thank you enough. Nor can I say how much I love and miss every one of you! I wouldn't have made it without you!

Raeda, Bassem, Yara and Hassan Shomar, My Heidelberg family. Anna Wysocka-Rabin has been a friend, a partner and a second mother. Her husband, Dr. Kenneth Rabin, who patiently endured our long working hours and revised parts of this work. The wonderful Christine Hartmann-Harting, for her generous support, delicious cakes and cheer-up conversations. The heavy ion group (old and current) who supported and patiently revised this work especially Oliver, Malte, Benjamin and Niels (who is not an E409er yet, but will soon be). My Palestinian friends and comrades, Fadia Jaber & Maha Iraqi. Gregor Remmert who first invited me to share his office then his lab. The Bohnanza group: Christine, Ina, Benjamin, Urban, Gerhard, Maria, Oksana & Wolfgang and finally Anja & Frank who are currently rediscovering Australia.

To all the above: I thank you for putting up with me and for making my stay in Heidelberg enjoyable!

Another person who should be mentioned here is Asem El Haj-Hamad. Asem was a bright student at An Najah University and a fellow Palestinian. He had won a scholarship for a study-trip to Germany. Alas, he was forbidden to leave Palestine by the Israeli Authorities. Soon afterwards and before setting foot to Germany, Asem, who suffered a chronic heart disease, died at the age of 22 in Nablus. Though we only spoke on the phone, Asem's sudden and tragic death hit me hard. It made me realize how privileged I am compared to average Palestinians; I can travel and work without worrying about curfews, roadblocks, demolished houses or flying bullets; I also had the time and chance to do this work. I thank Asem for putting my world into its right proportions and for giving me more will to finish this work as best as I possibly can.

I foremost thank God for all I have; thank him for helping me getting to where I am now and hope for more of his help in bringing the things I've learned in Germany to the people left in Palestine!